UNIVERSITY OF CALIFORNIA

Los Angeles

Additive manufacturing of functional materials based on digital light processing

A dissertation submitted in partial satisfaction of the requirements for the degree Doctor of Philosophy in Materials Science and Engineering

by

Dong Wu

2023

ABSTRACT OF THE DISSERTATION

Additive manufacturing of functional materials
based on digital light processing

by

Dong Wu
Doctor of Philosophy in Materials Science and Engineering
University of California, Los Angeles, 2022
Professor Ximin He, Chair

Additive manufacturing (AM) has been reshaping several industries and markets by providing a more cost-effective, faster, and customizable approach for fabricating complex parts compared to traditional manufacturing. Digital light processing (DLP)-based printing as one of the most popular AM processes has been extensively used in aesthetics, healthcare, & jewelry industries. Its applications are expanding other domains as well. Despite of the achievement, challenges such as materials limitation, production scaling and product functionality still need to be addressed, and more possible applications are expected to be explored. This dissertation aims to address these challenges by developing new functional materials and printing strategies based on DLP, and exploiting their potential applications in biomimetic study, soft robotics and flexible electronics.

In Chapter 1, the dissertation provided an overview of various additive manufacturing technologies. The development and the challenges of 4D printing and photo-induced

metal printing were discussed from the perspectives of materials and fabrication methods.

Chapter 2 and 3 focused on 4D printing methods of functional hydrogel structures for biomimetic study and soft robotics. The mechanical designs of the printed structures and advances in fabricating techniques were carefully discussed.

In Chapter 4 and 5, the dissertation explored novel metal patterning approaches at ambient conditions and discussed the properties of printed metals and the patterning mechanisms. Various applications of printed metallic traces, including wearable electronics, bioelectrodes for electrography and soft robotics, have been demonstrated.

Chapter 6 summarized the progresses made in developing new functional materials and printing strategies based on DLP in this dissertation. A positive outlook for DLP-based printing technologies was provided.

The dissertation of Dong Wu is approved,

Jonathan Hopkins

Xiaochun Li

Aaswath Raman

Ximin He, Committee Chair

University of California, Los Angeles

2023

Dedicated to my parents Cixi Chen, Minghua Wu,

and my love Mu Xu

For their unconditional love and support

TABLE OF CONTENTS

List of Figures

List of Tables

ACKNOWLEDGEMENTS

First and foremost, I would like to express my heartful gratitude to my family, without whom this would never have been possible. Their unconditional love and support are always my foundation.

My doctoral journey in the group has been both challenging and fulfilling. I was fortunate to join the He research group and I am grateful to be a part of such an excellent team. I have gained valuable knowledge, learned advanced techniques, and received comprehensive trainings to become a qualified researcher. I am deeply thankful to my advisor and my colleagues who have been consistently helpful and supportive.

I owe a special debt of gratitude to my advisor Prof. Ximin He for her exceptional guidance and unwavering support throughout my entire PhD study. Her professionalism, patience and responsiveness have helped me overcome numerous challenges, both in research and in life. I am also deeply grateful to Prof. Jonathan Hopkins, Prof. Xiaochun Li and Prof. Aaswath Raman for serving as my committee members and providing their expertise and precious advice in my research.

I would like to acknowledge Prof. Hanqing Jiang, Prof. Tzung K Hsiai, Dr. Zirui Zhai Dr. Qingyu Cui, for the academic collaborations, supportive discussions and guidance, without which many projects would not have been possible.

Eventually, I would like to express my sincere gratitude to my lab mates for their supports in academic research and daily life. They are Dr. Shuwang Wu, Dr. Bowen Yao, Dr. Cheolgyu Kim, Dr. Mutian Hua, Dr. Yusen Zhao, Dr. Yanfei Ma, Dr. Chi Chen, Yousif Alsaid, Jiaqi Song, Hardik Hingorani, Poom Narongdej, Yucheng Zhang, Sidi Duan, Yingjie Du, Yichen Yan, Pengju Shi, Zixiao Liu, Imri Frenkel and so on. I will certainly miss the days we worked together in the He lab.

VITA

2013-2017 B.S., Materials Science and Engineering, Southern University of Science and Technology, Shenzhen, China

PULICATIONS

Journal Publications

[1] **Fast and facile liquid metal printing via projection lithography for highly stretchable electronic circuits**

D Wu, S Wu, P Narongdej, S Duan, C Chen, Y Yan, Z Liu, X He*

In preparation

[2] **Room-temperature Annealing-free Gold Printing via Anion-assisted Photochemical Deposition**

D Wu, B Yao, S Wu, H Hingorani, Q Cui, M Hua, I Frenkel, Y Du, TK Hsiai, X He

Advanced Materials 2022, 2201772

[3] **Visualizing morphogenesis through instability formation in 4-D printing**

D Wu†, J Song†, Z Zhai, M Hua, C Kim, I Frenkel, H Jiang, X He

ACS applied materials & interfaces 2019. 11 (50), 47468-47475

[4] **4D printable tough and thermoresponsive hydrogels**

M Hua†, **D Wu**†, S Wu, Y Ma, Y Alsaid, X He

ACS applied materials & interfaces 2020, 13 (11), 12689-12697

[5] **Tunable Sponge-Like Hierarchically Porous Hydrogels with Simultaneously Enhanced Diffusivity and Mechanical Properties**

Y Alsaid, S Wu, **D Wu**, Y Du, L Shi, R Khodambashi, R Rico, M Hua, Y Yan, Y Zhao, D Aukes, X He

Advanced materials 2021, 33 (20), 2008235

[6] **Homogeneous freestanding luminescent perovskite organogel with superior water stability**

Y Zhang, Y Zhao, **D Wu**, J Xue, Y Qiu, M Liao, Q Pei, MS Goorsky, X He

Advanced Materials 2019, 31 (37), 1902928

Book Chapter

[1] **Bio-Inspired Anti-Icing Surface Materials**

S Wu, Y Yan, **D Wu**, Z He, X He

Ice Adhesion: Mechanism, Measurement and Mitigation, 467-493

" † " for co-first author

Chapter 1. Introduction

1.1 Additive Manufacturing

Additive manufacturing (AM), also termed as 3D printing, has been developing rapid since the concept was first introduced in 1980s. As a newly developed technique, AM has distinguished from tradition manufacturing technologies including substrative and formative manufacturing (**Figure 1.1**). Substrative manufacturing is a process by which 2D/3D parts are created by successively removing material from a solid block of materials, such as computer numerical control (CNC) machining (turning, drilling, milling), electrical discharge machining (CDM), water jet cutting and laser cutting. Formative manufacturing refers to as the process of forming 3D parts with designed shapes by applying stresses to cause plastic deformation of a material, such as injection molding and stamping. Additive manufacturing is the process that constructs 2D/3D parts by continuously adding materials to the parts. The general AM process consists of four steps: a virtual model is firstly created by computer-aid design (CAD) and then digitally sliced into multiple layers; after that, either a code of building paths or a serial of patterns is generated for the subsequent printing process; printing of the parts; as the printing finishes, postprocessing is usually demanded, such as washing, curing, annealing, polishing and coloring. The postprocess turns the printed raw models into products. Compared to the traditional manufacturing, AM offers some significant advantages including greater design flexibility and customization, faster product development cycles and less waste generated during production. In addition, AM allows for fabrication of complex parts which are extremely difficult or impossible to realize

with traditional manufacturing. Despite of the advantages of AM, there are still many challenges for the applications of AM in various industries, including the relatively low fabrication speed for mass production, limited materials selection, limited materials properties, limited size of parts and large preproduction research investments.

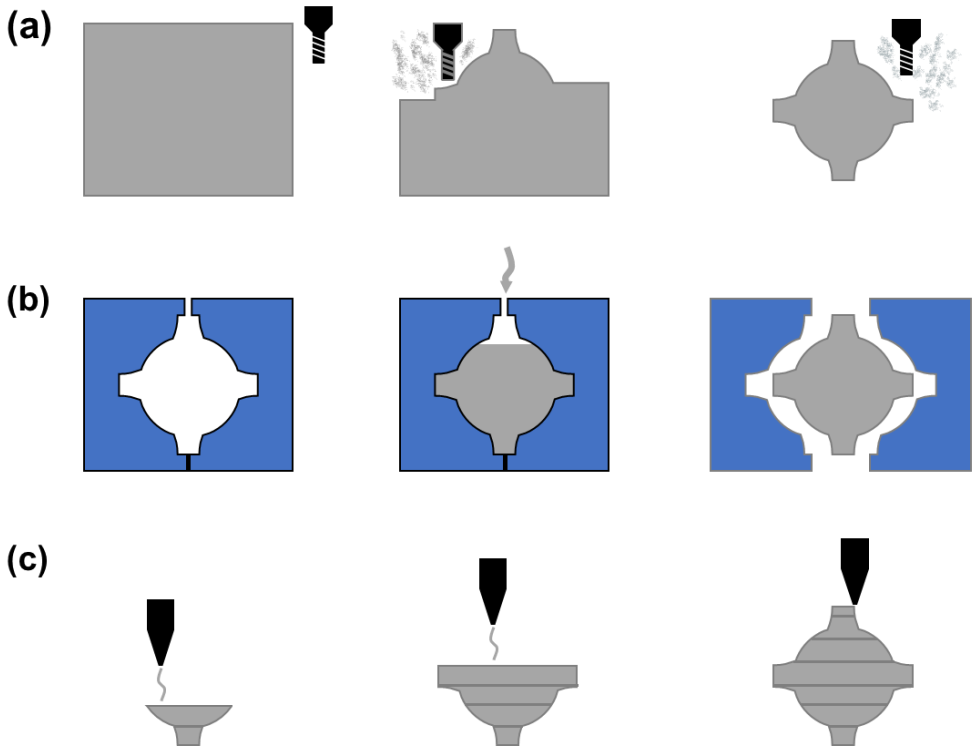

Figure 1.1 Schematics of (a) subtractive, (b) formative and (c) additive manufacturing.

With significant resources invested for the development of the AM industry in the recent decades, many advanced AM technologies have been developed. AM processes can be generally categorized in accordance with their printing mechanisms, including materials extrusion, materials and binder jetting, power bed fusion and vat photopolymerization (**Figure 1.2**). These techniques cover a wide range of materials and benefit diverse applications. [1]

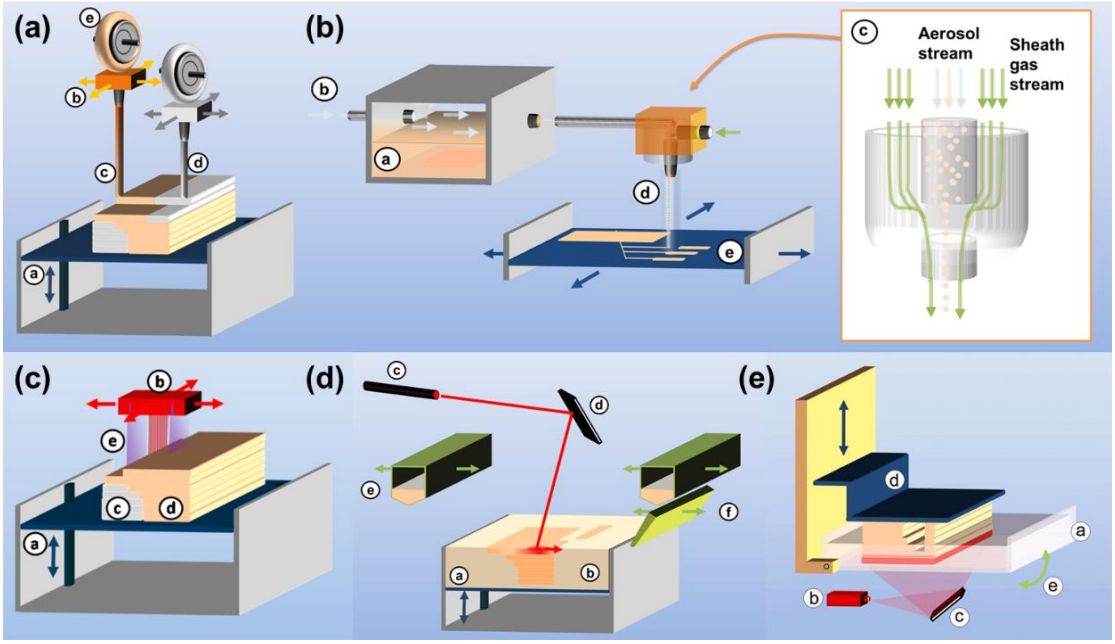

Figure 1.2 Schematic of different additive manufacturing processes: (a) Fused deposition modeling (FDM) as a material extrusion process; (b) Aerosol jet printing (AJ-P) and (c) Inkjet-based lithography (PolyJet) as material and binder jetting processes; (d) Selective laser sintering (SLS) as a powder bed fusion process; (e) Digital light processing (DLP) as a vat photopolymerization process. Reproduced with permission.[1] Copyright 2017, American Chemical Society.

Material extrusion is the most conventional AM technology for simple proof-of-concept and prototyping, due to the inexpensive printing device and materials. It is a process in which a continuous filament of composite or thermoplastic material, such as Polylactic acid (PLA) and acrylonitrile butadiene styrene (ABS), is selectively deposited through a nozzle to build a 3D part layer by layer (**Figure 1.2**a). This category includes Fused deposition modeling (FDM), 3D dispensing, and 3D bioplotting. Despite of the low cost, the applications of material extrusion are limited by the low resolution and rough

surface of printed objects.

Material jetting and binder jetting are inkjet-based AM process in which droplets of either build materials or liquid bonding agents are selectively deposited. Common materials jetting includes thermal inkjet printing, aerosol jet printing (AJ-P) and inkjet-based lithography (PolyJet). In AJ-P process, building materials are first atomized in an aerosol chamber by ultrasonification or pneumatic atomization. The preformed aerosol is then transferred to the movable print head by an inert gas stream and continuously deposited onto the substrate with the help of a sheath gas stream (**Figure 1.2**b). In PolyJet printing, small droplets of photopolymers are selectively deposited through hundreds of nozzles and then polymerized with a subsequent UV curing process (**Figure 1.2**c). Material and binder jetting largely extend the scope of printable materials compared with material extrusion process. Not only thermoplastics can be printed, metals, conductive polymer and ceramics can also be fabricated into 3D objects.

Powder bed fusion is fundamentally different from Materials extrusion and material jetting in which materials are deposited through nozzles. Instead, thermal energy provided by a laser or an electron beam is utilized to selectively fuse regions of a powder bed to construct layers (**Figure 1.2**d). Selective laser sintering (SLS) and electron beam machining (EBM) belong to this category. By controlling the input of the thermal energy, this process can be used to print both metal and polymers.

Vat photopolymerization is an AM technique that builds parts layer-by-layer by selectively polymerize a liquid photopolymer resin (**Figure 1.2**e). Various vat photopolymerization techniques have been developed based on different light

patterning methods, such as stereolithography (SLA), liquid crystal display (LCD) 3D printing, digital light processing (DLP) and multiphoton lithography (MPL). Vat polymerization is distinguished from the other printing techniques due to its high production speed and capability of printing high-resolution complex parts with high accuracy. It has been widely used in commercial production of polymer, metal and ceramic parts.

Besides the AM processes introduced above, there are other techniques such as sheet lamination and directed energy deposition, which can be very useful for metal parts production or mending.

1.2 Digital Light Processing

DLP-based 3D printing is one of the most popular vat polymerization techniques due to its outstanding printing speed, high printing resolution and precision, excellent scalability and mild fabricating conditions. A typical DLP 3D printer consists of a UV light source, a digital micro-mirror device (DMD), a set of projection optics, a motion stage and a tank for UV curable resin (**Figure 1.3**a).[2] DMD is a type of micro-electromechanical system (MEMS) developed by Texas Instrument, serving as the core of DLP printing technology. A DMD chip is composed of an array of millions of micro mirrors which can be tilted ±10-12° individually. This allows the DMD chip to manipulate the reflected light to form complex light patterns, enabling precise and intricate 2D lithography and 3D stereolithography. Starting with such basic setup design, significant advances of DLP-based 3D printing system have been made during the past

decade. By incorporating an oxygen permeable film at the bottom of resin vat, a dead zone inhibiting polymerization was created to eliminate the detaching step and the re-immersion step after curing each layer. Therefore, an improved DLP 3D printing technique termed Continuous liquid interface polymerization (CLIP) was developed to achieve continuous printing, shortening the production time from hours to minutes (**Figure 1.3**b).[3] Similarly, a mobile liquid interface (a fluorinated oil) was introduced between resin and glass window at the bottom of the resin tank allowing a continuous and rapid large-volume print process named high-area rapid printing (HARP).[4] Despite of the huge enhancement in print speed, techniques like CLIP and HARP still rely on the layer-by-layer polymerization of resin induced by a single planar light beam. The possibility of generating a patterned light in 3D space eventually leads to the development of volumetric printing, which allows printing 3D objects in one exposure further increasing the fabrication speed tremendously. Volumetric additive manufacturing can be achieved by employing holographic reconstruction of incident light (**Figure 1.3**c) or using computed axial lithography (CAL) which prints 3D objects with the combination of a rotational resin tank and computed intensity-modulated projections (**Figure 1.3**d).[5,6] With rapid enhancement in printing speed and adaption for high throughput printing, DLP-based lithography and stereolithography are being increasingly adopted for mass production in various industries, including electronics, aerospace, automotive, consumer goods and healthcare. However, many challenges remain to be addressed in materials limitation, production scaling and product quality.

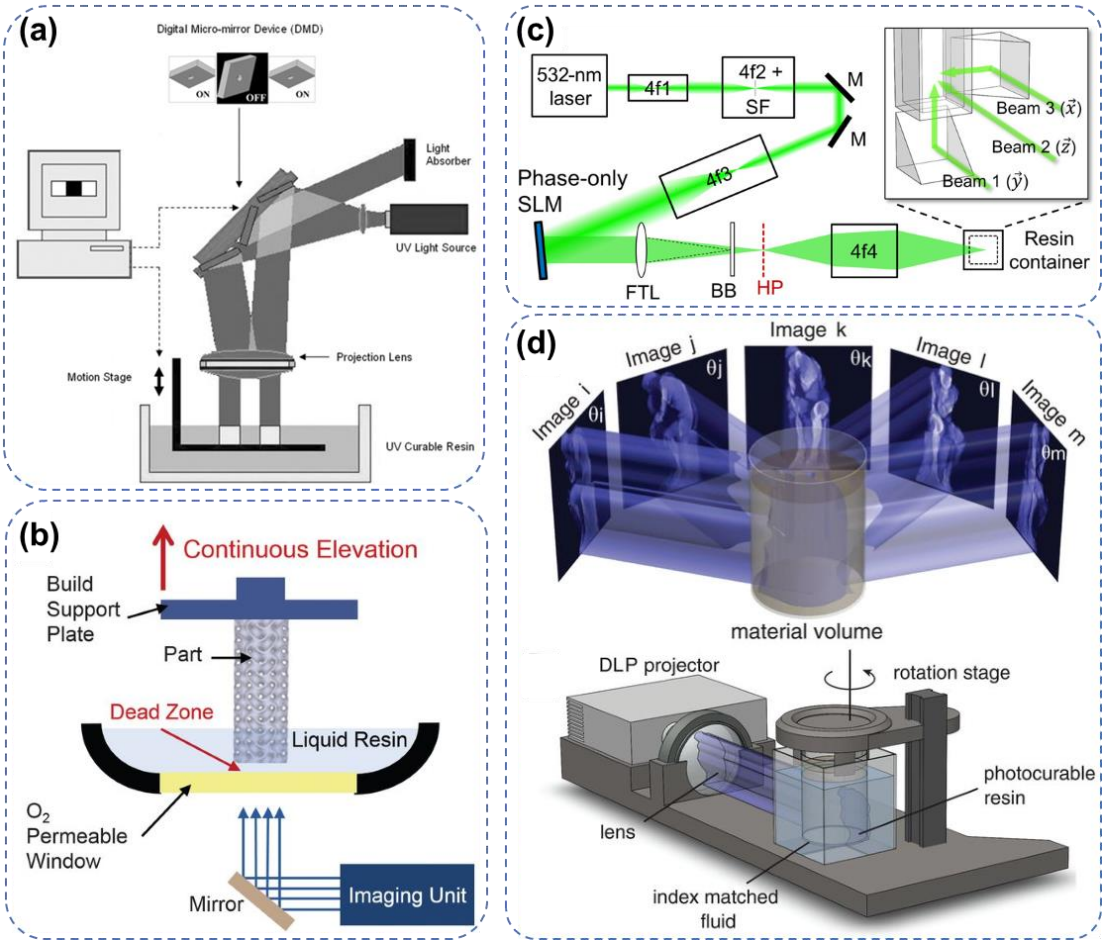

Figure 1.3 (a) Schematic of digital light processing (DLP) printing system. Reproduced with permission.[2] Copyright 2006, WILEY. (b) Schematic of continuous liquid interface polymerization (CLIP) printing system. Reproduced with permission.[3] Copyright 2015, AAAS. (c) Schematic of holographic volumetric 3D fabrication system. Reproduced with permission.[6] Copyright 2017, AAAS. (d) Schematic of the computed axial lithography (CAL) concept and system for volumetric fabrication. Reproduced with permission.[5] Copyright 2019, AAAS.

1.3 4D Printing

The concept of 4D printing evolves from 3D printing as the additional fourth dimension, time, is introduced. Conventional 3D printing builds 3D objects with unchanging shape

and properties throughout their lifetime, while 4D printing build structures that can change their shapes, color or other properties over time in programmable fashions in response to external stimuli such as water, pH, heat, light, etc. This technology can be interpreted as the combination of 3D printing, stimuli-responsive materials and a well-programmed design. Various 3D printing technologies have been used in 4D printing, including FDM, DIW, Inkjet printing, etc. The majority of 4D printing research focusses on the shape-changing ability of the printed structures, such as bending, elongation, curling, buckling and twisting.[7,8] These shape-changing behaviors can be attributed to the relative shrinkage/expansion between active and nonactive parts of the 4D printed structures, which can be fabricated by either a single smart material or heterogeneous multi-materials.

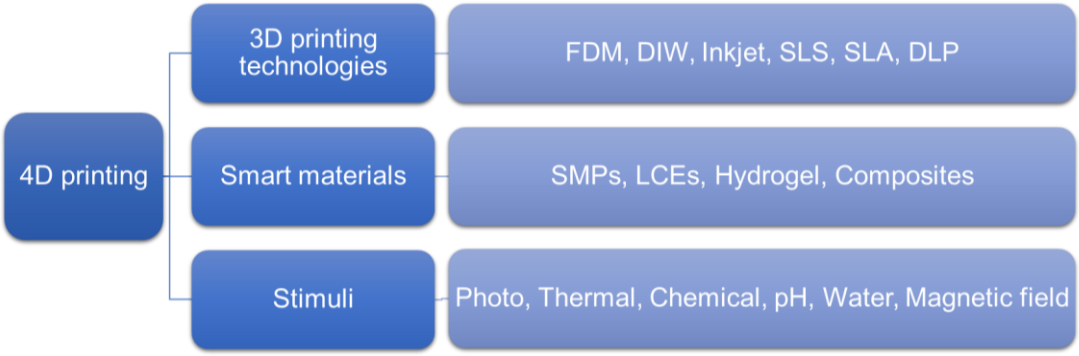

Figure 1.4 Diagrammatic representation of the critical factors of 4D printing.

Shape memory polymers (SMPs), liquid crystal elastomer (LCEs) and hydrogels are the most widely used 4D printing materials (**Figure 1.4**). SMPs are polymers that can maintain a temporary shape and recover to their initial shape in the presence of an external stimulus such as light, electric, solution or heat. To achieve the shape memory

effect, SMPs must consist of chain segments and netpoints, and they require a programming step and recovery step.[9] The netpoints are used to "remember" the permanent shape of the material while the chain segments can respond to the external stimulus. During the programming step, the SMP is first deformed under a proper condition (e.g., at a temperature above glass transition temperature or melting) and the deformation is then fixed by chemical or physical changes (e.g., formation of glassy or crystalline domains) to prevent the movement of polymer chains. Thus, a temporarily stable shape is obtained. As the SMP to a suitable external stimulus, the fixing units will be removed while internal stress will be released, allowing the SMP recover to its original shape. Based on the number of types of fixing units, the shape-memory process can either be one-way with one irreversible temporary shape, or two-way with two reversible temporary shapes. Due to the design flexibility, SMP structures fabricated via 4D printing can be utilized for microgripper, vascular stents, flexible electronic devices.[10,11]

Different from SMPs with programmable and triggerable shape change, LCE changes shape continuously with the constant stimulus. LCE consists of a loosely crosslinked network of mesogens (liquid crystalline polymers) which are aligned with a mechanical stretching treatment. Upon a temperature increase, the thermal transition of LCE from nematic phase to isotropic phase will lead to its macroscopic shape deformation. Despite of the difference in mechanism, LCE can also exhibit shape memory effect with proper structural design and programming.[12] The alignment of mesogens is the critical step during the fabrication of LCE structures. Therefore, LCE can be printed with DIW,

due to the shearing of ink which aligns LCE mesogens when the ink flows through nozzle.[13–15] DLP printing with a pre-alignment step are also reported for printing LCE actuators, in which the alignment of mesogens are achieved by either a rotatable magnetic field or a rotatable resin tray.[16,17] Combined with other materials, LCE-based electrothermal or photoactivated actuators can be printed.[18,19]

Hydrogels are three-dimensional networks of crosslinked hydrophilic polymer chains, capable of absorbing and holding large amounts of water. With stimuli-responsive molecular moieties on the in the networks, some hydrogels can change the water content in response to certain external stimulus, leading to volumetric variation. These stimuli-responsive hydrogels have been used in 4D printing to achieve shape morphing.[20–22] However, due to the limited number of smart hydrogels, non-stimuli responsive hydrogels are also extensively investigated. To achieve shape morphing, researchers have used non-responsive hydrogels to fabricate a variety of multimaterials and composite structures. These structures typically involve different swelling behaviors in different parts or directions.[23,24] Light-based and extrusion-based 3D printing techniques are commonly employed to fabricate hydrogel-based soft sensors and actuators.[25] Additionally, hydrogels have several advantages over SMPs and LCEs. Hydrogels usually inhibit excellent hydrophilicity, biocompatibility and mechanical properties that are comparable to living tissues, which make them an ideal biomaterial candidate.[26,27]

1.4 Photo-induced metal printing

The fabrication of metal patterns and metallic microstructures is crucial in the fields of electronics and mechatronics. Traditional metal deposition methods, including electroplating, electroless plating, sputtering and physical vapor deposition, require a subsequent patterning step, such as photolithography, to obtain the desired patterns and structures. AM technology provide a simpler solution for selectively depositing metal and creating 2D/3D metallic structures. The methods commonly used for metal deposition in AM include screening printing,[28] extrusion-based printing[29] and photo-induced printing.[30] In photo-induced printing, metals can be patterned with the aid of certain light irradiation. The simplest approach is mixing photopolymer precursors with metallic fillers to prepare a metal-polymer composite slurry that can be selectively photopolymerized (**Figure 1.5**a). Such printing technique has been commercialized by Admatec Europe. Metallic structures can also be fabricated through photochemical reduction of metal ions using either 2PL or DLP printing (**Figure 1.5**b).[30–33] Furthermore, it has been reported that photopolymerization of polymer and photoreduction of metal ions can be achieved simultaneously.[34] Photons can not only induce photoreactions, but also can transfer metals. A focused laser pulse can be absorbed by thin metal film to generate a metal droplet deposited onto a substrate, forming metal microstructures (**Figure 1.5**c).[35,36] A laser can also act as an optical trap to navigate the deposition of metal nanoparticles in electrophoresis to produce metal structures (**Figure 1.5**d).[37] Even though various metal printing strategies with simplified process have been developed, the incomplete understanding of the processes

and immature techniques indicate that there is a long way to go before they can be adopted in large-scale manufacturing.

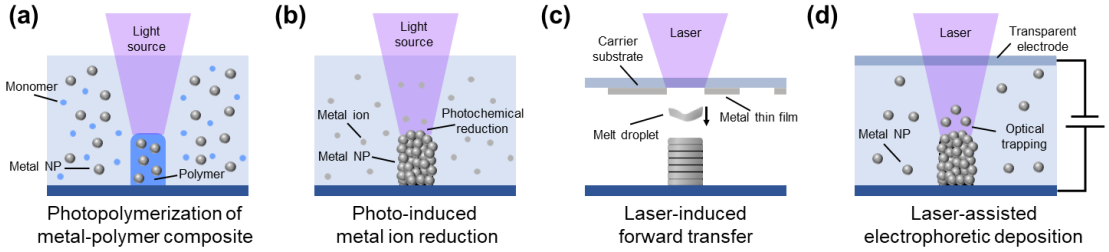

Figure 1.5 Schematics of different photo-induced metal printing processes. (a) Photopolymerization of metal nanoparticle-polymer composite. (b) Photo-induced photoreduction of metal ions. (c) Laser-induced forward transfer of metallic thin film. (d) Laser-assisted electrophoretic deposition of metal nanoparticles.

1.5 Motivation and Scope of Research

The adoption of DLP printing in various industries has been reshaping global manufacturing. It has enabled faster prototyping and production of highly customized and complex parts, simplified fabrication process, and largely reduced production time and cost. DLP printing has brought significant impacts on automotive, consumer, healthcare and industrial, and it is expected to bring broader influence. Despite of the achievement of DLP printing, challenges and potentials remain ahead. This dissertation will focus on the fabrication of various functional materials with DLP printing, to explore the potential benefits and the possible applications of DLP printing in biomimetic study, soft robotics, and flexible electronics manufacturing.

The first part of the dissertation will focus on 4D printing of hydrogels. 4D printing platforms based on different stimuli-responsive hydrogels were developed and

investigated, which would benefit the biomimetic study and soft robotics research.

The second part of the dissertation will focus on the metal printing. Gold and liquid metal circuits were printed with DLP lithography based on different mechanisms. A wide range of applications of the printed metals were demonstrated.

Based on the projects completed, this dissertation is divided into six chapters:

Chapter 1 provided a brief introduction of various additive manufacturing techniques. The state of the art and the challenges of 4D printing and photo-induced metal printing via AM were generally reviewed.

Chapter 2 showcased the visualization of morphogenesis through instability via 4D printing. Core-shell heterogeneous hydrogel structures were printed to replicate the distinct circumferential buckling formation in pumpkins. The 4D printing platform was demonstrated for mimicking the morphologic transformation of various plants.

Chapter 3 presented the 4D printing of a thermoresponsive tough hydrogel. The adaption of hydrogel toughening to 3D printing platform enabled the printability of tough hydrogels. With the improved toughness and thermoresponsiveness of the printed hydrogels, various soft actuators with high actuation power were demonstrated.

Chapter 4 introduced the room-temperature annealing-free gold printing via anion-assisted photochemical deposition. One-step patterning of gold nanoparticles network with tunable morphology and electrochemical properties was achieved. Owing to the high electrical conductivity and conformability, the printed gold was demonstrated as reliable bioelectrodes for electrophysiological signal delivery and acquisition.

Chapter 5 presented the fast and facile liquid metal printing strategy for highly

stretchable electronics circuits. A liquid metal particles dispersion ink was developed, enabling photo-patterning of metallic traces on various substrates. With high electrical conductivity and excellent electromechanical performance, the printed liquid metal circuits were demonstrated for applications in various wearable electronics and soft robotics.

Chapter 6 summarized the dissertation and provides an outlook for the research and applications of DLP printing in the future.

1.6 Reference

[1] S. C. Ligon, R. Liska, J. Stampfl, M. Gurr, R. Mülhaupt, *Chem Rev* **2017**, 117, 10212.

[2] Y. Lu, G. Mapili, G. Suhali, S. Chen, K. Roy, *J Biomed Mater Res A* **2006**, 77, 396.

[3] J. R. Tumbleston, D. Shirvanyants, N. Ermoshkin, R. Janusziewicz, A. R. Johnson, D. Kelly, K. Chen, R. Pinschmidt, J. P. Rolland, A. Ermoshkin, E. T. Samulski, J. M. DeSimone, *Science* **2015**, 347, 1349.

[4] D. A. Walker, J. L. Hedrick, C. A. Mirkin, *Science* **2019**, 366, 360.

[5] B. E. Kelly, I. Bhattacharya, H. Heidari, M. Shusteff, C. M. Spadaccini, H. K. Taylor, *Science* **2019**, 363, 1075.

[6] M. Shusteff, A. E. M. Browar, B. E. Kelly, J. Henriksson, T. H. Weisgraber, R. M. Panas, N. X. Fang, C. M. Spadaccini, *Science Advance* **2017**, 3, eaao5496.

[7] A. Ahmed, S. Arya, V. Gupta, H. Furukawa, A. Khosla, *Polymer (Guildf)* **2021**, 228, 23926.

[8] X. Kuang, D. J. Roach, J. Wu, C. M. Hamel, Z. Ding, T. Wang, M. L. Dunn, H. J. Qi, *Adv Funct Mater* **2019**, 29, 1.

[9] A. Lendlein, O. E. C. Gould, *Nat Rev Mater* **2019**, 4, 116.

[10] M. Zarek, M. Layani, I. Cooperstein, E. Sachyani, D. Cohn, S. Magdassi, *Advanced Materials* **2016**, 28, 4449.

[11] Q. Ge, A. H. Sakhaei, H. Lee, C. K. Dunn, N. X. Fang, M. L. Dunn, *Sci Rep* **2016**, 6, 31110.

[12] I. A. Rousseau, P. T. Mather, *J Am Chem Soc* **2003**, 125, 15300.

[13] D. J. Roach, X. Kuang, C. Yuan, K. Chen, H. J. Qi, *Smart Mater Struct* **2018**, 27, 125011.

[14] A. Kotikian, R. L. Truby, J. W. Boley, T. J. White, J. A. Lewis, *Advanced Materials* **2018**, 30, 1706164.

[15] Z. Wang, Y. Guo, S. Cai, J. Yang, *ACS Appl Polym Mater* **2022**, 4, 3153.

[16] S. Li, H. Bai, Z. Liu, X. Zhang, C. Huang, L. W. Wiesner, M. Silberstein, R. F. Shepherd, *Sci. Adv* **2021**, 7, 3677.

[17] M. Tabrizi, T. H. Ware, M. R. Shankar, ACS Appl Mater Interfaces **2019**, 11, 28236.

[18] D. E. Hagaman, S. Leist, J. Zhou, H. F. Ji, *ACS Appl Mater Interfaces* **2018**, 10, 27308.

[19] C. Yuan, D. J. Roach, C. K. Dunn, Q. Mu, X. Kuang, C. M. Yakacki, T. J. Wang, K. Yu, H. J. Qi, *Soft Matter* **2017**, 13, 5558.

[20] D. Han, C. Farino, C. Yang, T. Scott, D. Browe, W. Choi, J. W. Freeman, H. Lee, *ACS Appl Mater Interfaces* **2018**, 10, 17512.

[21] D. Han, Z. Lu, S. A. Chester, H. Lee, *Sci Rep* **2018**, 8, 1963.

[22] J. Guo, R. Zhang, L. Zhang, X. Cao, *ACS Macro Lett* **2018**, 7, 442.

[23] A. Sydney Gladman, E. A. Matsumoto, R. G. Nuzzo, L. Mahadevan, J. A. Lewis, *Nat Mater* **2016**, 15, 413.

[24] Z. Zhao, J. Wu, X. Mu, H. Chen, H. J. Qi, D. Fang, *Macromol Rapid Commun* **2017**, 38, 1600625.

[25] M. Champeau, D. A. Heinze, T. N. Viana, E. R. de Souza, A. C. Chinellato, S. Titotto, *Adv Funct Mater* **2020**, 30, 1910606.

[26] J. M. Taylor, H. Luan, J. A. Lewis, J. A. Rogers, R. G. Nuzzo, P. v. Braun, *Advanced Materials* **2022**, 34, 2108391.

[27] Z. Li, Y. Zhou, T. Li, J. Zhang, H. Tian, *VIEW* **2022**, 3, 20200112.

[28] J. Liang, K. Tong, Q. Pei, *Advanced Materials* **2016**, 28, 5986.

[29] Q. Huang, K. N. Al-Milaji, H. Zhao, *ACS Appl Nano Mater* **2018**, 1, 4528.

[30] X. Yang, M. Sun, Y. Bian, X. He, *Adv Funct Mater* **2019**, 29, 1.

[31] Z. Zhao, J. Bai, Y. Yao, C. Wang, *Materials Today* **2020**, 37, 10.

[32] T. Tanaka, A. Ishikawa, S. Kawata, *Appl Phys Lett* **2006**, 88, 1.

[33] Y. Y. Cao, N. Takeyasu, T. Tanaka, X. M. Duan, S. Kawata, *Small* **2009**, 5, 1144.

[34] E. Blasco, J. Müller, P. Müller, V. Trouillet, M. Schön, T. Scherer, C. Barner-Kowollik, M. Wegener, *Advanced Materials* **2016**, 28, 3592.

[35] M. Zenou, A. Sa'Ar, Z. Kotler, *Small* **2015**, 11, 4082.

[36] M. Zenou, A. Sa'ar, Z. Kotler, *Sci Rep* **2015**, 5, 17265.

[37] T. Takai, H. Nakao, F. Iwata, *Opt Express* **2014**, 22, 28109.

Chapter 2. 4D printing of hydrogel for visualizing morphogenesis

2.1 Introduction

Different biological species differ from one another by their unique morphologies. While the embryonic development of each species or organ starts with a similar profile during growth, different morphologies eventually develop in their matured state. This biological process is termed morphogenesis. As part of the process, surface patterns and textures form across many length scales. For example, centimeter-scale cortical convolutions and groovy patterns on fruits,[1-2] millimeter-scale fingerprints,[3] and even micrometer-scale features on buckled tumor surfaces[4] and crumpled membranes of white blood cells.[5] The underlying mechanism of the morphology development, as a synergistic result of complicated biological, biochemical and mechanical processes, is not yet fully understood.[6] Therefore, this unique yet common phenomenon is still of great importance and interest to biologists, materials engineers and mechanics scientists. Understanding how different organisms evolve from similar, featureless immature states, usually embryos, into highly differentiated mature products would be meaningful for plant breeding in agricultural development, and in the biomedical field for diagnosis and treatment.[5, 7] Fundamentally, such 3D-structure evolution processes would also aid the development of complex dynamic mechanical theories and shed light on the design of structural materials.

To understand the complex process of morphogenesis, extensive research and investigation have been conducted from the molecular, genetic and cellular perspectives by biologists and botanists. Alternatively, other scientists take a macroscopic approach by studying the phenomena on the basis of mechanics and

mathematics. The complicated biological tissue structures are usually abstracted into elastic or hyper-elastic material models to study their fundamental stress and strain development.[2, 8-13] Generally, different morphologies can be achieved via the formation of various surface patterns of mechanical instability during external loadings. The surface of the material would remain smooth until the applied compressive stress exceeds a critical value. Upon surpassing the threshold, buckling would occur on the surface of the material, characterized by the sudden localized deflection on the surface. To maintain a minimized free energy, undulation patterns will gradually develop across the surface of the material with the build-up of stress.

Based on the conventional instability theories, various theoretical calculations and finite element method (FEM) models have been developed to explain the formation of different morphologies during morphogenesis. Chen *et al.* have reported a quantitative mechanics framework of stress-driven anisotropic buckling on model spheroidal shell/core (film/substrate) systems. They approximated various natural fruits and vegetables as spheroidal stiff exocarp (shell)/ compliant sarcocarp (core) systems, which exhibit intriguing buckling profiles.[2, 14] Dervaux *et al.* have studied the circumferential deformation of a free hyper-elastic disk mimicking the growth of a green algae.[15] Suo *et al.* have investigated the crease formation of soft tissue growing inside a rigid shell or outside a rigid core.[8]

To aid the theoretical development, active/responsive materials, which undergo volume and/or property changes in response to environmental stimulus, have been utilized for experimental validation of morphogenesis models. For example, Ben Amar *et al.*

utilized two different hydrogels with large distinction in swelling ratios to validate their model of shape transition in melanoma.[9] 3D printing technology has also been adopted for the facile fabrication of the material models. The combination of 3D printing and responsive materials are often referred to as 4D printing, with time being the fourth dimension. 4D printing technology has been widely used to achieve various morphologies and intelligent behaviors. Shape-memory polymer fibers in elastomeric matrix were printed to be used as intelligent hinges to enable origami folding patterns such as box, pyramid and airplanes.[16] Simple homogeneous tubular hydrogel structures with one end fixed have been fabricated by using DLP 3D printing for the investigation of their buckling formation due to their instability.[17] Complex heterogeneous dual-gel bioinspired tubes were recently reported to achieve periodical buckling and intelligent behavior such as elongation and gripping.[18-19] Anisotropic hydrogel composites were reportedly applied in 4D printing of different biomimetic architectures, including a native orchid and a native calla lily flower.[20] In accordance to the prior 4D printed structures, anisotropy in the materials' stimuli-responsive behavior is essential to achieve programmable intelligent performance.[21]

2.2 Proposed Method

Most studies of 4D printing focus on the transformation from 1D rods or 2D layered structures into 3D structures, while the time-dependent transformation starting from 3D structures are relatively less reported.[20, 22-23] With the understanding that biological tissues are complex in both geometry and structure, we were inspired to take advantage

of 4D printing fabrication to visualize and elucidate the morphogenetic mechanisms of various plants' organs. Essentially, we combined digital light processing (DLP)-based 3D printing technology with stimuli-responsive hydrogels to 4D print a heterogeneous core-shell dual-gel structure that geometrically and structurally imitates the pumpkin fruit. The materials model mimics the growing process of pumpkins as the hydrogel swells and gradually develops pumpkin-like morphology. Thus, the 4D printed model can be used to monitor morphology evolution during its "growth" and shed light on the underlying morphogenesis mechanism. In the model, the less swellable, stiff core emulates the central part of the fruit which consists of fibrous strands wrapping the seeds and two pole ends. The faster-swelling, soft shell mimics the soft mesocarp of the fruit where growth and volume expansion is most significant. The buckling wavelength, which determines the number of ridges and grooves on the "pumpkin" surface, can be readily tuned by controlling the expansion mismatch between the core and the shell. To the best of our knowledge, in this work, the time dependent development of periodic buckling from initiation site to the entire surface is studied for the first time. This work elucidates the prerequisites, mechanisms, and the dynamic process of buckling on a 3D, heterogeneous, self-confined object without external boundary, resembling natural fruits geometrically. This is anticipated to contribute to the understanding of previously commonly studied buckling of uniform objects with boundary confinement.

2.3 Experimental and Characterization Section

2.3.1 Materials

Acrylic acid (AAc), N,N'-methylene-bis-acrylamide (MBA), Sudan I dye and phenylbis(2,4,6- trimethylbenzoyl)phosphine oxide (Irgacure-819) were purchased from Sigma-Aldrich, Inc. Dimethyl sulfoxide (DMSO) solvent, ethanol, 0.05M pH 7.00 dihydrogen potassium phosphate-sodium phosphate dibasic buffer solution and 0.05M pH = 4.00 potassium biphthalate buffer solution, hydrochloric acid solution were purchased from Fisher Scientific Inc. All chemicals were used without further purification and treatment.

2.3.2 Preparation of Printing Precursor

To prepare the precursor solution for the 3D printing process, 24wt% AAc as the monomer; 3.6wt% MBA as the crosslinker, 0.6wt% Sudan I dye as the photo absorber, and 0.2wt% Irgacure-819 as the photo initiator were mixed in 47 g of DMSO solvent. The mixture was vortexed and then ultrasound treated for 10 minutes, producing a clear reddish precursor solution. This solution was used for printing all the hydrogels described in this work. Additionally, ethanol was used to rinse the samples and a 0.05M pH = 7.00 dihydrogen potassium phosphate-sodium phosphate dibasic buffer solution was used as the swelling agent for the printed hydrogels for accurate control of the medium condition in all experiments.

2.3.3 Photolithography System

The printing was accomplished by a home-made, DLP-based 3D printing system as shown in **Figure 2.1**a. The system was composed of a PRO4500 UV light (385 nm) projector from Wintech Digital System Technology Corporation, a motorized translation stage mounted to a motor controller, and other optical accessories from Thorlabs. The power density of the projected UV light is measured to be 2.0 mW/cm^2 by an ultraviolet light meter, Traceable® Products . A home-made program was used to realize the coordination control of the projection and the movement of stage. The resolution of the printer can achieve 30 μm on the x-y plane and 10 μm in the z-axis direction.

2.3.4 Printing and Swelling Process

The printing process was carried out in air under ambient condition. The printing precursor was cured by UV light layer by layer to print the 3D structure. A 3D computer-aided design (CAD) model was first designed and cut into a series of 2D patterns. The patterns were perpendicularly projected by the UV projector onto the stage, which was immersed in the precursor solution. To print a core-shell barrel structure, one large and one small concentric circles were projected sequentially for each layer. The larger circle was first projected for a short curing time of 3-4 s, followed by the projection of the small circle pattern for a longer curing time of 10s in total to form the rigid core. Once a layer was printed, the support plate moved down allowing the projector to print another layer upon the top of the printed ones. For all the samples with core-shell

structure, 50 layers were printed. The thickness of each layer was set to be 0.1 mm. Once the printing was completed, the as-printed hydrogel samples were rinsed in ethanol to remove the unreacted components and excess photo absorber. Then, the clear hydrogel samples were immersed in a 0.05 M pH = 7 buffer solution to swell, mimicking the growth process of pumpkins as shown in **Figure 2.1**.

2.3.5 Measurement of Swelling Ratios and Rates

Thin discs of hydrogels of 2.1 cm diameter and 2 mm thickness were printed with various curing times to measure the swelling ratios of the printed hydrogels. As printed, the samples were first rinsed with ethanol to wash away the unreacted monomers and dyes. Then, they were put into pH = 7 buffer solution to swell for 6 hr. The changes in the discs' diameters over time were measured to calculate the linear swelling ratios, which were then cubed to obtain the volumetric swelling ratio of the hydrogels.

2.3.6 Measurement of Modulus

To measure the Young's modulus of the printed hydrogels with different curing time, 15-layer samples in dog-bone shape were printed with various curing times (3 to 20 seconds per layer), rinsed with ethanol to get rid of unreacted monomers and extra dye, and then dried in an oven. Dynamic Mechanical Analysis (DMA850, TA Instruments) was used to measure the stress-strain curves of the printed samples. The moduli were obtained as the slope of the stress-strain curves.

2.3.7 Characterization of the Microstructures

Scanning electron microscope (SEM) was used to study the microstructures of the printed samples. The SEM images are obtained by using ZEISS Supra 40VP SEM. To prepare the samples for SEM imaging, the gels were first immersed in the buffer solution until they fully swelled. Then, they were frozen by using liquid nitrogen and left in the freeze dryer (Labconco corporation, Freezone 1L) overnight. A gold thin film was sputtered onto the samples for the SEM imaging, using the PELCO®SC-7 auto sputter coater.

2.3.8 Simulation

The shape transition of hydrogels is a transient process, which mainly involves large deformation of the gel network and mass diffusion of water into/out of the gel. To model this complicated behavior, the inhomogeneous field theory that couples large deformation and mass diffusion were implemented in the environment of commercial multi-physics modeling software COMSOL.[24-25]

2.4 Results and Discussion

2.4.1 Material and Structure Design

As the most versatile class of stimuli-responsive materials, hydrogels can undergo significant volumetric changes in response to various types of stimuli, such as pH, temperature and humidity. Notably, the swelling ratio and mechanical performance of hydrogels can be easily tailored by tuning the chemical composition and the

microstructure of the network. In this study, we 4D printed a poly (acrylic acid) (PAAc) hydrogel structure to serve as our material model. The hydrogel consists of crosslinked alkyl chains as the backbone and carboxyl groups extending outward from the backbone, thus driving its swelling in an environment of pH greater than the pKa of the polymer (reported pKa for acrylic acid is 4.3).

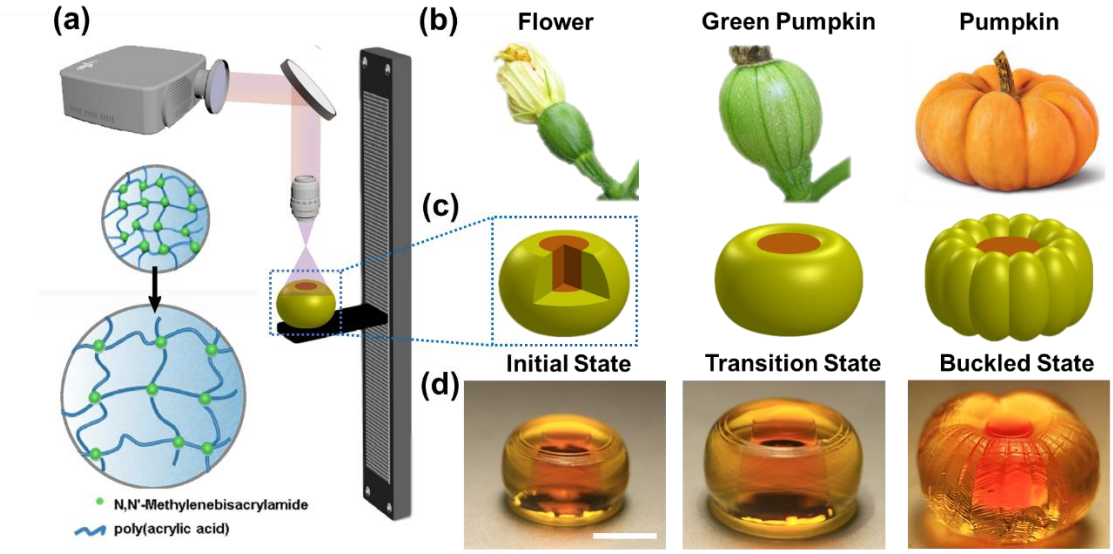

Figure 2.1 (a) Schematic of projection micro-stereolithography system; (b) growth of pumpkin and (c) corresponding schematic diagram; (d) pictures of the printed hydrogel structure during the swelling process. Scale bar in (d) is 5mm.

The schematic of projection micro-stereolithography system used to print hydrogel structures in our work as shown in **Figure 2.1**a. The detailed printing setting and procedures have been described in the experimental section. A computer-aid design (CAD) model with a profile shown in **Figure 2.2** was used. Firstly, we printed a baby-pumpkin-like, heterogeneous hydrogel structure (henceforth referred to as "the

pumpkin model") with coherent core and shell, as illustrated in the sectional figure in **Figure 2.1**c. The pumpkin model consists of a core cured for longer time (10s), marked in orange, and a circumferential shell cured for shorter time (3.5s), marked in green. This printing profile generates a highly swellable soft shell and a less swellable stiff core. Also, in the design, the core-shell radius ratio varies from 0.53 for the top and bottom layers at the two polar ends (pumpkin stem and base) to 0.4 at the equatorial layer throughout the total 50 layers of the entire model. It should be noted that, since the pumpkin model is printed layer by layer, interlayer horizontal lines remain visible in both the as-printed state and swollen state of the pumpkin model in **Figure 2.1**d. These horizontal layered features are intrinsically different from the vertical circumferential ridges and grooves formed during the "growth" of the pumpkin model, and therefore, neglected in our observation of the buckling. In the initial state, the surface of the pumpkin model is smooth, corresponding to the flowering stage of real pumpkins as shown in **Figure 2.1**b. As the pumpkin model is triggered to swell in a pH = 7 buffer solution, water starts to diffuse into the hydrogel networks and the pumpkin model will gradually swell. During this transition state, still no circumferential features are formed on the pumpkin model, which corresponds to the young, green pumpkin stage that takes place after the flower has withered. Eventually, the pumpkin model develops visible periodic ridges and grooves across the surface after 4 hours of "growth" mediated by the buffer solution, as the shell buckles under the constraint of the core. The circumferential buckling features run continuously from one end of the pumpkin model to the other, corresponding to the mature stage in a pumpkin's life cycle.

Through this process, the swelling evolution of the pumpkin model successfully mimics the morphogenesis of the pumpkin, starting from a feature-less, barrel-like geometry and gradually developing into the final structure of periodic grooves and ridges.

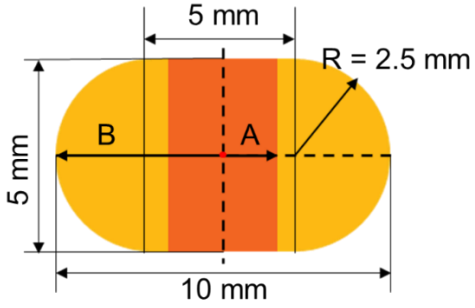

Figure 2.2 Profile of the CAD model. The core-shell radius ratio is tuned by the radius of the core, A, which is the only varying parameter in this profile. The core-shell ratio of the model (A/B) varies from 0.2 to 0.6 in this work.

2.4.2 Tunable Buckle Formation

To gain insight on the mechanism of the buckle formation, we first verified the role of the heterogeneity induced by the core-shell structure. A homogeneous control sample with no core-shell structure, fabricated with 3s-curing per layer, was compared side by side with the pumpkin model fabricated with a printing profile of 10s-curing for the core and 3s-curing for the shell in each layer, as shown in **Figure 2.3**a,b. The two samples were allowed to swell to comparable ratios in the same media. The homogeneous structure remained smooth, while circumferential buckling developed across the surface of the pumpkin model with heterogeneous structure after 4 hours of swelling. This indicates that the imposed heterogeneity is crucial for the formation of

periodic grooves and ridges on the material's surface. This heterogeneity enhances the strain mismatch between the superficial and in-depth part of the model which helps to facilitate the buckling formation on the surface. Dimensional and mechanical ratios of heterogenous structures are commonly considered to govern the formation of buckling.[2, 8] With our heterogeneous pumpkin model, we have further investigated the influence of three significant factors on the buckle formation: the mismatch of core/shell swelling and core/shell moduli, as well as the ratio of core/shell radii.

We have verified that the modulus mismatch and self-imposed strain mismatch during swelling of the pumpkin model governs the formation of periodic buckling of its surface by systematic modulation of the material's properties. By tuning the curing time of each layer, materials fabricated with our system can exhibit drastically different moduli and swelling ratios using the same precursor, as shown in **Figure 2.3**c, d. For instance, the modulus for a hydrogel with 3s curing time per layer is ~ 9 kPa, while modulus for a 10s sample is ~295 kPa. Similarly, samples with layer exposure time of 3s led to an increase of 77% in diameter, but only 38% for hydrogel with 10s curing time per layer. The mechanical results were also supported by the microstructure analysis in **Figure 2.3**e. Layers with exposure time of 3s showed a pore size of about 20 μm, while 10s exposure time produced a pore size of around 5μm. Therefore, high dynamic ranges of modulus ratios and swelling ratios between the core and the shell could be realized by simple adjustment of the respective curing time of each part. Modulus mismatch of up to 70-fold and swelling ratio mismatch of up to 60% could be achieved in a single run of the printing process.

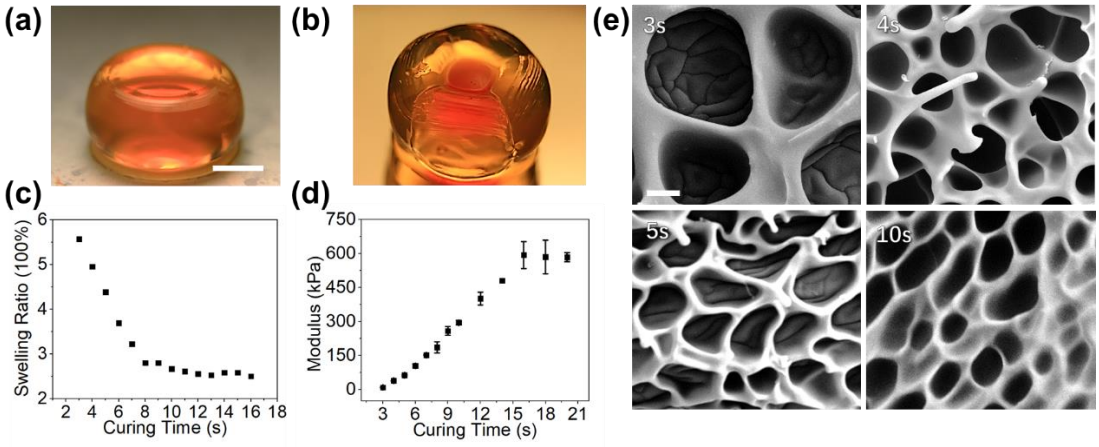

Figure 2.3 (a) A 3s-cured homogeneous structure and (b) a heterogeneous pumpkin model with a 3s-cured shell and a 10s-cured core; (c) a plot of volumetric swelling ratio versus curing time and (d) a plot of modulus versus curing time of the homogeneous hydrogels; (e) SEM images of the microstructures in the hydrogels with different curing time (3s, 4s, 5s, 10s). Scale bars in (a) and (b) are 5 mm, in (e) is 5 μm.

Based on the precise controllability and tunability of stiffness and swelling ratio, we fabricated a series of pumpkin models with different modulus mismatch and strain mismatch in the swollen state, as shown in **Figure 2.4**a-c, e-g, i-k. We used the same CAD pumpkin model with a fixed core-shell radius ratio of 0.4 on its equatorial plane for the printing. A constant curing time of 10s for the core is set, while the curing time for shell is varied from 3s to 3.5s and 4s, to create less swellable shells and thus decreasing core/shell modulus mismatch and strain mismatch. After 4 hours of immersion in the pH = 7 buffer solution, all three samples generated circumferential buckling extending from top to bottom and across the entire surface. The wavelength of the circumferential buckling decreases significantly with the decrease in modulus and strain mismatch. The number of ridges on the 3s-10s (shell curing time – core

curing time) pumpkin model is ~4, while for the 3.5s-10s pumpkin model the number increased to ~22, and for the 4s-10s model the number further increased to ~40. This is confirmed by finite element analysis of the cross-section at equator of the pumpkin model, as shown in **Figure 2.4**d, h, l, where a similar trend of buckling formation is observed.

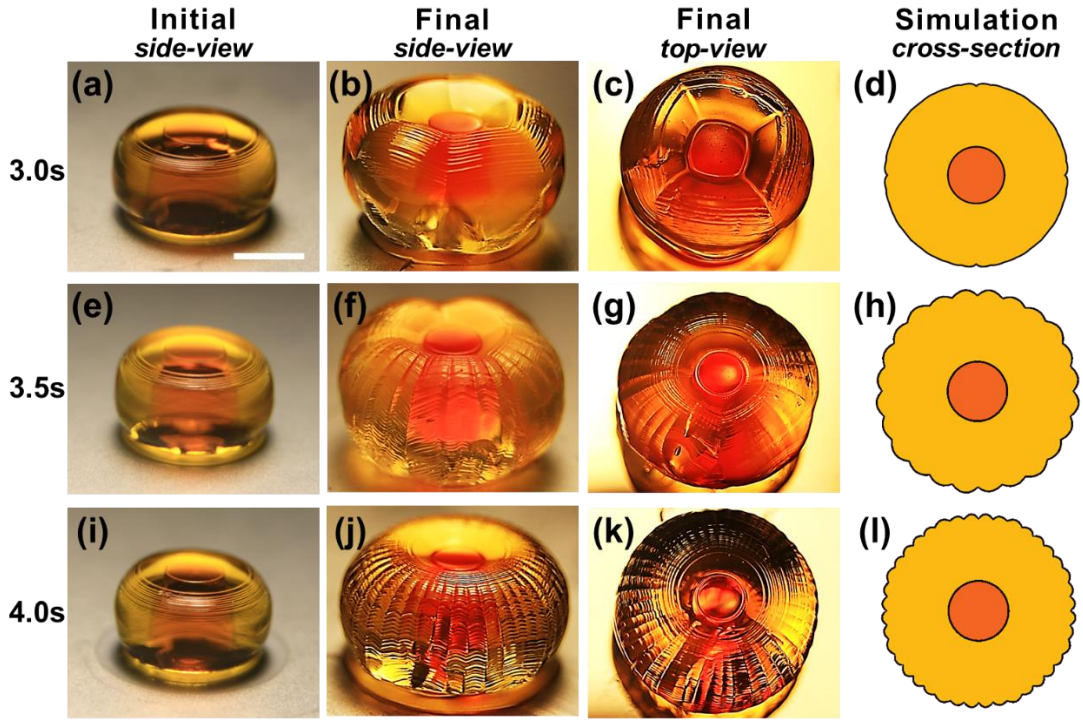

Figure 2.4 Initial state (a, e, i), final state side view (b, f, j) and top view (c, g, k), simulated results (cross-section) (d, h, l) of the printed pumpkin models with different shell curing time:3s, 3.5s, 4s respectively. Scale bar is 5 mm.

In the previous work reported by Yin *et al.*, it is studied and discovered that the radius ratio between the core and the shell plays an important role in the morphogenesis, especially for the number of buckling and grooves.[2] Therefore, we printed a series of pumpkin models with the core/shell radius ratio varied (0.2 ~ 0.6) and the curing times

fixed (3s for shell and 10s for core), to systematically study the influence of radius ratio on the number of grooves. Here, the radius ratio value, A/B, is defined by the two concentric circles at the equatorial layer at their initial state. We denote "A" as the radius of the core while "B" as the outer radius of the ring (shell), as shown in **Figure 2.5**f. The final-state morphologies of the series of 3s-10s pumpkin models with varying A/B from 0.2 to 0.6 are shown in **Figure 2.5**a-e. The wavelength of the circumferential buckling decreases with the increasing A/B. The number of ridges on a pumpkin model with A/B = 0.3 is ~4 (**Figure 2.5**b), while for the 0.5 ratio pumpkin model the number increases to ~6 with smaller ridges further forming on top of the 6 large ones (**Figure 2.5**d). As A/B increases to 0.6, the number of ridges increases to ~30 (**Figure 2.5**e). This is also confirmed by a similar analysis of the cross-section at the equator of the pumpkin model, shown in **Figure 2.5**f-j.

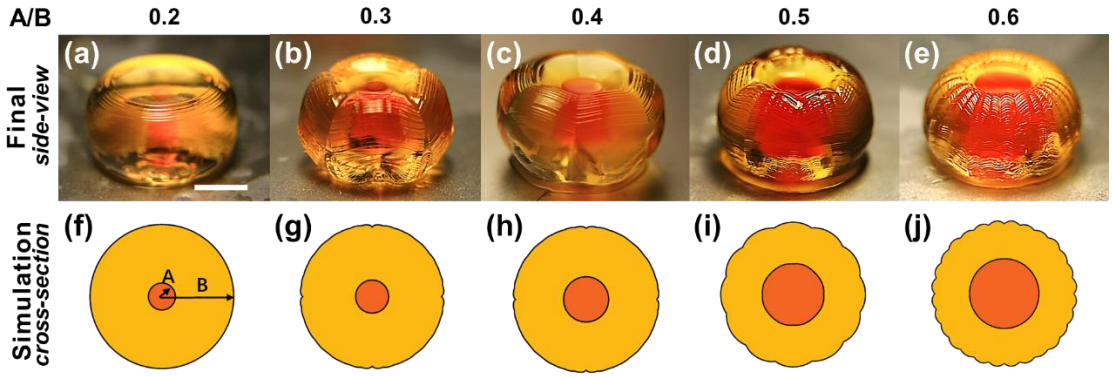

Figure 2.5 Printed pumpkin models of various core-shell radius ratios (A/B), all with 3s-cured shells and 10s-cured cores. The core-shell ratios are respectively: (a) 0.2; (b) 0.3; (c) 0.4; (d) 0.5 and (e) 0.6. (f-j) Corresponding simulation results of the cross-section at the equatorial plane. Scale bar is 5 mm.

2.4.3 Buckling Mechanism

To study the dynamic development process of periodic buckling across the surface, time-lapse observation was carried out throughout the swelling process of the pumpkin model. A sample was printed with a shell cured for 4s and a core cured for 10s to capture the onset and propagation of the ridges formation due to buckling. In the first 3.5 hours of swelling, no buckling occurred on the surface. After being immersed in buffer solution for 3.5 hours, faint buckling features start to form at the two ends of the pumpkin model, extending radially from the core to surrounding shell, as shown in **Figure 2.6**a. At this stage, only the top few layers show buckling features and the rest of the surface remained smooth. The sudden formation of buckling features is attributed to the "snap through" aspect of buckling. Previously Jin *et al*. has reported an analytical study of a tubular, soft shell growing outside of a rigid core.[8] Based on their theory, here we further concluded the critical condition for the onset of circumferential buckling on the outer surface of the shell in our pumpkin model with both the core and the shell swelling, which is given as

$$g^3 \Big/ \left(\left(\frac{A}{B}\right)^2 - g^3 \left(\left(\frac{A}{B}\right)^2 - 1 \right) \right) = 2.4$$

where g is the relative growth ratio which is defined as $g = g_{shell}/g_{core}$, and A and B are the same radii as we have defined above.

Due to the swelling of both the core and the shell, a 2-step swelling process is proposed for the deduction of the equation as shown in **Figure 2.7**. The initial state, denoted as State I, is taken as stress-free. Both the core and shell are then assumed to swell to the same ratio, g_{core}, simultaneously and homogeneously to a stress-free State II. After

that, the core is assumed to fully swell while the shell will continue to grow. Therefore, the whole structure will reach a stressed State III eventually. The equation for the critical condition is based on the several assumptions: (1) the deformation of the hydrogel is taken as elastic and incompressible, which means that for a constant curing time, the growth ratio (swelling ratio) will be the same; (2) both the core and the shell grow homogeneously, so the growth ratio in the radial, circumferential, and longitudinal directions of the shell have the same value, $g_r = g_\theta = g_z$; (3) it is assumed that there is no deformation in the z direction. Thus, the critical relative growth ratio (*i.e.*, the threshold for buckling initiation), g, as a function of A/B can be plotted as **Figure 2.6**g. For a given A/B, the relative growth ratio needs to exceed a threshold for the buckling to occur, which is similarly observed in our experimental results.

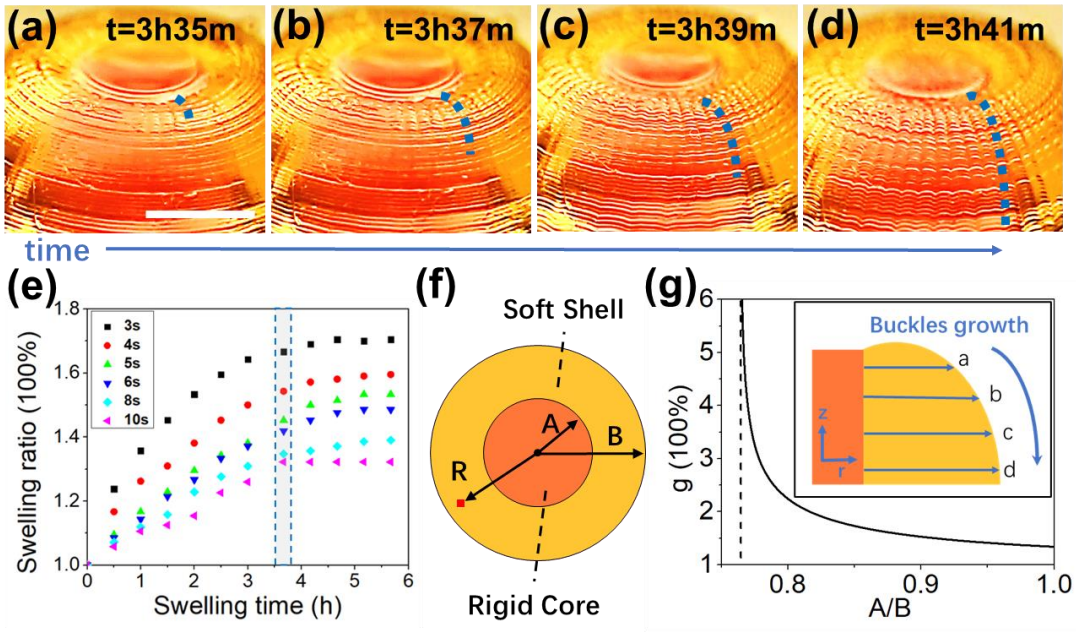

Figure 2.6 The buckles started to appear when the structure swelled to a critical level (a) and extended from the top to bottom (b, c) and eventually covered the surface of the structure (d); (e) the swelling ratios of hydrogels printed for different curing time (3s-

10s) as the function of time, with the shaded region indicating the time period when buckling occurs; (f) the schematic of the equatorial layer of the pumpkin model; (g) the critical relative growth ratio, g, as a function of core/shell radius ratio, A/B. Inset: schematic of the buckle growth which starts from top to equatorial plane, corresponding to (a-d). Scale bar is 5 mm.

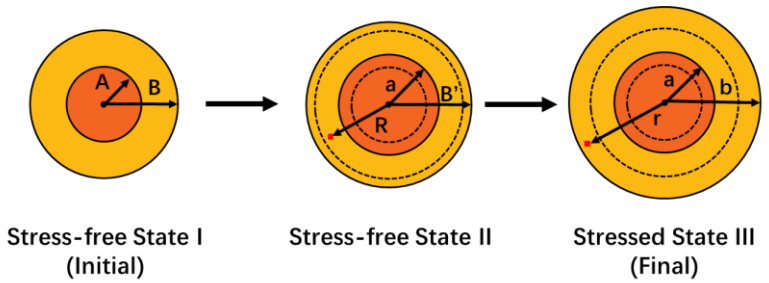

Figure 2.7 The swelling process: the initial stress-free State I; the stress-free State II after the homogeneous growth of the core and the shell with the same growth ratio, g_{core}; the final stressed state after the complete growth of the model.

At ~3.5 hours, the core has been fully swelled while the shell is still growing. The buckling formation and development occurred within the grey region in **Figure 2.6**e. Within a short period of time afterwards, the circumferential buckling ridges extend from the poles to the equator and eventually cover the entire surface of the pumpkin model, as progressively shown in **Figure 2.6**b-d. The length of formed ridges is marked with blue dashed lines for better illustration. This spatial and temporal evolution of the circumferential buckling patterns pose special interest for study. The reason why the buckling onset in the polar region is faster than the equator region can also be explained using the above equation. With a large A/B value, the critical relative growth ratio is

more readily achieved. Since the polar region has larger A/B (A/B = 5.3:10) than the equatorial region (A/B = 4:10), instability will first occur in the polar region. As the structure continues to swell, the regions away from the poles consecutively reach the critical condition for the onset of buckling, leading to the propagation of ridges extending from the two poles to the equator with the evolution of time, as illustrated in the inset of **Figure 2.6**g. However, the theoretical calculation predicts that the numbers of ridges formed should change with different core-shell ratios, whereas, for our pumpkin model with various core-shell ratios along the z axis, the number of ridges remains the same in every layer. This may result from the strong interaction between each layer as they are coherently jointed at each interface, thus additional strain energy would arise if different layers assume different numbers of ridges. Therefore, as the buckling occurs in previous layers along the propagation path, it will induce the subsequent layer to buckle in the same radial position to mitigate the excess interlayer strain energy. As a result, the printed layers with varying core-shell ratios synergistically display a single mode of buckling, where the buckling pattern runs continuously between the two poles.

As shown in the **Figure 2.6**g, it is predicted by the equation that the buckling occurred only if A/B is larger than $\sqrt{7/12}$, while in the experimental results shows a lower threshold of A/B for buckling formation. This can be attributed to the much more complex conditions of the experimental results. Due to the layer-by-layer additive manufacturing method, the growth of hydrogel structures, in practice, was not homogeneous in longitudinal and lateral directions. Besides, it was assumed that there

was no deformation in z direction, for the convenience of calculation. Other factors such as the model's height and the curvature of the shell have not been considered. Since several assumptions have been made to simplify the conditions in the analysis, challenges to fully understand the mechanism behind the buckling formation still remain and more investigation is under way. A primary exploration has been conducted by tuning the deformation gradient in z direction, λ_z. If $\lambda_z < 1$, it can describe a condition that a compressive stress is applied at the two poles of the model to force it to shrink in z direction. By introducing the deformation gradient in z direction, the critical condition of buckling can be rewritten as

$$g^3B^2/(\lambda_z(g^3(B^2 - A^2) + A^2)) = 2.4$$

As shown in **Figure 2.8**, such a compression will eventually lead to a lower threshold of A/B for buckling initiation as well as a lower critical relative growth ratio, which is much consistent with the experimental results. Although the pumpkin model in present experiment did not shrink in z direction, this analytical result confirms the significant influence of the constrain from the polar ends. In addition, wrinkling of pressurized elastic shells, which are similar periodical buckling of our model, has also been reported.[26] As far as it goes, the buckling formation of the pumpkin model is attributed to the mismatch between the core and the shell in swelling ratio and modulus, as well as the constraint boundary at the two ends. As long as the critical conditions of buckling formation are met, circumferential buckling can also form on the surface of a printed pumpkin model with a hollow core as shown in **Figure 2.9**, which more closely resembles the structure of a real pumpkin.

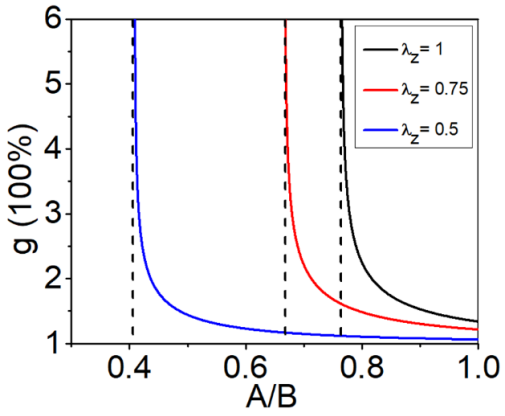

Figure 2.8 The critical relative growth ratio, g, for onset of the surface buckling as a function of A/B for isotropic growth with different deformation in z direction. (black: $\lambda_z = 1$; red: $\lambda_z = 0.75$; blue: $\lambda_z = 0.5$).

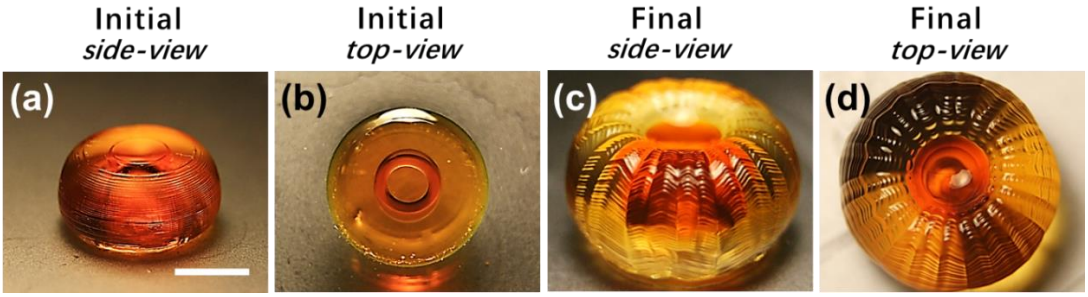

Figure 2.9 The images of the printed pumpkin model with a hollow core, specifically a 4s-cured shell and a 10s-cured closed-tube core: (a) side-view, (b) top-view of the initial state; (c) side-view and (d) top-view of the final state. Similar buckling formed with such a hollow-core structure as well, proving that the key factors for buckling are swelling mismatch and polar constrain, regardless of the filling of the core. The core-shell ratio of the model is 6/10. The radius ratio of the tubular core is 5/6. The hollow part ranges from the 11st to the 40th layer while the other layers are solid. Scale bar is 5 mm.

2.4.4 Morphological Transformations in Biomimetic Structures

Apart from mimicking the morphogenesis of the Cucurbita species like pumpkins, we have also applied our platform to mimic the morphogenesis of other fruits and vegetations.[27-31] For example, the curvy edges of cabbage, bent flower petals, and twisted bean shells. To mimic cabbages, we printed a core-shell hetero-structured thin disc out of the same hydrogel materials, as shown in **Figure 2.10**a. The swelling (strain) mismatch between the 3s-cured soft shell and the 10s-cured hard core, after 2 minutes of swelling in buffer solution, led to the formation of the cabbage-leaf-like wavy morphology as shown in **Figure 2.10**b. For mimicking flower petals, we printed a double-layer hetero-structure as shown in **Figure 2.10**e. The bottom 4 layers of the petals were printed for 3s while the top 2 layer were printed for 8s. The difference in swelling ratios between the two layers in response to water allows the petals to act as a bilayer actuator bending to the center, which mimics the morphology of chrysanthemum. Besides core-shell structures and bilayer structures, distinct plant morphologies can also be controllably formed by placing stiff lines in a soft film. In **Figure 2.10**i, we printed a leaf-shape structure with a soft mesophyll and a stiff vein inside. After immersion in buffer solution for 2 minutes, the printed leaf will turn into a curved profile as shown in **Figure 2.10**j. In addition, a soft strip with 45-degree oriented, stiff slash lines embedded was printed and developed into a helix structure similar to Bauhinia pods, as shown in **Figure 2.10**m, n. The matrixes were cured for 4s while the veins were printed for 15s for both structures. The simulations of the four different structures shown in **Figure 2.10**c, g, k, o show equivalent results as the

experimental ones, which closely resembled the natural organisms as shown in **Figure 2.10**d, h, l, & p. This further verified the geometry evolution of the 4D printing designs and processes. By designing heterogeneous structures with tunable modulus mismatch and swelling mismatch, we can controllably fabricate heterogeneous structures to mimic the morphogenesis and reproduce the morphologies of various plants.

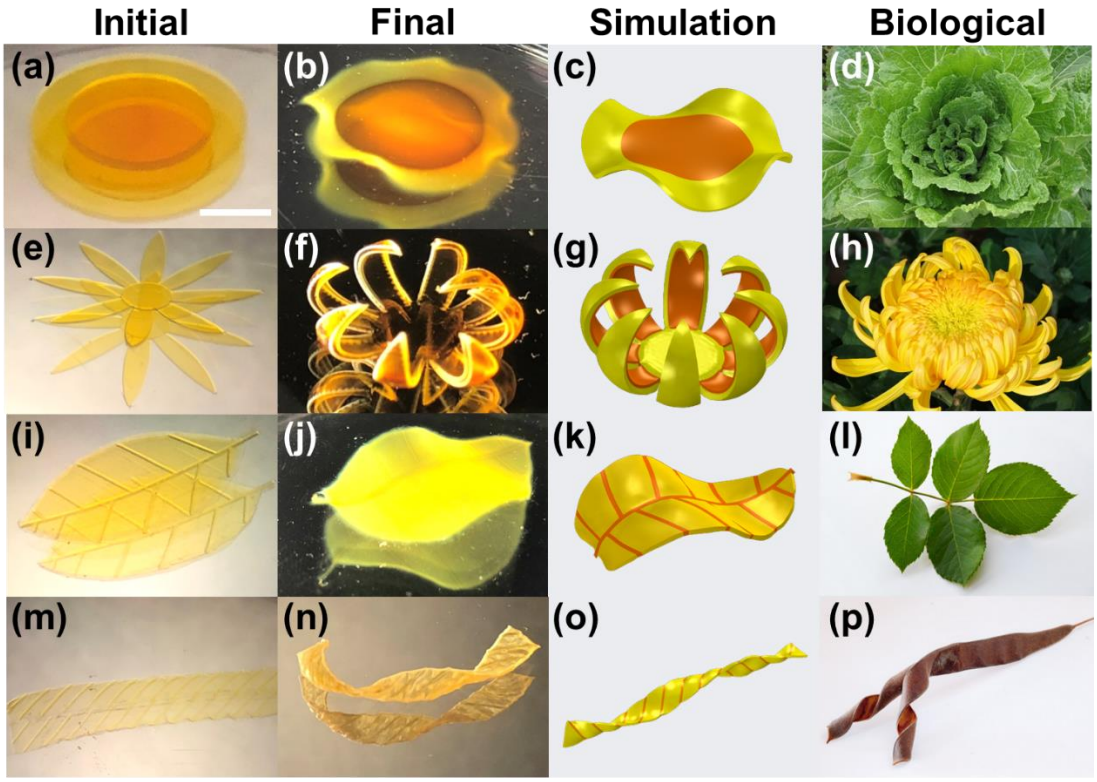

Figure 2.10 Morphologic transformation of different printed biomimetic structures: the initial plain structures (a, e, i, m) were printed and rinsed with ethanol, then immersed in water to allow them to develop into their final states (b, f, j, n). The simulated models (c, g, k, o) and the images of real cabbage flowers/leaves (d), chrysanthemum (h), leaves of rose (l) and helix strips of Bauhinia pods (p) indicate the corresponding emulation of their 3D geometrical morphologies evolved from the pre-designed 2D heterogeneous structures. Scale bar is 5 mm.

2.5 Conclusion

In summary, by 4D printing a hetero-structured material that structurally and geometrically represents pumpkins, we have successfully mimicked the morphogenesis of pumpkins, a complex spatiotemporal evolution that starts from a feature-less, barrel-like geometry and gradually develops into a final structure with periodic grooves and ridges. We have evaluated the importance of heterogeneity in morphogenesis with our model. Furthermore, we have explored the governing parameters of the produced patterns by taking advantage of 4D printing, which allowed for achieving a large range of modulus mismatch and strain mismatch, as well as tunable core/shell radius ratios. Assumptions have been utilized to understand the mechanism of the buckling formation in a simplified way. The present differences between experimental results and analytical calculation indicate that challenges remain, and the further investigation is underway. We have also demonstrated that the platform could be used for mimicking the morphogenesis of a wide selection of plants. The swelling process of our printed models presents a synthetic morphogenesis, which can help shed light on the mechanism behind the practical morphological formation of natural plants and extend the understanding of complex mechanics of heterogeneous high-dimensional dynamic architectures. This extension of the knowledge opens a new access to the design and fabrication of previously unachievable complex 3D architectures, and the studies and control of the biological tissues and organs. Printable biocompatible hydrogels with intellectual behaviors are significant to the development of soft robotics and artificial

tissues and organs. It will also benefit broad agricultural, soft robotics, and additive manufacturing fields.

2.6 Reference

[1] Liu, Y.; Yang, X.; Cao, Y.; Wang, Z.; Chen, B.; Zhang, J.; Zhang, H. *Computers & Graphics* **2015**, 47, 68-77.

[2] Yin, J.; Cao, Z.; Li, C.; Sheinman, I.; Chen, X. *Proc. Natl. Acad. Sci. U. S. A.* **2008**, 105 (49), 19132-5.

[3] Yin, J.; Gerling, G. J.; Chen, X. *Acta Biomater* **2010**, 6 (4), 1487-96.

[4] Ciarletta, P. *Phys Rev Lett* **2013**, 110 (15), 158102.

[5] Wang, L.; Castro, C. E.; Boyce, M. C. *Soft Matter* **2011**, 7 (24), 11319.

[6] Mirabet, V.; Das, P.; Boudaoud, A.; Hamant, O. *Annu Rev Plant Biol* **2011**, 62, 365-85.

[7] Phillips, G. C. *In Vitro Cellular & Developmental Biology - Plant* **2004**, 40 (4), 342-345.

[8] Jin, L.; Cai, S.; Suo, Z. *EPL (Europhysics Letters)* **2011**, 95 (6), 64002.

[9] Dervaux, J.; Couder, Y.; Guedeau-Boudeville, M. A.; Ben Amar, M. *Phys Rev Lett* **2011**, 107 (1), 018103.

[10] Shahaf Armon, E. E., Raz Kupferman, Eran Sharon. *Science* **2011**, 333, 1726-1730.

[11] Savin, T.; Kurpios, N. A.; Shyer, A. E.; Florescu, P.; Liang, H.; Mahadevan, L.; Tabin, C. J. *Nature* **2011**, 476 (7358), 57-62.

[12] Li, B.; Cao, Y.-P.; Feng, X.-Q.; Gao, H. *Journal of the Mechanics and Physics of*

Solids **2011**, 59 (4), 758-774.

[13] Li, B.; Jia, F.; Cao, Y. P.; Feng, X. Q.; Gao, H. *Phys Rev Lett* **2011**, 106 (23), 234301.

[14] Yin, J.; Chen, X.; Sheinman, I. *Journal of the Mechanics and Physics of Solids* **2009**, 57 (9), 1470-1484.

[15] Dervaux, J.; Ben Amar, M. *Phys Rev Lett* **2008**, 101 (6), 068101.

[16] Ge, Q.; Dunn, C. K.; Qi, H. J.; Dunn, M. L. *Smart Materials and Structures* **2014**, 23 (9), 094007.

[17] Lee, H.; Fang, N. X. *J Vis Exp* **2012**, (69), e4457.

[18] Liu, J.; Liu, W.; Pantula, A.; Wang, Z.; Gracias, D. H.; Nguyen, T. D. *Extreme Mechanics Letters* **2019**, 30, 100514.

[19] Liu, J.; Erol, O.; Pantula, A.; Liu, W.; Jiang, Z.; Kobayashi, K.; Chatterjee, D.; Hibino, N.; Romer, L. H.; Kang, S. H.; Nguyen, T. D.; Gracias, D. H. *ACS Appl Mater Interfaces* **2019**, 11 (8), 8492-8498.

[20] Gladman, A. S.; Matsumoto, E. A.; Nuzzo, R. G.; Mahadevan, L.; Lewis, J. A. *Nat Mater* **2016**, 15, 413-418.

[21] Erol, O.; Pantula, A.; Liu, W.; Gracias, D. H. *Advanced Materials Technologies* **2019**, 4 (4), 1900043.

[22] Ding, Z.; Weeger, O.; Qi, H. J.; Dunn, M. L. *Materials & Design* **2018**, 137, 256-265.

[23] Xiao Kuang, D. J. R., Jiangtao Wu, Craig M. Hamel, Zhen Ding, Tiejun Wang, Martin L. Dunn, and Hang Jerry Qi. *Advanced Functional Materials* **2019**, 29, 1805290.

[24] Hong, W.; Zhao, X.; Zhou, J.; Suo, Z. *Journal of the Mechanics and Physics of Solids* **2008**, 56 (5), 1779-1793.

[25] Wang, X.; Zhai, Z.; Chen, Y.; Jiang, H. A Facile, *Extreme Mechanics Letters* **2018**, 22, 89-97.

[26] Vella, D.; Ajdari, A.; Vaziri, A.; Boudaoud, A. *Phys Rev Lett* **2011**, 107 (17), 174301.

[27] Liu, Z.; Swaddiwudhipong, S.; Hong, W. *Soft Matter* **2013**, 9 (2), 577-587.

[28] Forterre, Y.; Dumais, J. Materials Science. *Science* **2011**, 333 (6050), 1715-6.

[29] Stoychev, G.; Puretskiy, N.; Ionov, L. *Soft Matter* **2011**, 7 (7), 3277.

[30] Wu, Z. L.; Moshe, M.; Greener, J.; Therien-Aubin, H.; Nie, Z.; Sharon, E.; Kumacheva, E. *Nat Commun* **2013**, 4, 1586.

[31] Li, B.; Cao, Y.-P.; Feng, X.-Q.; Gao, H. *Soft Matter* **2012**, 8 (21), 5728.

Chapter 3. 4D printing of tough thermal-responsive hydrogels

3.1 Introduction

Stimuli-responsive hydrogels are widely used for soft actuators and soft robots due to their facile fabrication, diverse actuation modes, high degree of freedom during actuation.[1] Hydrogel actuators are seeing growing interests as under-water robots and biomedical tools in light of their excellent compatibility with aqueous and biological environment.[2–6] Among various stimuli-responsive polymeric actuators, thermo-responsive ones have attracted particular interest due to the easy induction of thermal energy in the material without compositional change to the system.[7,8] Poly(N-isopropylacrylamide) (PNIPAM) hydrogels are a representative example that exhibits distinct behaviors at temperatures above or below its lower critical solution temperature (LCST).[9] PNIPAM hydrogels absorb water and swell at a temperature below LCST and conversely expel water and shrink at temperature above LCST. PNIPAM based actuators have shown significant advantages over many other types of hydrogels due to remote powering and control capabilities when conjugated with photothermal / magnetothermal materials.[4,6,10]

Conventional hydrogels, especially PNIAPM hydrogels, are mechanically weak due to their low solid contents (70-98% water contents) and lack of energy dissipating mechanisms.[11–15] Their intrinsic softness and fragileness lead to low deliverable force[16,17] and large passive deformation upon contact when applied as actuators, which hinders their use in practical applications that involves high loads, abrupt impacts, and long-term services. Various methods such as forming double networks (DN),[12,18] having

dual crosslinking[19] and compositing[20–25] were introduced for toughening hydrogels. However, many tough hydrogels are incapable of actuation by ambient stimuli while maintaining high toughness, due to the consumption of stimuli responsive sites or immobilization by the secondary networks or stiff fillers during the toughening process. For PNIPAM hydrogels, some viable approaches utilized solvent exchanges that induced strong aggregation or collapse of polymer chains for combined strengthening and actuation.[26–33] These methods require replenishing the entire body of solvent for reverse actuation and therefore limit the working environment of actuators to finite-sized containers. Alternatively, electro-actuation and pneumatic / hydraulic actuation have been employed to actuate tough hydrogels,[5,34,35] which requires external powering and pumping systems to supply sufficient voltage or pressure.

Achieving high mechanical robustness and stimuli responsiveness simultaneously has been difficult for hydrogels. Many toughening methods that involve addition of secondary networks,[18] crosslinkers[12] or reinforcements[23,24] are incompatible for building tough and stimuli-responsive actuators, as the stimuli-responsive network is internally restrained by the non-responsive toughening components. Some water-free polymer systems are easily made to be tough and stimuli responsive, like liquid crystal elastomers (LCEs)[36,37] and poly(pyrrole).[38] These materials consist of tough polymer backbones and stimuli responsive functional groups in a single network. Therefore, it would be advantageous to synthesize hydrogels with an intrinsically tough and stimuli responsive network to realize simultaneous high toughness and stimuli-responsiveness.

3.2. Proposed Methods

Herein, we present a tough and responsive hydrogel synthesized by grafting stimuli-responsive monomers to polymers with high toughness. Poly(vinyl alcohol) (PVA) is a high molecular-weight polymer with excellent mechanical properties due to its high fracture toughness compared to the short chain counterparts.[39] PVA also has a good ability to form nano-crystalline domains for further strengthening and toughening the network via post treatments.[40,41] Therefore, we used PVA and its methacrylate derivatives (PVA-MA) as the tough polymer backbone. The modification from PVA to PVA-MA enabled the photo polymerization of this tough polymer. In this study, N-isopropylacrylamide (NIPAM) was used as an exemplary responsive monomer for grafting onto the PVA-MA backbone to give PVA thermo-responsiveness and PVA/(PVA-MA)-g-PNIPAM hydrogel was fabricated via digital light processing (DLP) based 4D printing.[42] A facile salting out treatment was used subsequently to induce the formation of PVA nano-crystalline domains to further strengthen the hydrogel network. The printed hydrogels showed exceptionally high strength, high toughness, good thermo-responsiveness, and improved actuation force, and they are highly tunable owing to the ability to spatially program the material properties by 4D printing. The presented tough and responsive hydrogel system, with its simple synthesis and modular design, holds great potential for constructing tough and high-power soft-robots, bio-medical devices, and hydrogel actuators.

3.3 Experimental and Characterization Section

3.3.1 Materials

Poly(vinyl alcohol) (PVA, 99% hydrolyzed, M.W 89,000 - 98,000), N-isopropylacrylamide (NIPAM, 99%), Methacrylic acid (MA, 99%), N,N'-Methylenebisacrylamide (Bis), tartrazine, hydroquinone and 2-Hydroxy-4′-(2-hydroxyethoxy)-2-methylpropiophenone (Irgacure 2959) were purchased from Sigma Aldrich. Lithium phenyl-2,4,6-trimethylbenzoylphosphinate (TPO-Li) was purchased from CPS Polymers. Hexane, hydrochloric acid, acetone and triethyl amine was purchased from Fisher Scientifics. NIPAM was purified by recrystallization in hexane. All other chemicals were used without further treatment.

3.3.2 Synthesis of PVA-MA

The PVA-MA was synthesized by a condensation reaction between PVA and MA as shown in **Figure 3.1**. Typically, 20 g of PVA was dissolved in 180 mL of DI water conical flask with heating. 40 mg of hydroquinone was added to the solution. After cooling down, 5 mL MA and 10 mL hydrochloric acid was added to the solution. The mixture was stirred at 300 rpm and 60 ˚C for 12 h. After cooling down, 15 mL triethyl amine was added to the solution. The whole solution was then diluted 10 times and precipitated in acetone. The precipitate was finally filtered and dried in vacuum.

3.3.3 Preparation of Printing Precursor

The printing precursor consists of (10-*x*) wt% PVA, *x* wt% PVA-MA, 20 wt% NIPAM

and 0.1 wt% TPO-Li dissolved in water. The hydrogels were denoted as "*x*P-MA_(10-*x*)P" for *x* wt% of PVA-MA added into the precursor. For controlling light penetration depth, 0.2 wt% tartrazine as photo-absorber was added to the precursor. The ratio of PVA and PVA-MA was adjusted between 0:10 to 7:3 for achieving different properties.

3.3.4 Printer Setup

The home-made printer consists of an DLP-based PRO4500 UV light (385 nm) projector from Wintech Digital System Technology Corporation, a motorized translation stage mounted to a motor controller, and other optical accessories from Thorlabs, Inc. The power density of the projected UV light on the focal plane is measured to be 2.34 mW/cm^2 using an ultraviolet light meter, Traceable Products. A customized program was used to coordinate the projection of image and the movement of the stage. The resolution of the printer was 30 μm in the x–y plane and 10 μm in the z-axis direction.

3.3.5 Printing Process

All the printing proceeded in air under ambient conditions. A 3D computer aided design (CAD) models was first designed and sliced into series of 2D patterns. The patterns were sequentially projected onto the substrate, which was immersed in the precursor solution. The thickness of each layer was set to be 0.1 mm. Each layer was cured for 30 s. For printing the bilayer structures, a bottom layer was printed, rinsed with DI water to remove the unreacted precursor and dried. Then the printed layer was immersed in a

second precursor and a layer with different material was printed on the top. All the samples tested for following measurements of mechanical properties, contraction force, and swelling ratio were all printed by this process.

3.3.6 Salting-out Treatment

The printed hydrogels were first immersed in DI water for 24 hours to remove the excess monomers and then immersed in 0.1-1 M Na_2SO_4 solution for 5 hours to induce aggregation and crystallization of the PVA and PVA-MA chains.

3.3.7 Mechanical Properties Measurement

A Cellscale Univert mechanical tester was used for measuring passive mechanical properties and active contraction of the hydrogel. For passive tensile tests, dog bone specimens with 2 mm gauge width, 4mm gauge length and 2 mm thickness was 3D printed and measured using a 4.5 N loading cell under stretch rate of 0.1 /s. For passive compression tests, cylindrical specimen with 5mm diameter and 2mm height was 3D printed and measured using a 10 N loading cell under compression rate of 0.01/s.

3.3.8 Contraction Force Measurement

For active contraction force measurement, the dog bone specimen was clamped at fixed distance of 4mm using the tensile testing setup with water bath compartment installed, hot water was poured into the bath container and the contraction force was recorded using a 0.5 N loading cell.

3.3.9 Swelling Ratio Measurement

The cylindrical specimen for compression test was equilibrated in water and heated to 40 °C using a hot plate. The area change of the specimen was recorded using a camera from top. It is assumed that the specimen showed uniform volume change in all directions. The volumetric swelling ratio was calculated using the following:

$$Contraction\ ratio = \left(\frac{Area_{40℃}}{Area_{25℃}}\right)^{3/2}$$

3.3.10 Microstructure Characterization

All hydrogel samples were immersed in DI water for 24 hours before freeze-drying using a Labconco FreeZone freeze dryer. The freeze-dried hydrogels were cut to expose the inside and sputtered with gold before carrying out imaging using a ZEISS Supra 40VP SEM.

3.3.11 XRD Characterization

The hydrogel sample was cut into a rectangular shape with dimensions of 2 cm x 1 cm x 4 mm and placed in rectangular sample holders for examination, and the resulting spectrum were analyzed by built-in database on Panalytical X'Pert Pro Powder X-ray Diffractometer.

3.3.12 DSC characterization

Before freeze-drying the hydrogels for Differential Scanning Calorimetry (DSC) measurements, we first used excess chemical cross-links induced by glutaraldehyde to

fix the amorphous PVA polymer chains to minimize the further formation of crystalline domains during the air-drying process following reference[40] . The water content of the hydrogel f_{water} could be obtained by comparing the weight before and after freeze-drying. In a typical DSC measurement, we first weighed the total mass of the freeze-dried sample m. The sample was thereafter placed in a Tzero pan and heated up from 50 °C to 250 °C at the rate of 20 °C/min under a nitrogen atmosphere with flow rate of 30 mL/min. The curve of heat flow shows another narrow peak ranging from 200 °C to 250 °C, which correspond to the melting of the crystalline domains. The integration of the endothermic transition ranging from 200 °C to 250 °C gives the enthalpy for melting the crystalline domains per unit mass of the dry. Therefore, the mass of the crystalline domains $m_{crystalline}$ can be calculated as $m_{crystalline} = m*H_{crystalline}/H^0_{crystalline}$, where $H^0_{crystalline}$ = 138.6 J/g is the enthalpy of fusion of 100 wt.% crystalline PVA measured at the equilibrium melting point T^0_m [43]. Therefore, the crystallinity in the dry sample X_{dry} can be calculated as $X_{dry} = m_{crystalline}/m$. With measured water content from freeze drying, the crystallinity in the swollen state can be calculated as $X_{swollen} = X_{dry} * (1-f_{water})$.

3.3.13 FT-IR Characterization

The Fourier-transform infrared spectroscopy (FT-IR) analysis was conducted using JASCO Model 420 FT-IR using a potassium bromide (KBr) pellet. FT-IR spectra were recorded in the spectral range of 4000–400 cm^{-1} with a 2 cm^{-1} resolution and 32 scans.

3.4 Result and Discussion

3.4.1 Material Design

Figure 3.2a,b showed the one-pot synthesis of the PVA/(PVA-MA)-g-PNIPAM hydrogel. PVA and PVA-MA were used as the tough polymer backbone for two reasons. First, due to the high molecular weight of PVA, the fracture energy of PVA chains is much higher than the relatively short polymer chains formed via radical polymerization from monomers. The energy required to fracture a polymer chain (Γ) scales proportionally with the polymer chains length (n repeating units) according to Lake-Thomas theory ($\Gamma \propto \sqrt{n}$).[39] Second, PVA is easy to crystallize via thermal annealing or phase separation processes.[40,41,44] The crystalline domains can toughen hydrogels by inhibiting crack propagation, crosslinking multiple chains and increase the fracture energy of polymer chains, as the energy required to fracture crystalized chains are much higher than that of its amorphous counterpart. For subsequent grafting of thermally responsive monomers onto the PVA chains, the PVA polymers went through a simple condensation reaction with methacrylic acid (MA) in an acidic environment and produced a UV crosslink-able derivative PVA polymer with the hydroxyl (-OH) side groups partially modified with the methacrylate (-MA) side groups, termed as PVA-MA (**Figure 3.1**a). However, note that PVA-MA has reduced ability to crystalize due to the steric hindrance by the modified side group. Therefore, non-modified pristine PVA was blended with PVA-MA in the precursor for retaining good crystallization ability for toughening the hydrogel. Additionally, PVA-MA is crucial for the grating of NIPAM molecules onto the PVA network, which in turn gave rise to the thermal

responsiveness of the hydrogel. Therefore, a balanced concentration of PVA and PVA-MA should be used for optimum combined mechanical properties and thermal responsiveness. The hydrogels were denoted as "*x*P-MA_(10-*x*)P" for *x* wt% of PVA-MA added in the total precursor, and we mainly used 5P-MA_5P hydrogel in our study due to its combined high strength, high stretchability and good thermal responsiveness. Additionally, water was used as the solvent instead of organic solvents for green synthesis, and TPO-Li was used as the photo-initiator in the aqueous precursor, due to its ability to induce radical polymerization under both visible and UV spectra to fit different printing systems. PVA, PVA-MA, NIPAM and TPO-Li were dissolved in water (**Figure 3.2**a) and exposed to UV light for gelation (**Figure 3.2**b). No crosslinker was added to ensure that all retained NIPAM molecules were attached to the PVA-MA backbone after rinsing. The fabricated hydrogel was transparent and colored with the photo absorber dye added to the precursor (**Figure 3.2**b, bottom image). The chemical composition of the obtained hydrogel was verified with FT-IR analysis (**Figure 3.1**b): 3420 cm^{-1} (N-H in NIPAM groups), 3300 cm^{-1} (broad peak indicating the O–H in PVA), 2940 cm^{-1} (C–H in PVA), 2900 cm^{-1} (C-CH_2 in methacrylate groups), 2862 cm^{-1} (C-CH_3 in methacrylate and NIPAM groups), 1650 cm^{-1} (C=O in NIPAM groups), 1585 cm^{-1} (C=C in methacrylate groups), 1444 cm^{-1} (C-H in methacrylate and NIPAM groups), 1192 cm^{-1} (C-O-C between PVA and methacrylate groups), 1087 cm^{-1} (C-O-H in PVA). When comparing PVA (red) and PVA-MA (blue), we could see the peaks at 1192 cm^{-1} and 1585 cm^{-1} which corresponds to the formation of ester bond and the grafted MA containing C=C bond.

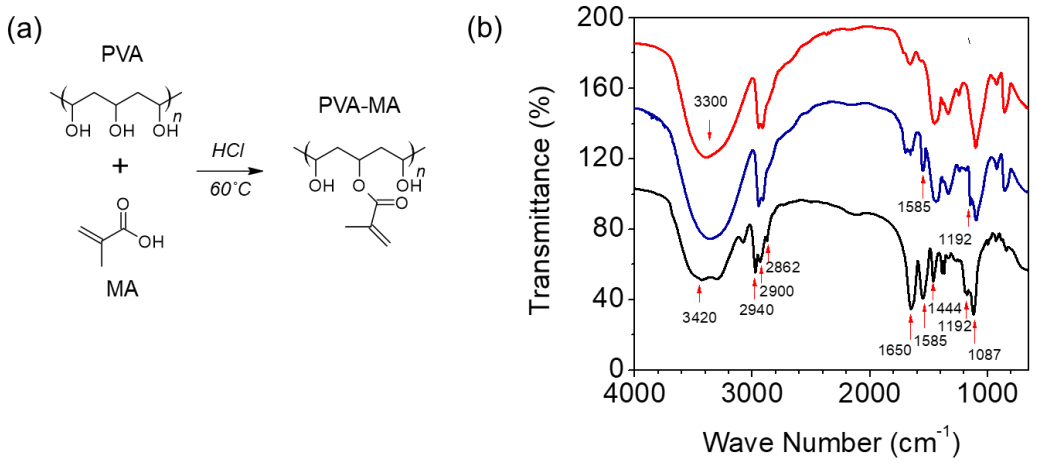

Figure 3.1 (a) Synthesis route of PVA-MA from poly(vinyl alcohol) (PVA) and methacrylic acid (MA). (b) FTIR spectrum of the pristine PVA (red), PVA-MA (blue) and PVA/(PVA-MA)-g-PNIPAM hydrogel (black).

To further toughen the PVA/(PVA-MA)-g-PNIPAM hydrogel, the 3D printed sample was then immersed into Na_2SO_4 salt solutions of various concentrations to induce aggregation and crystallization of the PVA chains. The treatment is known as salting out and is based on the classical Hofmeister effect, in which different ions has distinguishable ability to induced phase separation of solutes and precipitate the dissolved polymers.[45] The sulfate ions have strong ability to induce aggregation and crystallization of the PVA and were used as the salting out agent in this study.[20,44,46] The sample transitioned from transparent to semi-transparent after the salting out treatment, and remained semi-transparent even when immersed back into water, indicating the formation of nano-crystalline domains that strongly scattered light (**Figure 3.2**c), which was also validated by the XRD pattern of the sample (**Figure 3.3**).

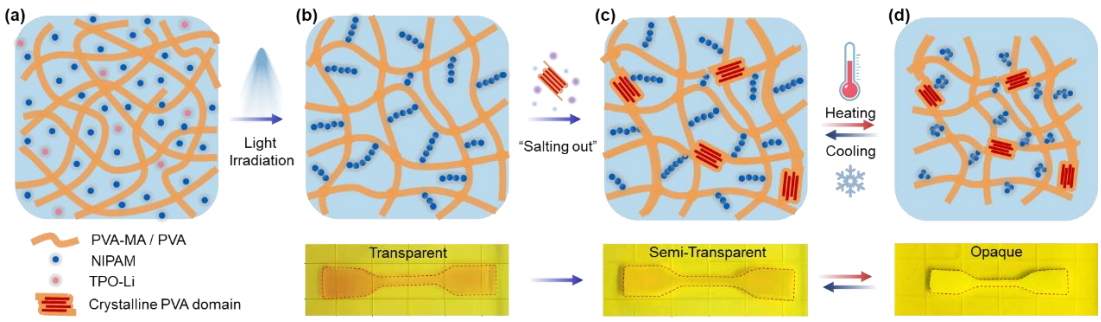

Figure 3.2 Illustration of the synthesis of PVA/(PVA-MA)-g-PNIPAM hydrogel. (a) Aqueous precursor containing PVA, PVA-MA, NIPAM and TPO-Li. (b) The one-pot synthesis of PVA/(PVA-MA)-g-PNIPAM hydrogel by light irradiation from a DLP 3D printer. The as-printed hydrogel was transparent. (c) Toughening of hydrogel by immersion in Na_2SO_4 salt solution to induce PVA aggregation and crystallization. The hydrogel turned semi-transparent after the salting-out process. (d) Actuation of the hydrogel by heating, and the recovery of hydrogel by cooling. The hydrogel turned completely opaque after heating and reverted to semi-transparent after cooling.

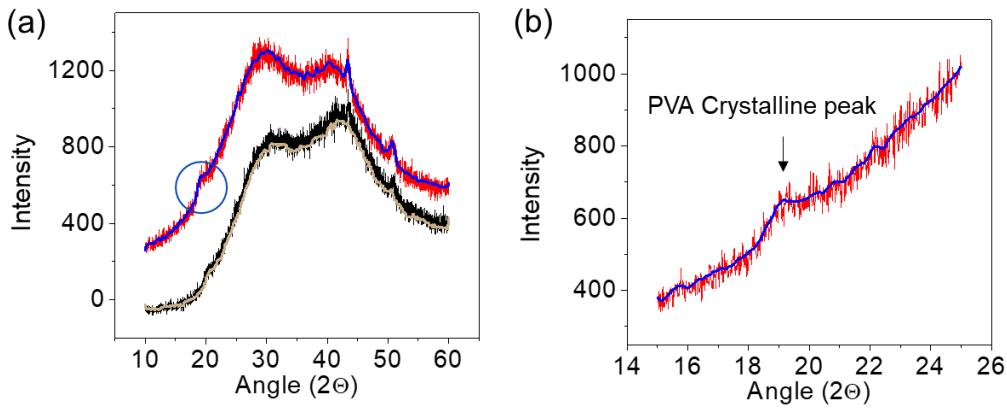

Figure 3.3 XRD pattern of PVA/(PVA-MA)-g-PNIPAM hydrogel before (black) and after (red) toughening by salting out treatment.

The toughened PVA/(PVA-MA)-g-PNIPAM hydrogel by salting out maintained the reversible thermal responsiveness in water (**Figure 3.2**c,d), benefiting from the single network design. The thermal responsive side groups / side chains were combined with the tough hydrogel network, which reduced the internal constraint between the thermal responsive and non-thermal responsive domains in the hydrogel network. When heated above the LCST of PNIPAM, the hydrogel quickly turned opaque as the grafted NIPAM chains phase separated from water and formed globules that additionally scattered light. The volume change was slower than the color change due to the hydrogel's bulk size, and the hydrogel gradually shrunk in size overtime. This could be caused by the relatively small pore size (0.2 – 2 μm) and bulk sample size of the hydrogel, which hindered the diffusion of water in / out of the hydrogel network (**Figure 3.4**). When lowering the bath temperature to below LCST, the hydrogel could recover to the original size and color. Owing to the 3D printability of the hydrogel, large voids serving as efficient water channels could be printed in the hydrogel structure for bypassing the size dependent volume change of the hydrogel and increase actuation speed.

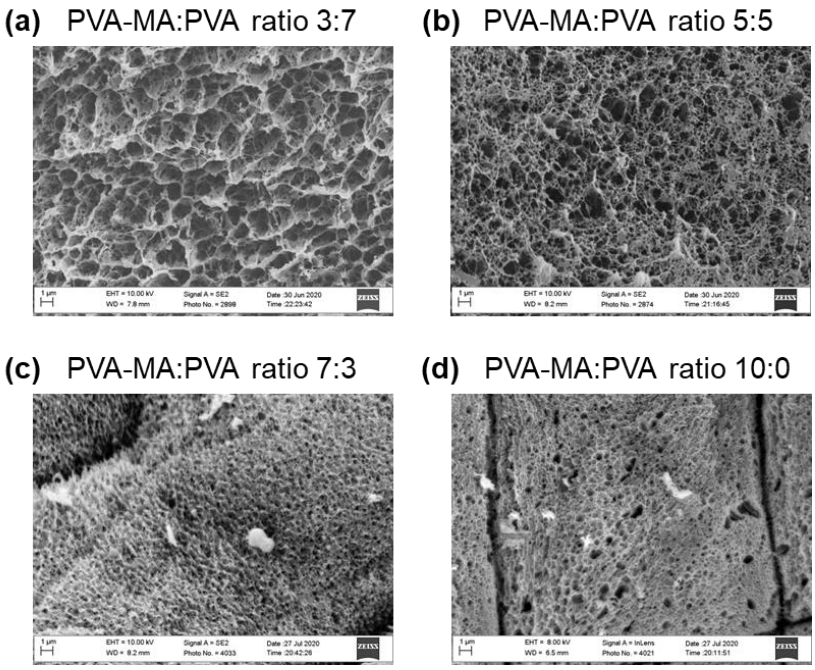

Figure 3.4 Microstructure of the PVA/(PVA-MA)-g-PNIPAM hydrogels with different PVA to PVA-MA ratios. The hydrogels were toughened in 0.5 M Na_2SO_4 solution, washed and then freeze -dried. The pore size decreased with increasing PVA-MA content.

3.4.2 Passive Mechanical Properties

The typical tensile and compressive stress-strain curves of the printed PVA/(PVA-MA)-g-PNIPAM hydrogel with respect to concentration of Na_2SO_4 solution are shown in **Figure 3.5**a,b. All hydrogels were rinsed in DI water to remove the salt prior to mechanical testing. The maximum stress and strain of the hydrogel increased with the concentration of Na_2SO_4 used for salting out, mainly due to the increasing aggregation and crystallinity of the hydrogel with increasing concentration of salting out agent. The typical 5P-MA_5P hydrogel reached ~15% crystallinity against the total solid content corresponding to ~1.5% crystallinity in the wet state after salting out for 5 hours. The

PVA crystalline domains significantly strengthened the hydrogel by their ability to pin down cracks,[41] they also improved hydrogel's elasticity by acting as rigid high functionality crosslinkers.[13]

For a typical 5P-MA_5P hydrogel, the tensile strength increased from 0.015 MPa to 2.2 MPa (**Figure 3.5**a), and the compressive strength increased from 0.16 MPa to 3.8 MPa (**Figure 3.5**b) after the salting-out treatment in 1M Na_2SO_4 solution. The corresponding toughness of the 5P-MA_5P hydrogel reached 10 MJ/m^3 (**Figure 3.5**c), comparable to that of natural tendons. Compared with other double-network tough NIPAM hydrogels,[30,47–49] the PVA/(PVA-MA)-g-PNIPAM hydrogel showed high stretchability, strength and toughness (**Figure 3.5**d).

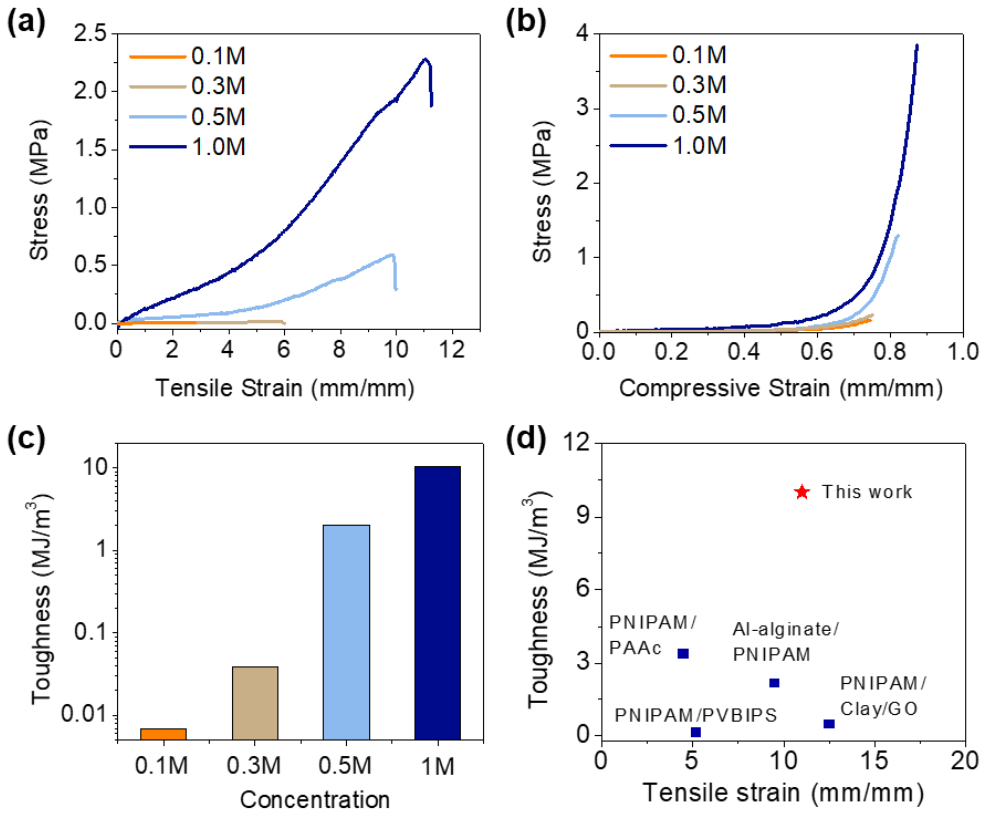

Figure 3.5 Mechanical properties of PVA/(PVA-MA)-g-PNIPAM hydrogels. (a & b) The tensile and compressive stress-strain curves of 5P-MA_5P hydrogel toughened in

different concentrations of Na_2SO_4 salt solution. (c) The tensile toughness of 5P-MA_5P hydrogels that were toughened in different concentrations of Na_2SO_4 salt solutions. (d) Ashby diagram showing the toughness vs. strain properties of 5P-MA_5P hydrogel compared with other tough NIPAM hydrogel systems.

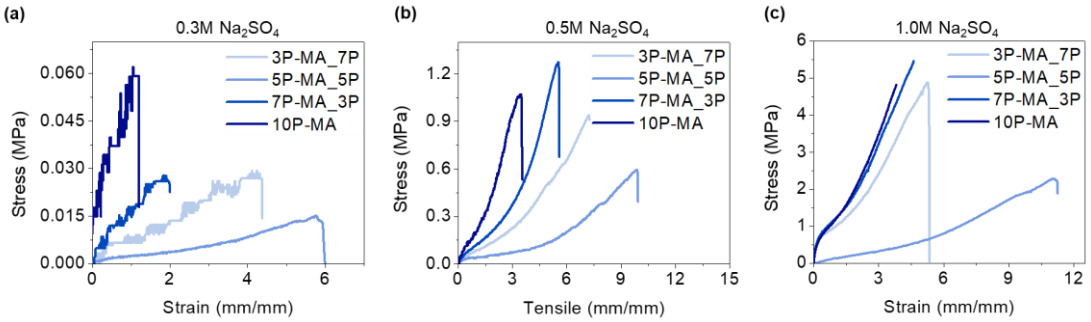

Figure 3.6 Stress-strain curves of PVA/(PVA-MA)-g-PNIPAM hydrogels with different PVA-to-PVA-MA ratios and toughened in different concentrations of Na_2SO_4 solutions. The 5P-MA_5P hydrogel toughened in 0.5 M Na_2SO_4 presented the optimum overall mechanical and responsive performance.

3.4.3 Active Actuation Properties

The PVA/(PVA-MA)-g-PNIPAM hydrogel maintained thermal responsiveness after the toughening process by salting out (**Figure 3.7**a), benefiting from the combination of thermal responsive side groups and tough polymer main chains in a single network. For a typical 5P-MA_5P hydrogel, the volumetric contraction could reach 50% for hydrogels toughened in 0.1M Na_2SO_4, comparable to the pure PNIPAM hydrogel (60% contraction). Although, the volumetric contraction decreased with increasing salt concentration, which was due to the reduced polymer chain mobility as the PVA and

(PVA-MA)-g-PNIPAM polymer chains aggregated and crystalized during the salting out process, the ultra-tough 5P-MA_5P hydrogel toughened in 1M Na_2SO_4 still maintained around 10% volumetric contraction (**Figure 3.7**b). The PVA/PVA-MA ratio also showed effect on the swelling ratio (**Figure 3.7**c). The contraction of the PVA/(PVA-MA)-g-PNIPAM hydrogel increased with the PVA-MA concentration. On one hand, higher PVA content increased the aggregates and crystalline domains formed during salting out for better toughening of the hydrogel (**Figure 3.6**) but provided fewer grafting sites for increasing thermal responsiveness of the hydrogel network. On the other hand, higher PVA-MA increased the amount of NIPAM grafted to the hydrogel network, which in turn improved the thermal responsiveness of the hydrogel but would lead to higher modulus. According to "Flory rubber elastic theory", during elastic deformation of polymers, the crosslinking density is proportionally correlated with the elastic modulus of the polymer.[50,51] (**Figure 3.8**). Therefore, higher PVA-MA would lead to higher crosslinking density, as well as reduce the maximum strain of the hydrogel (**Figure 3.6**).

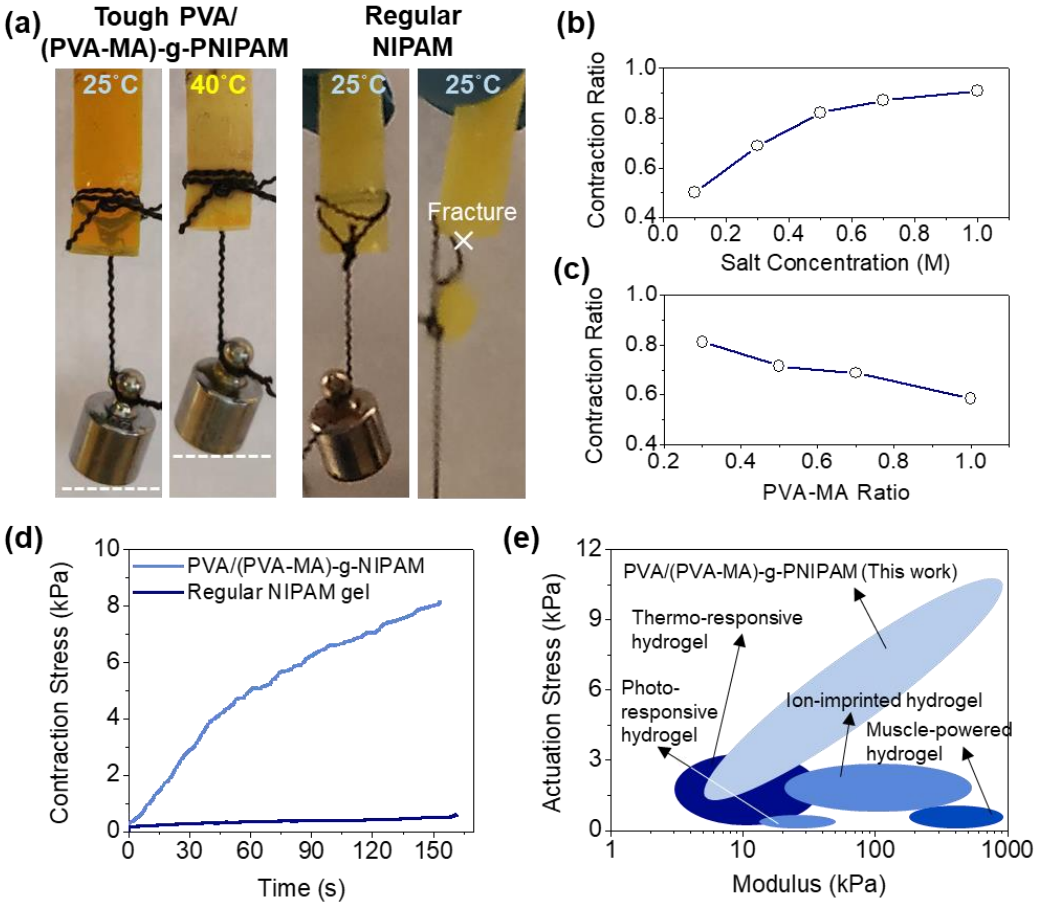

Figure 3.7 Actuation and output stress of PVA/(PVA-MA)-g-PNIPAM hydrogel. (a) Application of PVA/(PVA-MA)-g-PNIPAM hydrogel as linear actuator compared with NIPAM hydrogel. The 5P-MA_5P hydrogel toughened in 0.5 M Na_2SO_4 solution could lift a 20 g weight without fracture while regular NIPAM hydrogel of the same dimension fractured easily. (b) Contraction ratio of the 5P-MA_5P hydrogel toughened in different concentrations of Na_2SO_4 solution. (c) Contraction ratio of PVA/(PVA-MA)-g-PNIPAM hydrogel with different PVA to PVA-MA ratio toughened in 0.3 M Na_2SO_4 solution. (d) The stress – time curve of 5P-MA_5P hydrogel toughened in 0.5 M Na_2SO_4 solution compared with regular PNIPAM hydrogel. (e) Ashby diagram

showing the actuation stress vs. modulus of the PVA/(PVA-MA)-g-PNIPAM hydrogel compared with other hydrogel actuators.

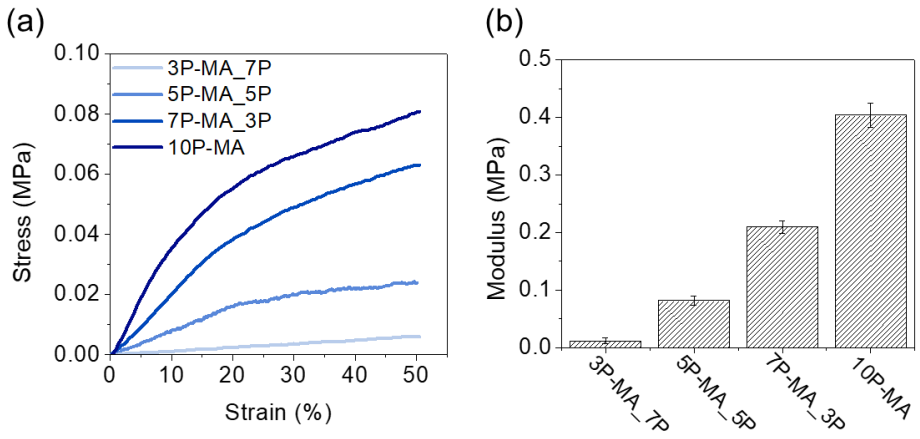

Figure 3.8 (a) Stress-strain curves of the as-printed hydrogels with various PVA / PVA-MA ratios in the strain range of 0-50%. (b) Corresponding modulus extrapolated from the linear regions of the stress-strain curves in a.

With the combined high toughness and thermal responsiveness, a typical 5P-MA_5P hydrogel strip fabricated via 4D printing and subsequently toughened in 0.5 M Na_2SO_4 could lift heavy weights (20 g) without large passive deformation or fracture (**Figure 3.7**a, left). In contrast, conventional NIPAM hydrogel (fabricated by polymerizing 30 wt% NIPAM, 1.5 wt% Bis and 1 wt% Irgacure 2959 in DMSO and immersed back into DI water) with the same dimension deformed severely under the same weight, which lead to formation and propagation of cracks in the hydrogel and eventually fracture of the hydrogel (**Figure 3.7**a, right). We quantitatively measured the contraction force delivered by the two hydrogels, and the tough 5P-MA_5P hydrogel showed ~20 times higher contraction force than the conventional NIPAM hydrogel (**Figure 3.7**d).

Compared to various state-of-the-art hydrogel actuators,[52–56] the tough PVA/(PVA-MA)-g-PNIPAM hydrogel showed a relatively high actuation force and modulus (**Figure 3.7**e).

The deliverable force of the PVA/(PVA-MA)-g-PNIPAM hydrogel is positively related with the mechanical properties of the hydrogel (**Figure 3.7**e). Without toughening by salting out, the contraction force of the PVA/(PVA-MA)-g-PNIPAM hydrogel is comparable to that of the conventional NIPAM hydrogel. With increasing toughness of the PVA/(PVA-MA)-g-PNIPAM hydrogel by using higher concentration salt solution, the contraction force also increased. The reason for this relationship is as follows: The non-toughened PVA/(PVA-MA)-g-PNIPAM is intrinsically soft, which would deform severely under low stress. While the hydrogel could contract significantly upon heating when there is no external load, the displacement is reduced when external load exists due to the passive extension of the hydrogel under stress. Thus, the tension between hydrogel and object is relaxed due to this passive deformation which reduced the force being delivered externally (**Figure 3.9**a). Additionally, in the case of high external loading, the hydrogel would immediately fracture due to its low strength and toughness. On the contrary, the toughened PVA/(PVA-MA)-g-PNIPAM hydrogel has a much higher modulus and would show reduced passive deformation under external loading. The toughened hydrogel could also endure much higher external force. Thus, the tension between toughened hydrogel and external object maintained at a much higher value as the toughened hydrogel contracted without large passive extension under the tension, which led to the increased deliverable force (**Figure 3.9**b).

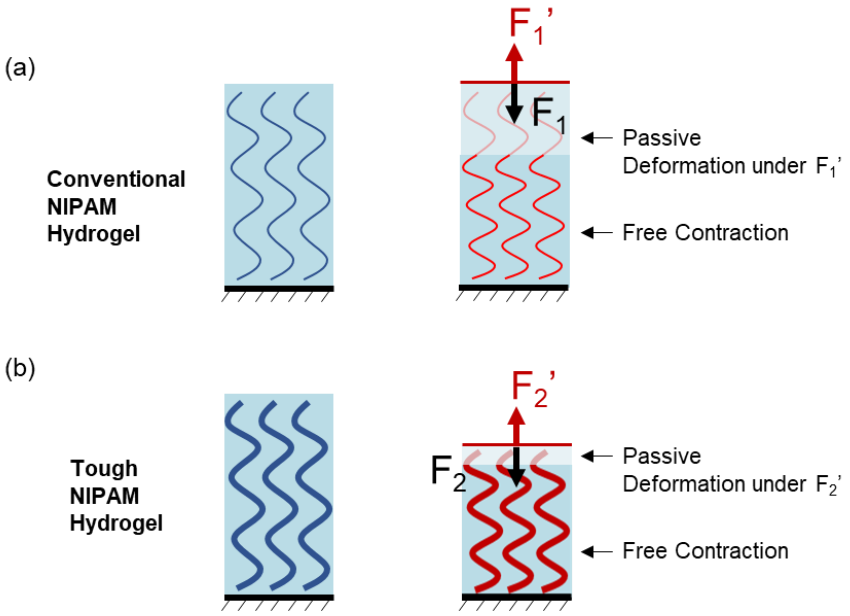

Figure 3.9 Illustration of contraction under constraint of a conventional PNIPAM hydrogel (a) compared with tough PVA/(PVA-MA)-g-PNIPAM hydrogel (b).

3.4.4 Thermal/photo actuators with high force and fast actuation

With high toughness and actuation force, the PVA/(PVA-MA)-g-PNIPAM hydrogels could readily be applied to fabricate hydrogel actuators. By 4D printing, bilayer actuators of various geometry could be facilely fabricated. The bilayer actuators consist of a passive layer of PVA/PVA-MA hydrogel and an active layer of PVA/(PVA-MA)-g-PNIPAM hydrogel. The printed bilayer actuators were washed in DI water and immersed in 0.5M Na_2SO_4 salt for toughening. After toughening, the bilayer actuators were immersed back in water for actuation tests. **Figure 3.10**a showed the actuation of a bilayer beam by heating. The bilayer beam was initially bent toward the passive layer, due to the higher shrinkage of PVA/PVA-MA hydrogel compared to PVA/(PVA-MA)-g-PNIPAM hydrogel. Upon heating, the bilayer beam quickly bent toward the active

layer. Despite the initial reverse bending, the bilayer beam completely bent toward the passive layer within 150 seconds and showed a large bending angle of ~210° at the tip. **Figure 3.10**b showed the actuation of a bilayer flower by cooling. The flower pedals were initially bent by heating. When immersed in room temperature water bath, the active layer gradually expanded which led to the blooming of the bilayer flower. By spatially programming the area ratio of the passive / active layer, the flower pedals after blooming did not overbend toward the passive layer. Combining high strength, high toughness, high actuation force and 4D printing aided design, a thermally activated bilayer tough hydrogel gripper was demonstrated in **Figure 3.10**c. Upon heating, the gripper arm bent toward the object and locked onto the object, which enabled the subsequent lifting of the object out of the water bath. In contrast, while a conventional NIPAM hydrogel gripper of the same geometry showed good actuation performance, it deformed severely during the lifting process and failed to lift the same object. Note that the arms of the PVA/(PVA-MA)-g-PNIPAM hydrogel gripper did not show large deformation during the lifting process, owing to the high strength and contraction force of the hydrogel. The weight being lifted weighed 1g, which is approximately 5 times the weight of the solid content of the hydrogel gripper.

Remote activatability is a significant advantage of NIPAM-based hydrogels due to the facile conversion of photons to thermal energy through various photo-absorbers.[4,6] The photo-absorbers are generally black materials with nanometer sizes for maximum photo-thermal conversion efficiency, here we utilized poly(pyrrole) as the photo-absorber coating. As shown in **Figure 3.10**d,e, the bilayer hydrogel actuator turned

black after coating with poly(pyrrole) and gained remote activatability using an IR laser (50 mW). The illuminated part on the hydrogel actuators were locally heated quickly to induce bending, while the unilluminated parts remained cool and static. By controlling the illumination, good spatial control of actuation could be realized in the hydrogel actuator (**Figure 3.10**e).

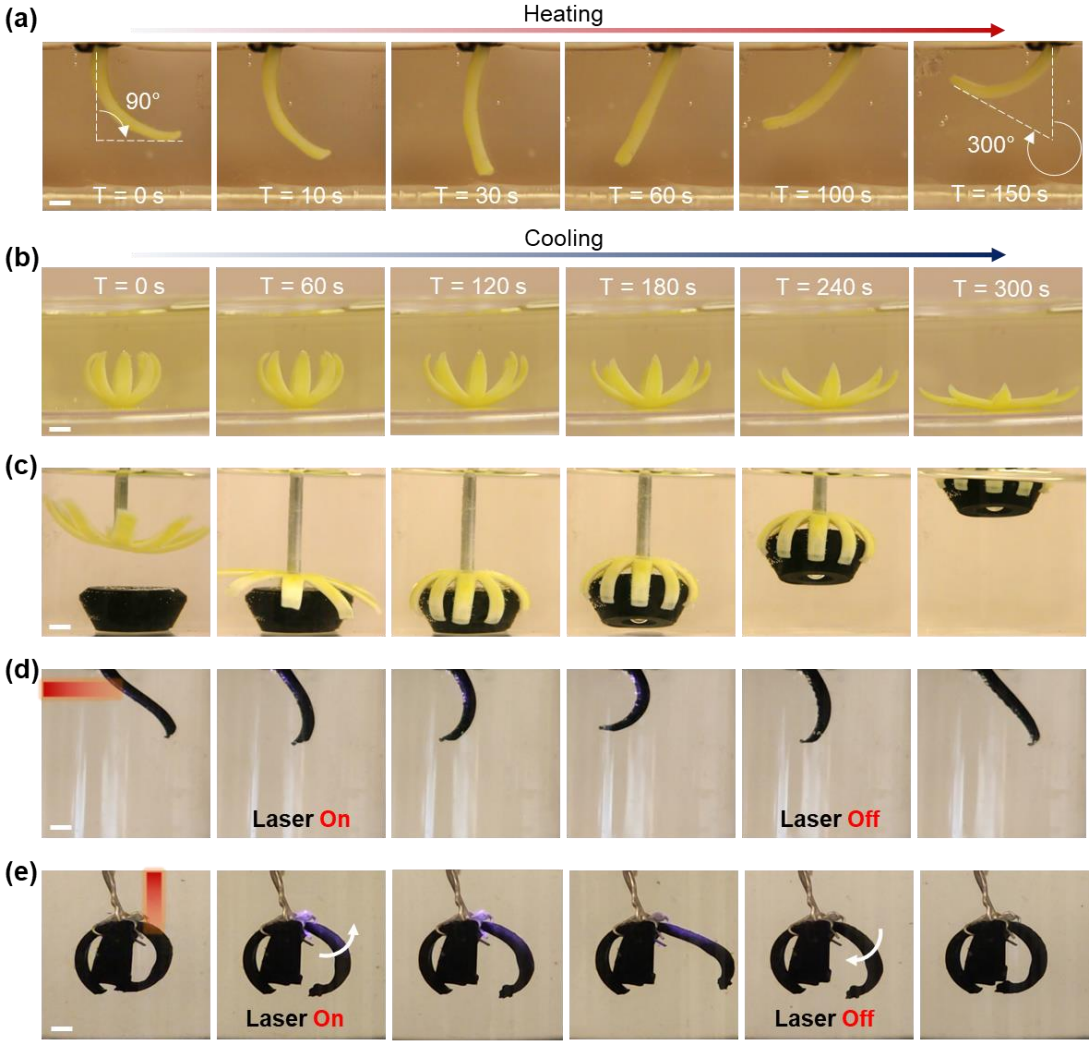

Figure 3.10 Customized actuator geometry and actuation speed. (a) A printed bilayer beam actuator showing fast bending and large bending angle under heating. (b) A bilayer flower blooms under cooling. (c) 3D printed bilayer gripper picking up an object through thermal actuation. The object weighs 1g. (d) Remote actuation of bilayer beam

actuator coated with a thin layer of poly(pyrrole). (e) Remote and selective actuation of bilayer gripper actuator coated with a thin layer of poly(pyrrole). Scale bar is 1 mm.

Actuation speed is another important criterion of hydrogel actuator. Due to the diffusion-mediated swelling and contraction of hydrogels, the actuation speed inversely scales with the actuator size. Utilizing the ability to spatially program the hydrogel, the size-dependent actuation speed of PVA/(PVA-MA)-g-PNIPAM hydrogels could be bypassed by printing large voids into the hydrogel to facilitate the fast diffusion of water in and out of the hydrogel. **Figure 3.11**a showed three types of printed 5P-MA_5P hydrogel lattice, respectively with Kelvin cell, Simple Cubic and Octet truss unit cells. These hydrogel lattices were originally weak and collapsed in air in the as-printed state (**Figure 3.12**a); after toughening in 0.5 M Na_2SO_4, they became capable of self-supporting their own weight and retaining the designed structure in air as a stand-alone architecture (**Figure 3.12**b). When using the lattice design with octet truss cells, the lattice could tolerate high external loading and deformation and still recover (**Figure 3.11**b). Applying the lattice design in printing hydrogel structures, the latticed 5P-MA_5P hydrogel toughened in 0.5 M Na_2SO_4 showed 4 times faster contraction speed compared to a non-structured bulk PVA/(PVA-MA)-g-PNIPAM hydrogel (**Figure 3.11**c,d). The latticed hydrogel also showed increased contraction ratio compared to its non-structured counterpart. Therefore, with structural design and the aid of 4D printing, fast actuation speed could be achieved in addition to the previously demonstrated high toughness and contraction force.

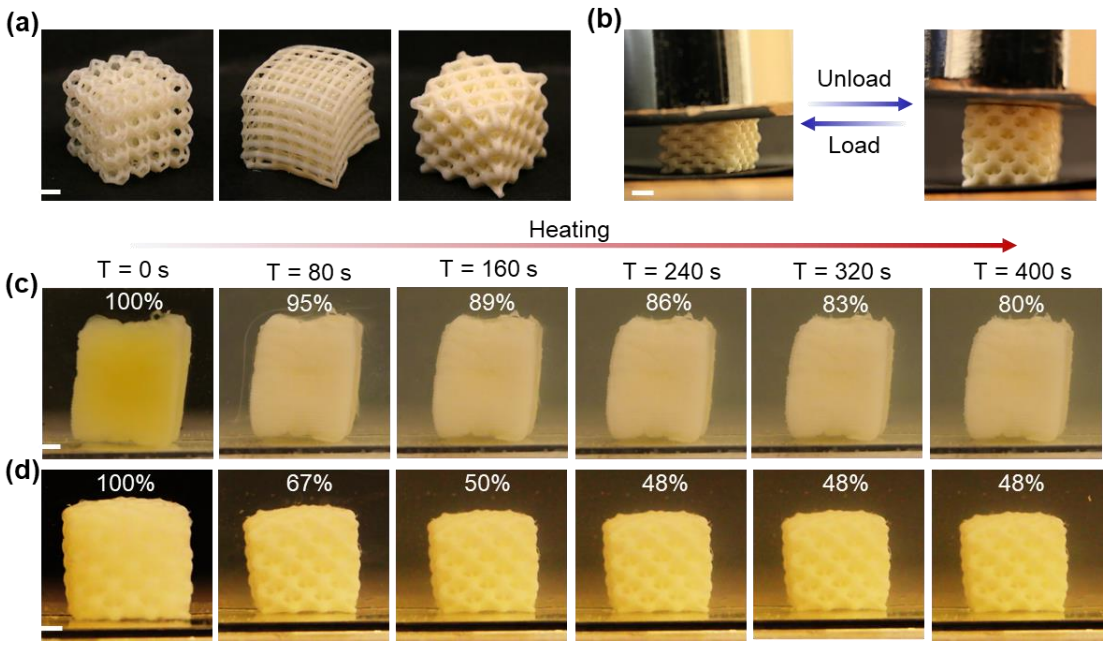

Figure 3.11 (a & b) Lattice structured 5P-MA_5P hydrogels toughened in 0.5 M Na_2SO_4 showing self-support in air and recoverability after deformed. (c & d) Boosting the actuation speed and contraction ratio by printing lattice structured hydrogel in comparison with a bulk hydrogel of the same bulk volume. Scale bar is 2 mm.

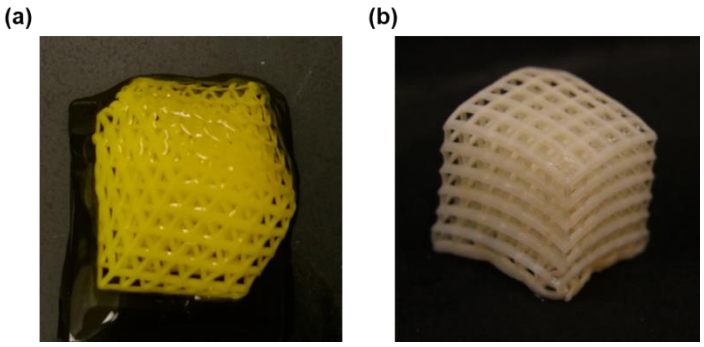

Figure 3.12 Printed simple cubic lattice of PVA/(PVA-MA)-g-PNIPAM hydrogel before (a) and after (b) the toughening treatment by salting-out. These lattices were originally weak and collapsed in air in the as printed state (a) but became capable of self-supporting their own weight and retain the designed structure as a stand-alone architecture in air after toughening in 0.5 M Na_2SO_4 (b).

3.5 Conclusion

In summary, we have demonstrated a material design that consisted of stimuli-responsive monomers and tough polymers in a single hydrogel network for combined high toughness and high actuation performance. Specifically, we showcased this design by grafting thermal responsive NIPAM monomers to tough PVA/PVA-MA hydrogel network in a one pot synthesis. We have evaluated the effect of salt concentration, PVA/PVA-MA ratio and structural design on the mechanical and actuation performance of the PVA/(PVA-MA)-g-PNIPAM hydrogel. Utilizing the combined high toughness and improved actuation force of the PVA/(PVA-MA)-g-PNIPAM hydrogel**s**, bilayer actuators were fabricated via 4D printing for demonstration. Remote actuation using light was also demonstrated using a photo-thermal energy conversion route. Overall, the presented material design significantly improved material toughness while maintaining high swelling/contraction of the hydrogel. We are convinced that the presented design would benefit the fabrication of hydrogel actuators and robotics for practical applications, and would lay the path for new pH responsive, magneto responsive, humidity responsive hydrogel systems with both high toughness and high actuation performances.

3.6 Reference

[1] Ionov, L. *Mater. Today* **2014**, 17 (10), 494–503.

[2] Yuk, H.; Varela, C. E.; Nabzdyk, C. S.; Mao, X.; Padera, R. F.; Roche, E. T.; Zhao, X. *Nature* **2019**,575(7781), 169−174

[3] Liu, X.; Liu, J.; Lin, S.; Zhao, X. *Mater. Today* **2020**, 36, 102–104.

[4] Zhao, Y.; Xuan, C.; Qian, X.; Alsaid, Y.; Hua, M.; Jin, L.; He, X. *Sci. Robot.* **2019**, 4 (33), eaax7112.

[5] Yuk, H.; Lin, S.; Ma, C.; Takaffoli, M.; Fang, N. X.; Zhao, X. *Nat. Commun.* **2017**, 8.

[6] Qian, X.; Zhao, Y.; Alsaid, Y.; Wang, X.; Hua, M.; Galy, T.; Gopalakrishna, H.; Yang, Y.; Cui, J.; Liu, N.; Marszewski, M.; Pilon, L.; Jiang, H.; He, X. *Nat. Nanotechnol.* **2019**, 14 (11), 1048–1055.

[7] Xu, X.; Liu, Y.; Fu, W.; Yao, M.; Ding, Z.; Xuan, J. *Polymers (Basel)*. **2020**, 12 (3, 580), 1–22.

[8] D'Eramo, L.; Chollet, B.; Leman, M.; Martwong, E.; Li, M.;Geisler, H.; Dupire, J.; Kerdraon, M.; Vergne, C.; Monti, F.; Tran, Y.;Tabeling, P. *Microsystems Nanoeng*. **2018**,4(1), 17069.

[9] Tang, L.; Wang, L.; Yang, X.; Feng, Y.; Li, Y.; Feng, W. *Prog. Mater. Sci.***2021**,115, 100702.

[10] Guo, J.; Yang, W.; Deng, Y.; Wang, C.; Fu, S. *Small* **2005**, 1 (7), 737–743.

[11] Hu, X.; Vatankhah-Varnoosfaderani, M.; Zhou, J.; Li, Q.; Sheiko, S. S. *Adv. Mater.* **2015**, 27 (43), 6899–6905.

[12] Sun, J.-Y.; Zhao, X.; Illeperuma, W. R. K.; Chaudhuri, O.; Oh, K. H.; Mooney, D. J.; Vlassak, J. J.; Suo, Z. *Nature* **2012**, 489 (7414), 133–136.

[13] Zhao, X. *Soft Matter* **2014**, 10 (5), 672–687.

[14] Shibayama, M. *Soft Matter* **2012**, 8 (31), 8030–8038.

[15] Haq, M. A.; Su, Y.; Wang, D. Mater. *Sci. Eng. C* **2017**, 70, 842–855.

[16] Illeperuma, W. R. K.; Sun, J. Y.; Suo, Z.; Vlassak, J. J. *Soft Matter* **2013**, 9 (35), 8504–8511.

[17] Depa, K.; Strachota, A.; Šlouf, M.; Hromádková, J. *Eur. Polym. J.* **2012**, 48 (12), 1997–2007.

[18] Gong, J. P.; Katsuyama, Y.; Kurokawa, T.; Osada, Y. *Adv. Mater.* **2003**, 15 (14), 1155–

[19] Lin, P.; Ma, S.; Wang, X.; Zhou, F. *Adv. Mater.* **2015**, 27 (12), 2054–2059.

[20] Yang, Y.; Wang, X.; Yang, F.; Shen, H.; Wu, D. *Adv. Mater.* **2016**, 28 (33), 7178–7184.

[21] Takahashi, R.; Sun, T. L.; Saruwatari, Y.; Kurokawa, T.; King, D. R.; Gong, J. P. *Adv. Mater.* **2018**, 30 (16), 1–7.

[22] Lin, S.; Cao, C.; Wang, Q.; Gonzalez, M.; Dolbow, J. E.; Zhao, X. *Soft Matter* **2014**, 10 (38), 7519–7527.

[23] Huang, Y.; King, D. R.; Sun, T. L.; Nonoyama, T.; Kurokawa, T.; Nakajima, T.; Gong, J. P. *Adv. Funct. Mater.* **2017**, 27 (9), 1–10.

[24] Xiang, C.; Wang, Z.; Yang, C.; Yao, X.; Wang, Y.; Suo, Z. *Mater. Today* **2019**, 34 (September), 7–16.

[25] Illeperuma, W. R. K.; Sun, J. Y.; Suo, Z.; Vlassak, J. J. *Extrem. Mech. Lett.* **2014**, 1, 90–96.

[26] Tian, Y.; Wei, X.; Wang, Z. J.; Pan, P.; Li, F.; Ling, D.; Wu, Z. L.; Zheng, Q. *ACS Appl. Mater. Interfaces* **2017**, 9 (39), 34349–34355.

[27] Zheng, S. Y.; Shen, Y.; Zhu, F.; Yin, J.; Qian, J.; Fu, J.; Wu, Z. L.; Zheng, Q. *Adv. Funct. Mater.* **2018**, 28 (37), 1–8.

[28] Peng, X.; Li, Y.; Zhang, Q.; Shang, C.; Bai, Q. W.; Wang, H. *Adv. Funct. Mater.* **2016**, 26 (25), 4491–4500.

[29] Liu, X.; He, B.; Wang, Z.; Tang, H.; Su, T.; Wang, Q. *Sci. Rep.* **2014**, 4, 1–7.

[30] Xiao, S.; Zhang, M.; He, X.; Huang, L.; Zhang, Y.; Ren, B.; Zhong, M.; Chang, Y.; Yang, J.; Zheng, J. *ACS Appl. Mater. Interfaces* **2018**, 10 (25), 21642–21653.

[31] Baker, A. B.; Wass, D. F.; Trask, R. S. *Sensors Actuators, B Chem.* **2018**, 254, 519–525.

[32] Scherzinger, C.; Schwarz, A.; Bardow, A.; Leonhard, K.; Richtering, W. *Colloid Interface Sci.* **2014**, 19 (2), 84–94.

[33] Zhang, Y.; Furyk, S.; Bergbreiter, D. E.; Cremer, P. S. *J. Am. Chem. Soc.* **2005**, 127 (41), 14505–14510.

[34] Yang, C.; Liu, Z.; Chen, C.; Shi, K.; Zhang, L.; Ju, X. J.; Wang, W.; Xie, R.; Chu, L. Y. *ACS Appl. Mater. Interfaces* **2017**, 9 (18), 15758–15767.

[35] Li, Y.; Sun, Y.; Xiao, Y.; Gao, G.; Liu, S.; Zhang, J.; Fu, J. *ACS Appl. Mater. Interfaces* **2016**, 8 (39), 26326–26331.

[36] Gelebart, A. H.; Vantomme, G.; Meijer, E. W.; Broer, D. J. *Adv. Mater.* **2017**, 29 (18).

[37] Jan Mulder, D.; Selinger, R. L. B.; Konya, A.; Gelebart, A. H.; Varga, M.; Vantomme, G.; Meijer, E. W.; Broer, D. J. *Nature* **2017**, 546 (7660), 632–636.

[38] Ma, M.; Guo, L.; Anderson, D. G.; Langer, R. *Science* **2013**, 339(6116), 186−189.

[39] Lake, G. J.; Thomas, A. G. *Proc. R. Soc. London. Ser. A. Math. Phys. Sci.***1967**,300(1460), 108−119.

[40] Lin, S.; Liu, J.; Liu, X.; Zhao, X. *Proc. Natl. Acad. Sci*. **2019**, 116 (21), 10244–10249.

[41] Lin, S.; Liu, X.; Liu, J.; Yuk, H.; Loh, H.-C.; Parada, G. A.;Settens, C.; Song, J.; Masic, A.; McKinley, G. H.; Zhao, X. *Sci. Adv.***2019**,5(1), eaau8528.

[42] Wu, D.; Song, J.; Zhai, Z.; Hua, M.; Kim, C.; Frenkel, I.; Jiang, H.; He, X. *ACS Appl. Mater. Interfaces* **2019**, 11 (50), 47468–47475.

[43] Peppas, N. A.; Merrill, E. W. *J. Appl. Polym. Sci.* **1976**, 20 (6), 1457–1465.

[44] Bai, R.; Yang, J.; Morelle, X. P.; Suo, Z. *Macromol. Rapid Commun*. **2019**, 40 (8), 1–8.

[45] Kunz, W.; Henle, J.; Ninham, B. W. *Curr. Opin. Colloid Interface Sci.* **2004**, 9 (1–2), 19–37.

[46] He, Q.; Huang, Y.; Wang, S. *Adv. Funct. Mater*. **2018**, 28 (5), 1–10.

[47] Wang, T.; Huang, J.; Yang, Y.; Zhang, E.; Sun, W.; Tong, Z. *ACS Appl. Mater. Interfaces* **2015**, 7 (42), 23423–23430.

[48] Zheng, W. J.; An, N.; Yang, J. H.; Zhou, J.; Chen, Y. M. *ACS Appl. Mater. Interfaces* **2015**, 7 (3), 1758–1764.

[49] Wang, Y. J.; Li, C. Y.; Wang, Z. J.; Zhao, Y.; Chen, L.; Wu, Z. L.; Zheng, Q. J. *Polym. Sci. Part B Polym. Phys.* **2018**, 56 (19), 1281–1286.

[50] Jiang, H.; Su, W.; Mather, P. T.; Bunning, T. J. *Polymer*. **1999**, 40 (16), 4593–4602.

[51] Flory, P. J. *Polym. J.* **1985**, 17 (1), 1–12.

[52] Cvetkovic, C.; Raman, R.; Chan, V.; Williams, B. J.; Tolish, M.; Bajaj, P.; Sakar, M. S.; Asada, H. H.; Saif, M. T. A.; Bashir, R. *Proc. Natl. Acad. Sci. U. S. A.* **2014**, 111 (28), 10125–10130.

[53] Xia, L. W.; Xie, R.; Ju, X. J.; Wang, W.; Chen, Q.; Chu, L. Y. *Nat. Commun*. **2013**, 4, 1–11.

[54] Kim, Y. S.; Liu, M.; Ishida, Y.; Ebina, Y.; Osada, M.; Sasaki, T.; Hikima, T.; Takata, M.; Aida, T. *Nat. Mater.* **2015**, 14 (10), 1002–1007.

[55] Takashima, Y.; Hatanaka, S.; Otsubo, M.; Nakahata, M.; Kakuta, T.; Hashidzume, A.; Yamaguchi, H.; Harada. *Nat. Commun.* **2012**, 3.

[56] Palleau, E.; Morales, D.; Dickey, M. D.; Velev, O. D. *Nat. Commun.* **2013**, 4, 1–7.

Chapter 4. Gold Printing via Anion-Assisted Photochemical Deposition

4.1 Introduction

Advancements in metal patterning technologies have improved the miniaturization, cost-efficiency, productivity, and customization of a variety of applications including integrated circuits, micro-optical components, micro electromechanical systems (MEMS, wearable electronics and biosensing devices.[1–4] Metal patterning is commonly realized through selective etching or "lift-off" technique by conventional photolithography. Such subtractive manufacturing methods, due to their long cycle time, strict operation conditions, and complex procedures, have been phased-out in industrial rapid production and prototyping facilities.[5]

With the rapid advancement of contemporary additive manufacturing techniques, the aforementioned issues have been partially remedied by inkjet printing and direct laser writing (DLW).[6] Inkjet printing has been utilized to readily print silver particle/nanowire composites,[7–11] but it requires careful optimization of the precursor's rheological properties to achieve printability, and then a post-treatment to enhance the necessary conductivity.[12,13] DLW has been used to print silver via a photochemical process, where metal ions are photo-reduced from metallic salt solutions within selective voxels to form metal patterns and structures.[14,15] This emerging technique has substantially extended the resolution in fabrication to micro and sub-micro levels. Delicate 2D or 3D metal, or metal-polymer composite structures with a feature size of 120 nm can be fabricated via multiphoton-induced reactions.[16–18] Nonetheless, DLW suffers from low efficiency when printing millimeter-scale patterns or structures.[19]

Particularly, digital light processing (DLP)-based projection lithography for metal printing has been developed to fill this gap, in which planar patterns are printed in

parallel instead of in series.[20–22] Applying DLP to metal printing can significantly simplify metal patterning processes for either subtractive or additive manufacturing.[23,24] Previously, we reported a room-temperature printing method using visible light. Highly conductive, patterned silver could be produced after a simple chemical annealing process of as-printed patterns.[25] A similar printing process utilizing a blue laser sintering post-treatment was also reported.[26] Functional polymers have been utilized to assist electroless deposition of metal thin films and patterns, and similar strategy was applied to DLP-based metal printing recently.[27] Recently, Zhao *et al.* proposed to use a polymer backbone to guide the growth of metal particles to achieve a dense metallic thin film, which eliminates the need for post-treatment.[28] Despite the progress achieved, issues and challenges such as limited thickness, singularity of structures, short lifetime of inks, and a lack of investigations into electrochemical properties and applications, necessitates additional studies of this metal patterning approach. Furthermore, silver is the focus of most published works, while gold, a noble metal with extraordinary chemical stability, conductivity, optical properties, catalytic capability, and biocompatibility, has not yet been systematically studied in DLP-based metal printing.

4.2 Proposed Method

Thus, we present a simple and novel strategy for one-step annealing-free metal patterning, namely anion-assisted photochemical deposition (APD). APD utilizes specific ion effects with projection lithography to directly print high conductivity (1.08×10^7 S m^{-1}, 24% of the bulk Au conductivity) gold patterns by simply projecting digital images on either rigid or flexible substrates at ambient conditions. Specific ion effect, also known as the Hofmeister effect, describes the changes of protein solubility induced by salts with varied ionic strength. By appropriately increasing the ionic

strength of a solution, the solubility of a protein can be increased – referred to as "salting in – while with a very high ionic strength, a protein solute can be precipitated – referred to as "salting out". In recent decades, this concept has been extended to many other macromolecules and broad researching fields such as hydrogels, nucleation, and self-assembly.[29–31] It has found its way into metallic nanotechnology as well, specifically so in laser synthesis and processing of colloid (LSPC).[32] Moreover, Du *et al.* succeeded in fabricating noble metal aerogels by taking advantage of specific ion effects.[33] In this work, we propose an APD technique which utilizes specific ion effects to assist the direct deposition and growth of gold nanoparticles (AuNPs) networks, and in doing so, APD allows us to achieve tunable porous gold structures. Such controllability over gold's morphologies offers great potential for broader applications where a variance in nano- and/or micro-structure is demanded. In addition, conformable gold electrodes are printed to demonstrate such potential in the exemplary context of electrophysiological signal delivery and acquisition.

4.3 Experimental and Characterization Section

4.3.1 Materials

Chloroauric acid ($HAuCl_4$), 4-mercaptobenzoic acid (4-MBA), sodium chloride, sodium hydroxide, sodium phosphate monobasic, sodium nitrate, sodium sulfate, sodium bromide, sodium iodide poly(diallyldimethylammonium chloride) solution (PDDA), polyethylene terephthalate (PET) thin film, Sylgard-184 silicone elastomer (PDMS), acrylic acid (AAc) and Phosphate Buffered Saline (PBS) solution were purchased from Sigma-Aldrich, Inc. Ethanol was purchased from Fisher Scientifics, Inc.

Ten20 conductive paste and Ag/AgCl electrodes were purchased from OpenBCI, Inc. Lithium phenyl-2,4,6-trimethylbenzoylphosphinate (TPO-Li) was purchased from Arkema Inc. All chemicals were used without further treatment.

4.3.2 Ink formulation

Stock solutions with different components were prepared separately: 6 mg mL^{-1} TPO-Li aqueous solution, 60 mg ml^{-1} HAuCl4 aqueous solution, 10 mg ml^{-1} 4-MBA ethanol solution, 100 mg mL^{-1} NaOH aqueous and DI water. The printable gold inks in this work were formulated by mixing the as prepared stock solutions of TPO-Li, $HAuCl_4$, DI water, 4-MBA and NaOH in the volume ratios of 1:0.125:0.125:0.015:0.015. Then certain amount of sodium salts was added and mixed under vortex to form the printing ink with specific anions.

4.3.3 Substrate treatment

Substrates were coated with PDDA to assist the seeding process of AuNPs. Glass and PDMS substrates were first rinsed with 2-propanol, DI water and ethanol under ultrasonication in sequence, then dried with air. Only water rinsing was conducted on PET substrate to avoid the damage from organic solvent. The substrates were then subjected to oxygen plasma treatment to make the surface reactive and immersed in a 0.1M PDDA aqueous solution for an hour. Eventually, the coated substrates were rinsed with DI water and dried with air at room temperature.

4.3.4 Printing architecture

The bottom-up printing setup consists of a DLP-based projector PRO4500 from Wintech Digital System Technology Corporation, a motorized translation stage mounted to a motor controller and optical accessories from Thorlabs, Inc. The intrinsic resolution of the printer is around 30 μm.

4.3.5 Printing procedure

All the printing proceeds in air under ambient conditions. Adequate amount of the inks was then placed on the substrates. Then a designed pattern was projected onto the top surface of the transparent substrates. As the light irradiated on the substrate, the photoreduction reaction occurred and generate AuNPs at the irradiated sites. The projected pattern will be kept for a certain period of time to keep the reaction ongoing. After printing, the substrates with deposited gold were rinsed by ethanol and dried in air.

4.3.6 Scanning microscope imaging and processing

A scanning electron microscope (SEM) was used to study the microstructures of the printed gold and measure the particle sizes and the porosity of the printed gold. The SEM images were obtained by using ZEISS Supra 40VP SEM. The as-printed samples were directly observed under SEM without further treatment. The obtain SEM images were smoothed, sharpened and analyzed using the software ImageJ. The particle sizes were determined by measuring longest length of the particles. To measure the porosity,

the printed Au patterns were approximated as porous 2D films. SEM images were processed in ImageJ where threshold tool was applied to obtain black and white images. Then specific areas were selected to measure area of pores and the mean pore area/selected area was calculated as the porosity.

4.3.7 Transmission and Reflectance spectra

The transmission and reflectance spectra of the printed Au patterns were measured by USB2000+UV-VIS-ES spectrometer with a DH-2000-BAL UV-VIS-NIR light source from Ocean Optics, Inc. The spectrometer was connected to DM5000 B microscope from Leica Microsystems GmbH.

4.3.8 pH value measurement

The pH values of the precursor inks were measured by FiveEasy Plus FP30 pH meter from Mettler-Toledo GmbH.

4.3.9 Thickness measurement

The thickness of the printed gold patterns was measured with Phase-Shift Interference (PSI) mode by Bruker NT9300 optical profiler from Bruker corporation.

4.3.10 Conductivity measurement

The sheet resistances of the printed gold electrode were measured with a four-point probe tester from Suzhou Jingge Electronic Co., Ltd.

4.3.11 Resistance stability measurement

A rectangular gold pattern was printed on PDDA-coated PDMS thin film to measure its resistance stability under inward and outward bending and stretching. The resistance of the printed gold was measured by the 2450 digital multimeters from Keithley Instrument. A Cellscale Univert mechanical tester was used to conduct cyclic stretching on the samples. The resistance for long-term electrical stability of the printed gold was measured by an electrochemical workstation, CHI660E from CH Instrument. The data were recorded at the voltage of 0.1V for 1 minute for each test.

4.3.12 Electrochemical impedance measurement

Electrochemical impedance spectra (EIS) were measured by two-electrode configuration, where a pair of printed Au electrodes with an area of 2 mm x 2 mm were used. Another pair of porous Au electrodes with same size for comparison was prepared by Pelco Auto Sputter Coater SC-7, Ted Pella Inc. PBS solution was used as the electrolyte for the tests. The EIS were acquired by using an electrochemical workstation, CHI660E from CH Instrument. The data were recorded at the initial voltage of 0 V with an amplitude of 5 mV at the frequency in the range of 1-10^4 Hz.

4.3.13 Electrical stimulation and measurement of the flytrap

A pair of gold electrodes were printed on a PET substrate and (exposed areal of ~5 mm^2) coated with a thin layer of poly(acrylic acid) (PAAc) hydrogel was attached to the lower epidermis of the flytrap lobe for electrical stimulation, which was applied by a square

wave alternating voltage (± 3.0 V, Frequency: 2 Hz) continuously. Another pair of printed gold electrodes coated with PAAc hydrogel was attached onto the other lobe of the same flytrap for measuring the action potential. The electrical signals are collected by the 2450 digital multimeters from Keithley Instrument.

4.3.14 Ex vivo ventricular pacing

A pair of gold electrodes were printed on a PET substrate and coated with a thin layer of PAAc hydrogel as an adhesive layer. A postmortem study was performed in a male Yucatan miniature pig (S & S Farms, Ranchita, Calif). All animal studies were approved by the UCLA Office of Animal Research in compliance with the UCLA IACUC protocols. The porcine epicardium was exposed through a thoracotomy, and the epicardium of the right ventricles was attached with printed gold electrodes. External pacing was conducted after euthanasia, with an amplitude of 2-3 V, a pulse width of 1 ms, and a pacing rate of 60 beats per minute.

4.3.15 ECG, EEG, and EMG measurements

Electrocardiogram (ECG), electroencephalogram (EEG) and electromyogram (EMG) are measured and recorded by using Cyton + Daisy biosensing board (16 channels) connected with either the printed Au electrodes or the commercial Ag/AgCl electrodes. A health volunteer is used as the human test subject. Ten20 conductive paste is applied evenly on the skin of the volunteer before attaching the conformal Au electrodes. No conductive paste is required for the Ag/AgCl electrodes due to the adhesive hydrogels

onside. The software OpenBCI GUI is used to control the board to collect the data.

4.3.16 Study approval

All experiments including the human testing and animal experiments were carried out in full compliance with local laws and ethical guidelines. Consent was obtained from the human subject involved in this study.

4.3.17 Statistical Analysis

All values of significance were determined using a one-way ANOVA with Microsoft Excel software. The sample size for measuring the particles sizes equals to 80 for each recipe or condition analysis. The sample size for measuring thickness and porosity equals to 5 for each recipe or condition analysis. All raw data collected for ECG, EEG and EMG tests were filtered with a Butterworth filter using Python code (5-50 Hz for ECG and EMG signals, 7-13 Hz for EEG signals, with a notch at 60 Hz).

4.4 Result and Discussion

4.4.1 Process and Mechanism

A DLP-based projecting system with 385 nm UV light source was employed to achieve the metallic gold patterning (**Figure 4.1**a). Digital images were projected on the interface between the precursor ink and the transparent substrates. A typical ink consists of chloroauric acid ($HAuCl_4$, 48 g L^{-1}) as the gold source, photo-initiator lithium phenyl-2,4,6-trimethylbenzoylphosphinate (TPO-Li, 0.6 g L^{-1}) to generate free radicals

for reduction reaction, and sodium chloride (NaCl, 20 g L^{-1}) as a printing-aid agent. This ink allows us to directly print Au patterns on either rigid or flexible substrates with a positively charged polymer coating (**Figure 4.1**b).

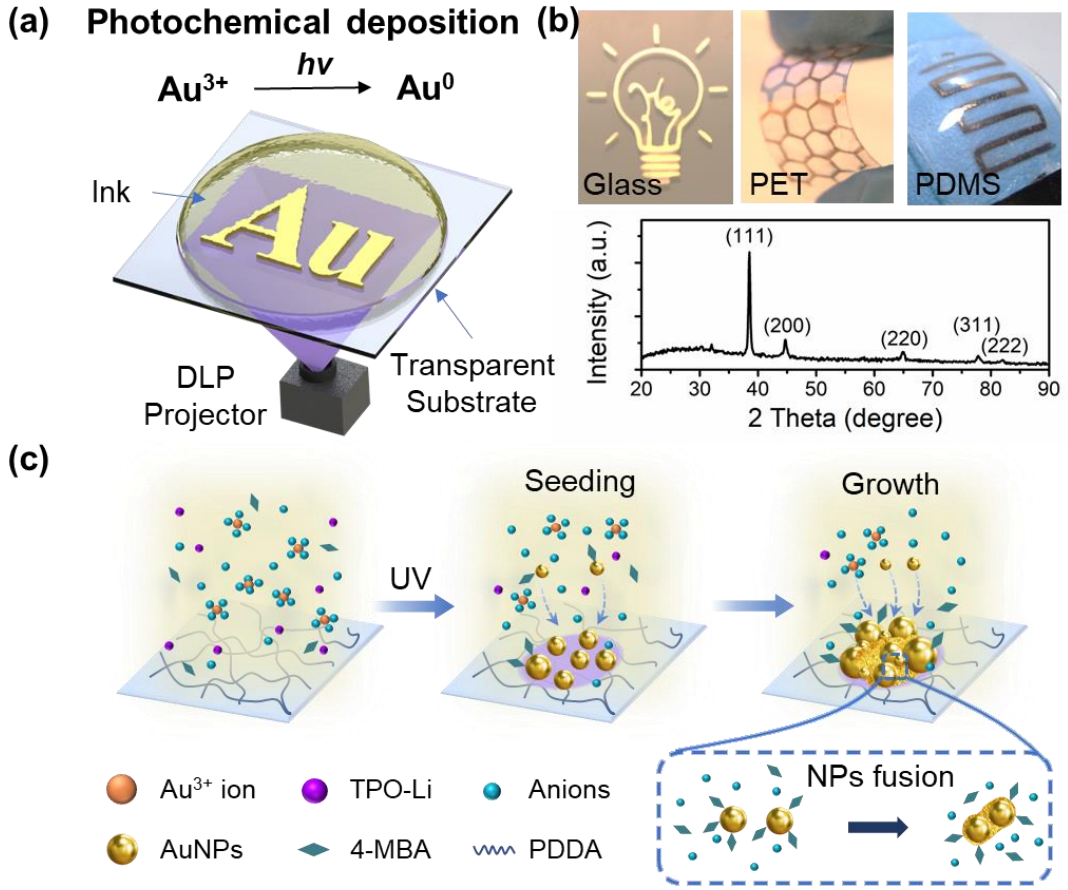

Figure 4.1 (a) Schematic of the DLP-based printing setup. (b) The printed patterns on different substrates (top) and XRD spectrum of printed gold (bottom). (c) Principle of the printing involving the reduction of gold ions, the seeding of AuNPs, and the growth of AuNPs network (top). The zoom-in AuNPs fusion occurs during the growth process (bottom).

We investigated the APD process with the typical gold precursor ink and proposed the printing principle (**Figure 4.1**c). Within 5 minutes of projection, a layer of loosely

distributed AuNPs can be observed deposited onto the substrate (**Figure 4.2**a,d). Most of the AuNPs were around 60 nm in diameter. Adjacent AuNPs attached to each other forming a AuNP network with a porosity of 12% (**Figure 4.3**c). However, the sharp and clear outlines of the AuNPs indicated that only a limited amount of AuNPs were fused together to allow electrical current to flow through. Lacking in long-range, continuous, conductive paths, this printed Au pattern was non-conductive. As the deposition proceeded to 10 minutes, the conductivity of the printed pattern drastically increased to 3.6 $x10^6$ S m^{-1}, due to an abundant formation of conductive paths. This was confirmed by SEM imaging (**Figure 4.2**b,e), which also showed the growth of AuNPs (**Figure 4.3a**). Despite the vacant regions between AuNPs seem to expand in the SEM image, the total porosity of the AuNPs network decreased to around 9%. We believe this can be attributed to the recrystallization of small AuNPs. Small and unstable nuclei below the critical nucleation radius would eventually be consumed to form conductive paths while the others would grow larger. As the printing continued to 20 minutes, we can obtain a dense and continuous AuNPs layer with a higher conductivity of 6.4 $x10^6$ S m^{-1}. The porosity of the network dropped to around 2% and remained stable even with further illumination. The densification process of the Au pattern was also reflected by the decrease of its light transmittance and the rapid increase of the optical reflectance throughout the printing process (**Figure 4.3**e,f). Although the irregular shape of AuNPs can still be observed, the edges of the AuNPs have become obscure (**Figure 4.2**c,f). Given previous work has concluded the specific ion effect induces destabilization and gel formation in metal nanoparticles solutions,[33] we believe that the presence of Cl^- ions

in our procedure promoted in-situ fusion between the newly generated AuNPs and subsequently deposited AuNPs thus filling the initially observed gaps within this short period of time (**Figure 4.2**e,f).

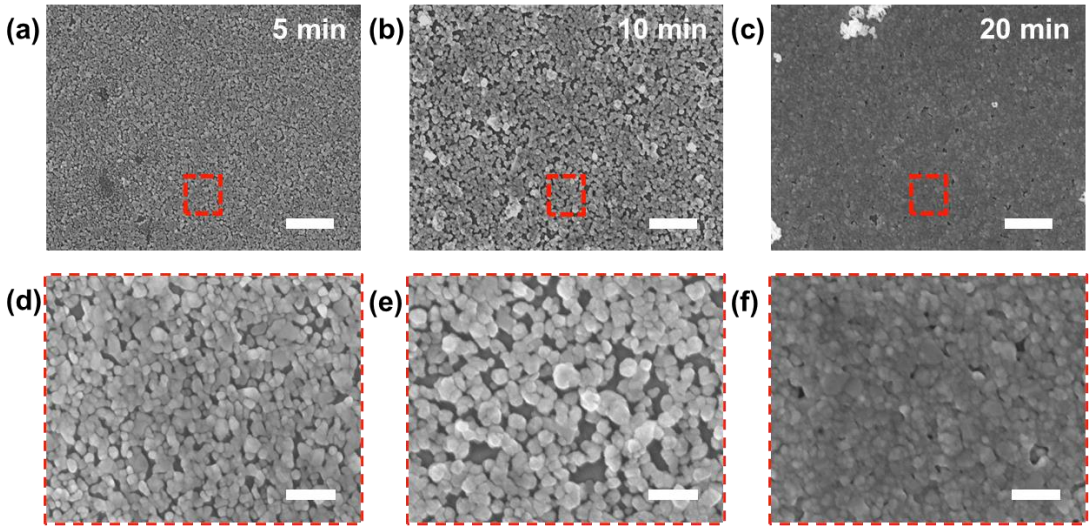

Figure 4.2 (a-c) SEM images of the printed gold with illumination time of 5, 10, and 20 minutes. (d-f) Zoom-in microstructures of the printed gold. Scale bar: 1 μm for a-c, 300 nm for d-f.

In addition, the thickness variation of the printed Au was also studied during the printing process of the typical ink (**Figure 4.3**b). The growth rate of the thickness was relatively slow within the first 5 minutes (3.1 nm min^{-1}). Once a layer of separated AuNPs is formed, the deposition rate rapidly increased (5.6 nm min^{-1}) and an Au pattern over 100 nm thickness was obtained in 30 minutes of printing. It was observed that the growth rate (the slope of the thickness-printing time curve) slowly decreased after 15 minutes of printing, which we attributed to the decline in the number of available

photons for the reaction. This was validated by the rapid decrease of transmittance of the printed Au pattern at 385 nm during the printing process (**Figure 4.3**e). After 30 minutes, we observed the transmittance dropped to below 2% as a dense pattern formed in the path of the UV light source located below the sample, hindering further deposition from taking place above. The decline of available photons as the printing proceed could be attributed to the printing setup, in which the UV exposure occurred from the backside of substrates. If UV patterns are projected from above, some AuNPs can be generated via homogeneous nucleation forming suspension and scattering the light, which eventually leads to unsuccessful patterning. Challenges are expected to be addressed in controlling the kinetics of the photoreduction reaction to confine it to the liquid-solid interface. By optimizing the ink recipe, top-down DLP printer with light projected from above substrates can replace the current bottom-up system, which endows broader applications for the APD method.

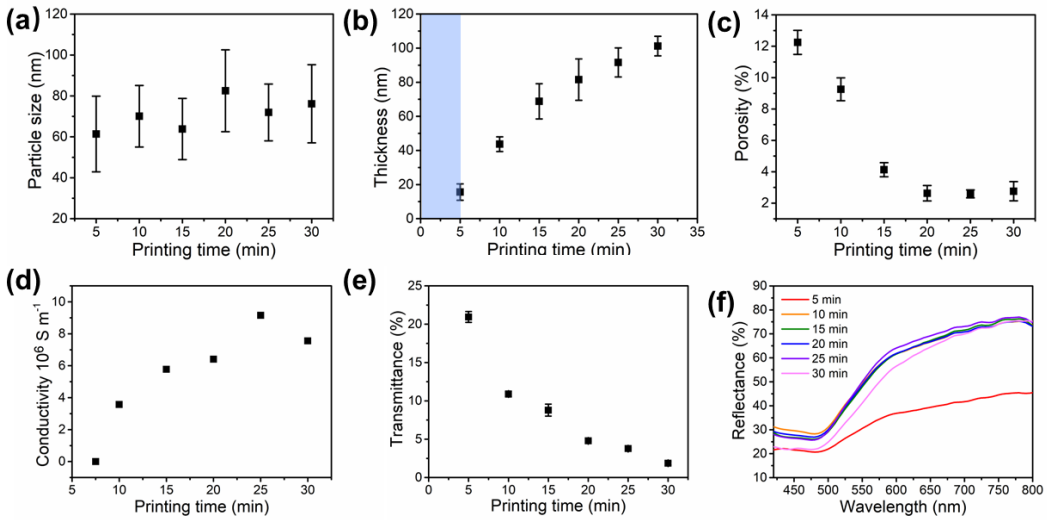

Figure 4.3 (a) Deposited Au nanoparticle sizes as a function of printing time. (b) Thickness of printed gold patterns as a function of printing time. (c) Porosities of

printed gold patterns as a function of printing time. (d) Conductivity of printed gold patterns as a function of printing time. (e) 385 nm UV transmittance of printed Au patterns as a function of printing time. (f) Reflectance spectra of printed Au patterns with different printing time.

The APD printing involved three different processes: reduction of gold ions, seeding of AuNPs, and anion-assisted growth of AuNPs network (**Figure 4.1**c). As the ink was placed on the substrate, no reaction would occur until a UV light pattern was projected on the interface between the substrate and ink. Upon UV photon flux, radicals were in-situ generated through the cleavage of the Norrish type I photo-initiator, TPO-Li, to reduce Au^{3+} to Au^{0}.[34] This photon-induced reduction proceeded until the light was blocked by the deposited layer as mentioned above. The produced Au^{0} aggregated into Au nanoparticles (AuNPs) and 4-mercaptobenzoic acid (4-MBA) attached to the surface of AuNPs via thiol-gold bonding. 4-MBA can help stabilize the AuNPs and restrict their growth.[35–37] A limited quantity of 4-MBA was used in the ink to obtain AuNPs with appropriate sizes to serve as the foundation, upon which further growth and subsequent in-situ fusion of AuNPs occurred. Meanwhile, Cl^{-} ions were adsorbed onto the AuNPs due to the electrostatic force, making them negatively charged on their surfaces. Once the AuNPs formed, they would then undergo the seeding process. To anchor the AuNPs, the substrate was coated with a polymeric layer of high positive-charge density, specifically poly(diallyldimethylammonium chloride) (PDDA). The

PDDA coating on the substrate is essential for printing, in the absence of which complete Au patterns can hardly be deposited on substrates (**Figure 4.4**c). Two driving forces that caused the aggregated AuNPs to deposit onto the substrate were settlement driven by gravity and the electrostatic attraction between the AuNPs and the polymer coating, where the latter was more dominant. As the small AuNPs were deposited on the substrate, they acted as seeds for further growth. This seeding process is reflected in the observation of a relatively slow deposition rate during the first 5 minutes of the printing process, which is kinetics-dominated. After that, the deposited AuNPs grew larger (**Figure 4.2**d and **Figure 4.3**a), and new smaller AuNPs formed (**Figure 4.2**f) due to the incessant reduction of Au^{3+} to Au^{0}. In conclusion, we suggest that the synergistic effect of the growth of AuNPs and the filling of newly formed ones densified the AuNP network. Anions, like Cl^- ions, then played a significant role in achieving a conductive path between the neighboring AuNPs. Specifically, the presence of anions altered the aqueous environment surrounding the AuNPs. The strongly hydrated kosmotropic anions, like Cl^-, were rather repelled from the interface between the AuNPs and the solution, resulting in greater surface energy on the AuNPs.[32,33] This drove fusion as the uncapped AuNPs approach each other, to form conductive paths and eventually develop into a conductive AuNP network via repeating the process above.

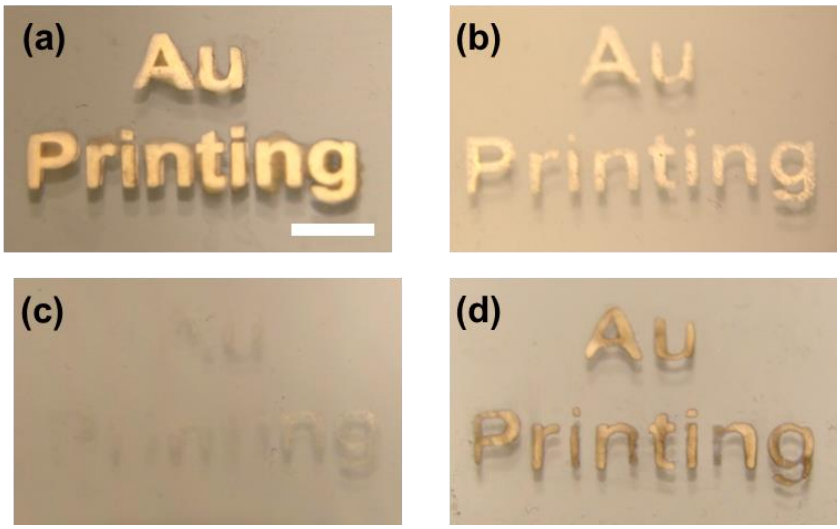

Figure 4.4 Optical images of printed Au patterns with different inks and substrates. (a) Standard ink with 4-MBA and 20 g L^{-1} NaCl printed on glass with PDDA coating; (b) ink without additional salts printed on PDDA-coated glass; (c) standard ink printed on glass without coating; (d) ink without 4-MBA printed on PDDA-coated glass. Scale bar is 5 mm.

The flux of UV photons controlled by the projector also significantly affected the thickness of the Au pattern (**Figure 4.5**). An increase in light intensity can lead to the formation of a thicker Au layer. The properties of the printed Au pattern were not only determined by the illumination time and the intensity of light source, but also significantly dependent on the chemical composition of the precursor inks. We investigated the influence of pH values on the precursor. Different traces of sodium hydroxide solution were added into the original, unaltered precursor to tune the pH values of the inks (**Figure 4.6** and **Table 4.1**). The pH value of the original precursor ink was 2.13, conditions under which TPO-Li accepted protons, becoming less

hydrophilic, and causing it to precipitate. Even though the photo-initiated reduction can still occur, the resultant white precipitant scattered light and acted as nucleation sites, which lead to inaccurately patterned printing. If the pH value is tuned to be above 7, TPO-Li become unstable and directly reduced Au^{3+} into Au^{0} without any luminous energy input. The ink was colorless as prepared, but at this pH a dark violet AuNPs suspension formed in minutes. Additionally, black Au foam eventually formed due to the presence of Cl^- salt when the alkaline precursor was allowed to sit undisturbed for at least 6 hours (**Figure 4.6**d,f). This observation was previously noted in works pertaining to a metal foam synthesis, further demonstrating the important role of anions in our printing strategy.[33] Therefore, we conclude that the stability of the ink is determined by the behavior of TPO-Li under different pH conditions. The ideal pH value for the precursor was validated to be around 6. Under this condition, there was no formation of either the TPO-Li precipitant or AuNPs, and the precursor ink still functioned properly succeeding 48 hours of storage in the dark and at room temperature.

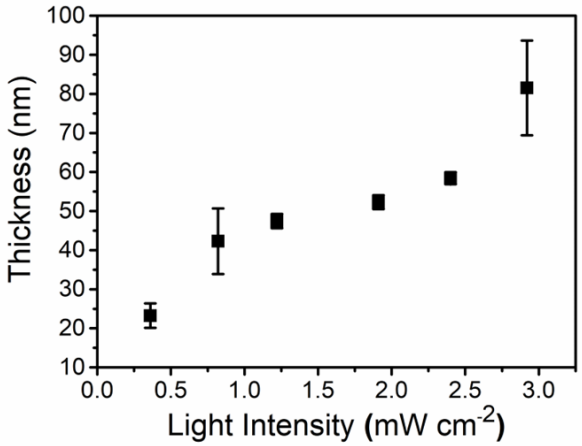

Figure 4.5 Thickness of printed Au patterns as function of projected light intensity.

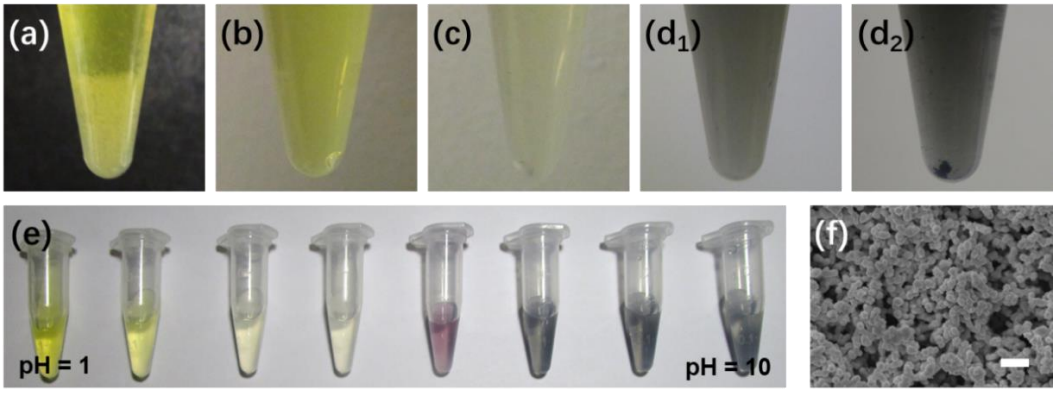

Figure 4.6 (a-d) Precursor inks of different pH values. (e) Precursor inks with different pH values corresponding to Table S1. (f) SEM image of the black Au gel precipitated from ink sample d. Scale bar is 1 um.

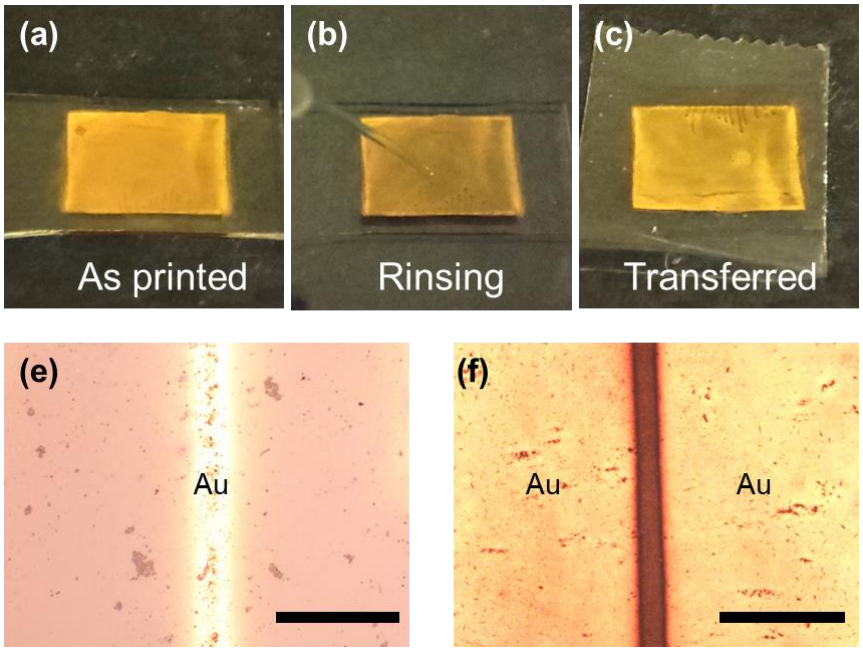

Figure 4.7 Optical images of (a) the Au pattern as printed, (b) the pattern being rinsed with ethanol, and (c) the pattern transferred onto an adhesive tape. (d) Thinnest line width (29 μm) and (e) resolution (98 μm) of the printed Au pattern via APD with the printing setup in this work. Scale bar: 100 μm for a, 500 μm for b.

Table 4.1 pH values of precursor ink samples with different amount of NaOH additives.

Ink Sample	100 mg ml^{-1} NaOH	pH
a	0 μL/1.25 ml	2.13
b	15μL/1.25 ml	5.99
c	30μL/1.25 ml	7.97
d	60μL/1.25 ml	10.50

4.4.2 Specific Ion Effects on the Printed Au Patterns

We investigated the properties of the Au patterns printed for 20 minutes with varied NaCl concentrations to further demonstrate the significance of the Cl^- in the APD process. Without additional sodium salts, a loosely arranged network with a porosity of 11% was deposited on the substrates. (**Figure 4.8**a) The deposited Au pattern was around 51 nm thick, while the measured conductivity was $1.67x10^6$ S m^{-1}. Even though large gaps can be observed among AuNPs, conductive pathways can still form due to the limited amount of Cl^- in the $HAuCl_4$ stock solution. As the NaCl concentration was increased to 25 g L^{-1}, a thicker pattern (~81 nm) with a higher density (porosity of 3.4%) of larger AuNPs of 59 nm in length was printed (**Figure 4.8**b). As mentioned above, Cl^-, as a kosmotropic ion, can stabilize the water-water interactions surrounding AuNPs and lower the surface energy. This allowed the AuNPs to grow and sinter together to form more conductive pathways, which consequently raised the conductivity to 1.08×10^7 S m^{-1}. Such a high conductivity is comparable to those obtained by inkjet printing, which however requires high temperature annealing (**Table 4.2**). As we continued to increase the concentration to 50 g L^{-1}, both conductivity and thickness decreased while the porosity increased slightly to 4.9%. We believe that the high Cl^- concentration made the AuNPs more negatively charged, leading to greater repulsion

between AuNPs due to electrostatic forces, which ultimately prevented the AuNPs from sintering (**Figure 4.8**c). As a result, fewer conductive pathways could form, compared to using an ink with moderate concentrations of NaCl. In general, we suggest that Cl^- can lower the surface energy of AuNPs promoting their sintering and growth at moderate concentration. It can also stabilize the AuNPs by blocking active sites and forming electrostatic repulsion between them. The synergistic effect of both processes eventually led to the porosity change with varied Cl^- concentration (**Figure 4.8**d).

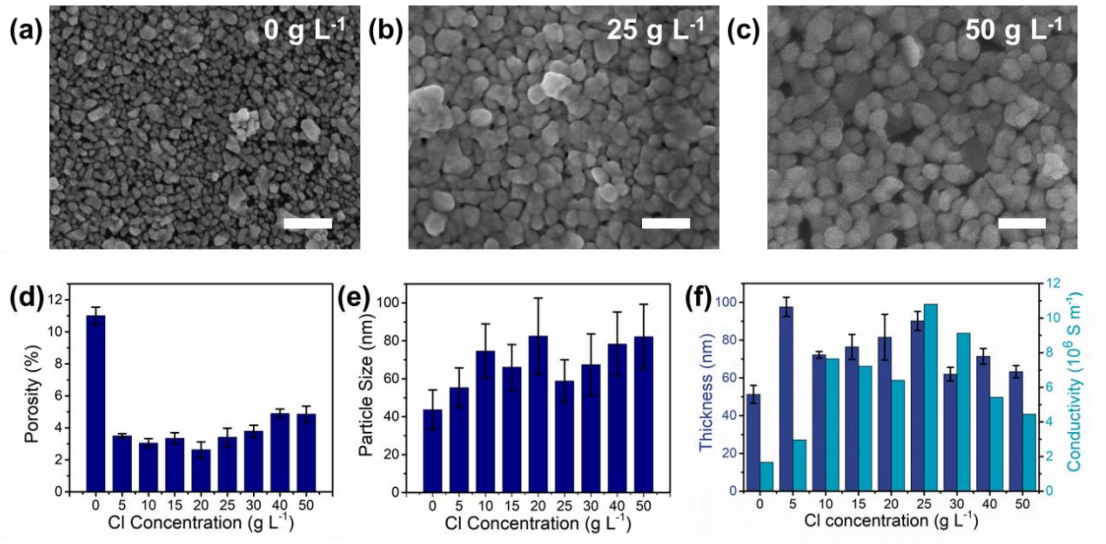

Figure 4.8 (a-c) SEM image of printed Au using inks with NaCl concentrations of 0, 25, 50 g L^{-1} respectively. (d) Porosity as a function of Cl^- anion concentrations. (e) Particle sizes as a function of Cl^- anion concentrations. (f) Thickness and conductivity as a function of Cl^- anion concentrations. Scale bar is 200 nm.

Table 4.2. Comparison between different gold printing methods.

Method	Metal source	Process	Morphology	Average layer thickness (nm)	Electrical Conductivity		Ref.
					10^7 S/m	bulk%	
APD	Metal salt solution	RT, no annealing	Porous or smooth	32-257	1.07	24	This work
PPD	Metal salt solution	RT, no annealing	Smooth	<40	/	/	28
LPP	Metal salt solution	RT, laser sintering	Rough	~100	/	/	26
DLP	Metal salt solution	RT, TiO_2 substrate	Particles	/	None	None	24
DLP-PE	PVD	RT, Etching	Rough	30-80	/	/	39
Inkjet	Au-organic ink	Annealing 280°C	Porous	65-75	1.9	43	40
Inkjet	AuNPs ink	Annealing 500°C	Rough	60	0.5	11	41
Inkjet	AuNPs ink	Annealing 350°C	Rough	100	1.01	23	42
Inkjet	AuNPs + PEDIT:PSS	RT, no annealing	Rough	/	0.002	5.2E-4	43
Micro-contact	Functional AuNPs ink	Annealing 200°C	Continuous	70	1.0	22	44
Vacuum evaporation	Bulk Au target	Vacuum	Continuous	70	2.0	45	44
DLW	Metal salt + polymer	Annealing 200°C	Rough	/	0.22	5	17
DLW	Metal salt ionic liquid	RT, no annealing	Rough	/	0.6	14	45

Conductivity of bulk gold: 4.4×10^7 S/m

APD: Anion-assisted photochemical deposition.

PPD: Poly-assisted photochemical deposition.

LPP: Laser projection printing.

DLP: digital light processing.

DLP-PE: Digital light processing photochemical etching.

PVD: Physical vapor deposition.

DLW: Direct laser writing.

Other sodium salts at equal concentrations were utilized in various precursor inks to investigate the influence of these different anions on gold printing via APD. The microstructures (**Figure 4.9**), the porosities (**Figure 4.10**a) and the particle size (**Figure 4.10**b) were shown to trend with salt variation that expectedly corresponds to the Hofmeister series: Na_2SO_4 > NaH_2PO_4 > NaF > NaCl > NaBr > $NaNO_3$ > NaI. Printed Au with high density and small particles can be achieved with the presence of kosmotropic SO_4^{2-} anions, while a loose network with much larger AuNPs can be obtained through the addition of chaotropic I^- ions. Continuous and more packed AuNPs networks form with the presence of an ionic kosmotrope. These kosmotropic anions can be utilized to lower the surface energy of AuNPs, promote their growth and sinter the AuNPs. On the other hand, the chaotropic ions tended to be adsorbed onto the surface of AuNPs, leading to the repulsion of negatively charged AuNPs. Thus, AuNPs were loosely distributed on the substrate and conductive paths are barely formed. Despite the great correlation between the structures and anions, the thickness and conductivity of the printed Au were not closely related to the Hofmeister series (**Figure 4.10**c and **Table 4.3**). The thickness and conductivity involved more complex kinetics and thermodynamic processes during the printing. Multiple factors including, but not limited to, crystalline structures, particle sizes, deposition rate, sintering of AuNPs, interaction between Au ions and anions, and the possible formation of Au^+ ions can contribute to the final performance of the deposited Au. Even though there are still challenges to fully understand the deposition process, tunable porous structures of Au patterns can be achieved via APD, which is significant for fulfilling broad applications

in electronic industries such as electrode fabrication and flip chip packaging. Therefore, we plan to conduct more fundamental studies on the deposition process in the future.

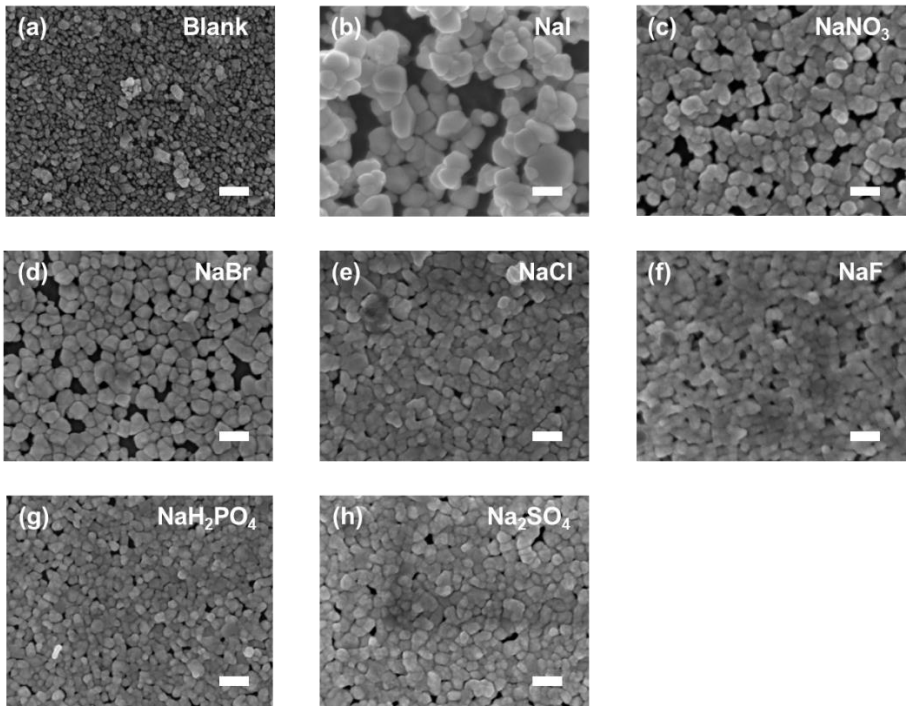

Figure 4.9 SEM images of deposited Au printed with precursor inks of (a) no additional salt and (b-h) different salt additives with the same mole concentration. Scale bars are 200 nm.

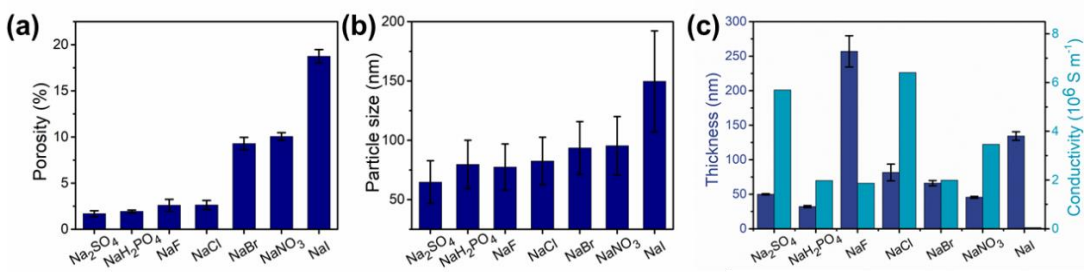

Figure 4.10 (a) Porosity of samples with different anions. (b) Particle sizes of samples with different anions. (c) Thickness/conductivity of samples with different anions. Data represents mean ± standard deviation, n = 5, significance determined by one-way ANOVA test. Scale bar, 200 nm for a-c.

Table 4.3 Thickness and conductivity of printed Au using precursor inks with different salt additives.

Salts	Thickness (nm)	Conductivity (10^6 S m^{-1})
Blank	51.29±4.77	1.6707
NaI	134.24±6.19	/
$NaNO_3$	45.56±1.33	3.4615
NaBr	66.02±3.81	1.9920
NaCl	81.53±12.13	6.4083
NaF	256.89±22.57	1.8670
Na_2HSO_4	32.04±1.47	1.9754
Na_2SO_4	49.88±0.94	5.6939

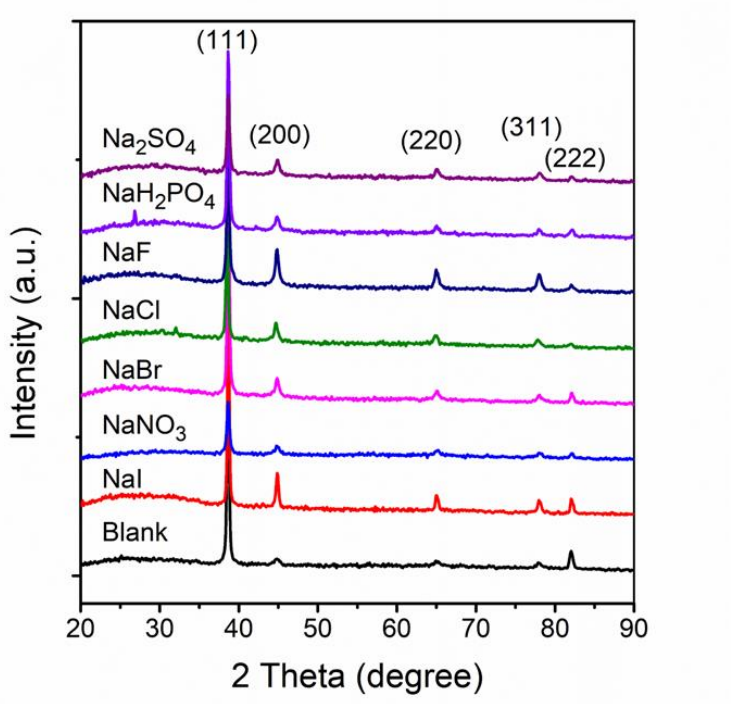

Figure 4.11 XRD spectrums of printed Au using inks with different anions.

4.4.3 Electromechanical Performance

We demonstrated that our APD method can be conducted on both rigid and flexible substrate (**Figure 4.1**b & **Figure 4.12**a). Au patterns on both glass and PDMS substrates were incorporated into circuits to power LEDs. The long-term stability of electrical performance was verified by measuring the resistance change in ambient condition. No obvious degradation in conductivity of the pattern was observed (**Figure 4.13**a). At the same time, we also looked at the resistance variation of the printed Au pattern on a soft PDMS substrate under bending and stretching. Au strip patterns were printed with the typical ink onto a flexible PDDA-coated PDMS thin film. Changes in resistance due to different bending radii during inward and outward bending were measured respectively (**Figure 4.12**b). By bending the pattern outward at a radius anywhere from 24 mm down to 8 mm, the change in resistance was negligible given the ductility of gold network. As the bending radius decreased further, however, the resistance rapidly increased due to the breakdown of conductive paths under localized stretching (R/R_0 increased from 1.22 to 4.62). Alternatively, the resistance reduced as the sample was bent inwards. Compressive strain enhanced the packing density of the AuNPs, creating more conductive paths through the networks. As the inward bending radius decreased to 4 mm, the resistance of the gold network dropped to less than half. Once the printed gold returned to its original flat state, the resistance also restored. In addition to the bending tests, the printed Au strip patterns were stretched under different strains ranging from 0 to 50% (**Figure 4.12**c). As the strain increased, the resistance of the Au pattern also increased proportionally, making it possible to function as a strain sensor. As the strain

rose to over 50%, the printed Au pattern became non-conductive. The SEM images show that the printed Au pattern was an intact and connected layer before stretching at 50% strain (**Figure 4.12**e), while it broke into many small rectangular fragments after the stretching (**Figure 4.12**f). It is worth noting, even with the formation of cracks on the printed Au pattern under 50% strain, the pattern still partially restored its conductivity upon release. The resistance stability of the printed Au pattern was tested by stretching the sample to 50% strain 1,000 times (**Figure 4.12**d). The resistances were measured after a stretching cycle ended. The results showed that during the first three cycles, the resistance had almost no change due to the intrinsic ductility of gold. After that, the resistance increased and eventually stabilized at around twice the original value. Under multiple cycles of stretching, the printed Au layer broke down into fragments to release the stress, while some portions remained connected and formed conductive paths. Therefore, the Au patterns can reach a newfound stability with high conductivity under small strain.

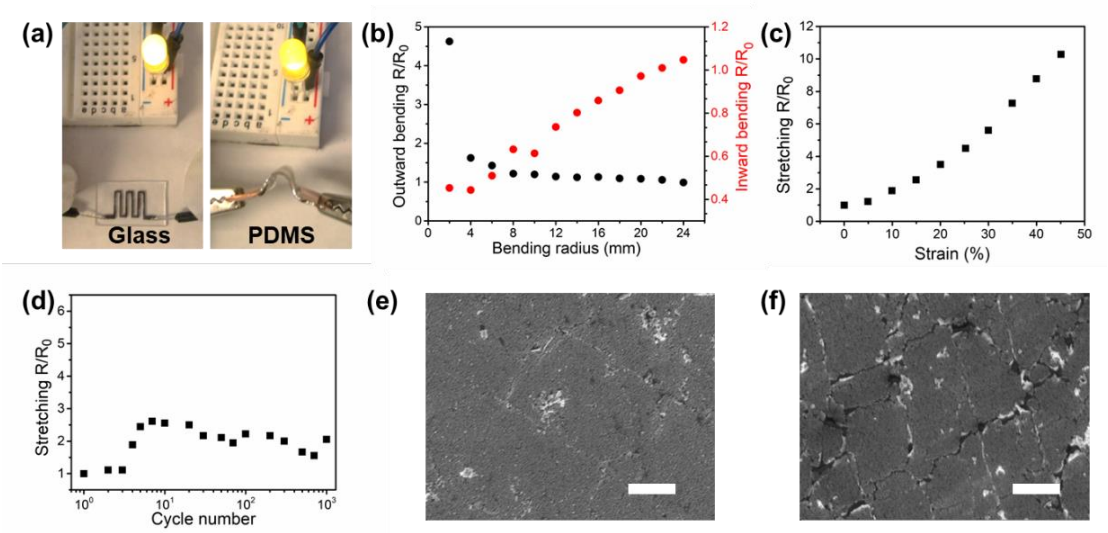

Figure 4.12 (a) Au circuit printed on rigid and flexible substrate connected with a LED

light. (b) Resistance stability of printed flexible Au electrode on PDMS substrate under inward and outward bending. (c) Resistance stability of printed flexible Au electrode on PDMS substrate under stretching. (d) Resistance cyclic stability of printed Au on PDMS with 50% strain. SEM images of printed Au pattern on PDMS substrate (e) before and (f) after stretching at 50% strain. Scale bar is 4 μm.

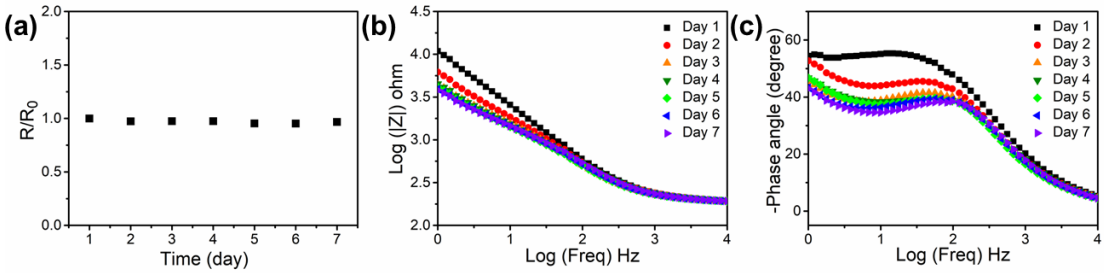

Figure 4.13 Long-term electrical and electrochemical performance of printed Au patterns. (a) Resistance stability and (b) Bode plots for the printed Au electrodes within 7 days.

4.4.4 Tunable Electrochemical Performance

Due to the tunability of the properties and morphologies of the printed gold patterns, we suggest porosity of the gold networks may contribute to their electrochemical performance as electrodes. Therefore, we investigated the impedance performance of the printed gold electrodes. Three porous Au electrodes with similar thickness were prepared by printing with low (~3 mW cm^{-2}) and high intensity (~5 mW cm^{-2}), and sputtering. Both the printed Au electrodes showed comparable or lower impendence than the sputtered one, validating the potential for application as electrodes in

electrochemical reaction systems (**Figure 4.14**b). For the electrodes printed with low intensity (low-Int electrodes), the structure was more porous (**Figure 4.15**a). In Nyquist plots (**Figure 4.14**a), the smaller semicircle of the low-Int electrodes indicated its smaller charge transfer resistance (R2 in **Figure 4.16**) compared to the sputtered electrodes. In brief, the low-Int electrodes showed higher electrocatalytic capability and may benefit applications like electrocatalysis and electrochemical sensing. For the electrodes printed with high intensity (high-Int electrodes), the structure was denser (**Figure 4.15**b). In Nyquist plots (**Figure 4.14**a), no semicircle was observed for the high-Int electrodes, which indicated the active sites were blunted and electrochemical reactions were suppressed. This was also reflected in the increase of phase angles to around -80° at low frequency in Bode plots (**Figure 4.14**c). Therefore, the high-Int electrodes can provide stable transduction between electrons and ions at the same time with a lower impedance than the sputtered Au, which partially remedied the conflicts between low impedance and high stability of porous Au electrodes. In conclusion, the tunability achieved by APD allows us to adjust the electrochemical performance of the printed electrodes to meet the requirements of different applications such as electrocatalysis and electrophysical signal transmission with low impedance at the same time. This offers more significance of the Au electrodes fabricated via APD in future studies.

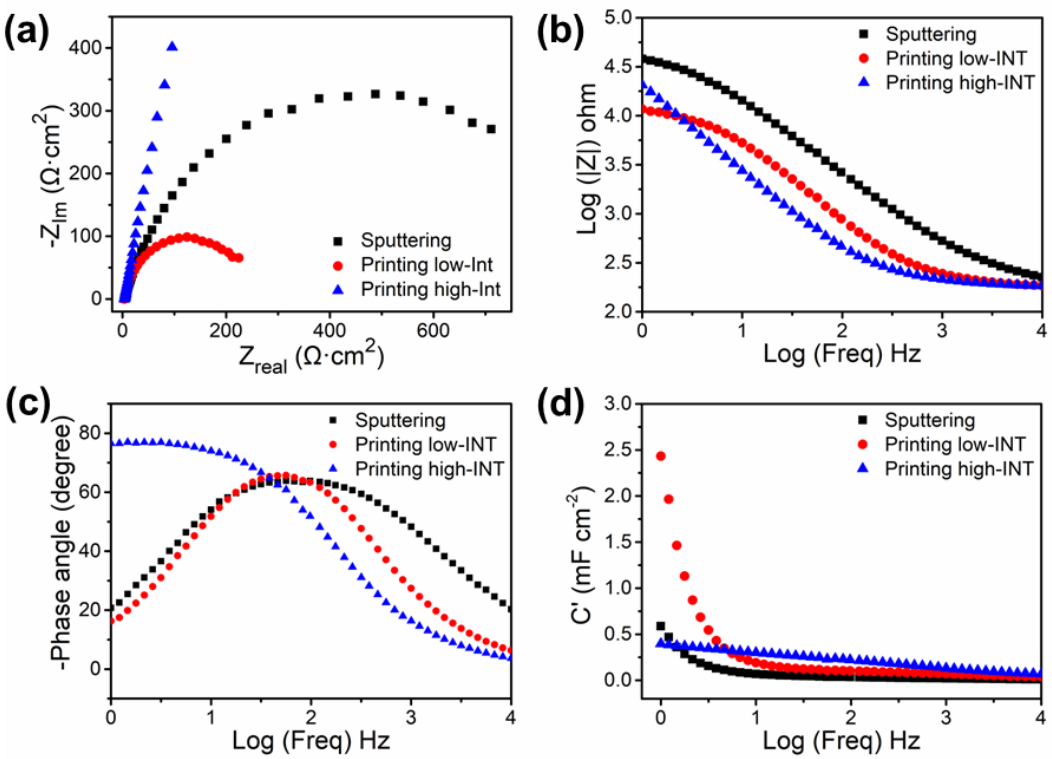

Figure 4.14 Electrochemical impedance spectra (EIS) within a frequency range of 1 - 10^4 Hz with an amplitude of 5 mV of sputtered gold and printed gold electrodes with different light intensity: (a) Nyquist plots for the gold electrodes. (b) Bode plots for the gold electrodes: Impedance as a function of frequency. (c) Bode plots for the gold electrodes: Phase angle as a function of frequency. (d) Capacitance as a function of frequency.

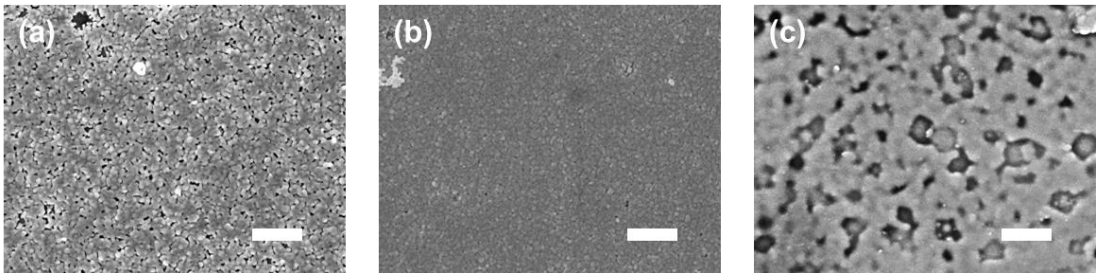

Figure 4.15 SEM images of (a) printed Au with low intensity (~3 mW cm^{-2}) and (b) high intensity (~5 mW cm^{-2}), and (c) sputtered Au. Scale bar is 1um.

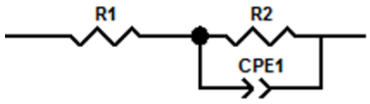

Figure 4.16 Equivalent circuit of the printed Au electrodes.

4.4.5 Conformable Electrodes for Electrophysiology Signal Transduction

To demonstrate the excellent conductivity, flexibility, conformability, and light weight of the gold electrode that we fabricated here, several biological applications involving electrophysiology signal delivery and acquisition were conducted. First, two soft electrodes were fabricated by printing Au films on two flexible PET thin films separately, and they can be conformally attached to the epicardium of the right ventricles of a porcine heart after euthanasia of the test subject (**Figure 4.17**a). To externally pace the heart with the printed Au electrodes, an electrical pulse at a condition commonly used for commercial gold electrodes was applied, specifically with an amplitude of 2-3 V, a pulse width of 1 ms, and a pacing rate of 60 beats per minute. The porcine heart was successfully paced, which exhibited an excellent charge delivery capability of the printed Au electrodes. Additionally, we took advantages of the printability by fabricating a pair of Au electrodes on a single PET thin film with a single exposure, and then conformally attached them to the small and soft lobes of a Venus flytrap by introducing a thin hydrogel as an adhesive layer (**Figure 4.17**b). The Venus flytrap can be modulated quickly from an “open” to a “close” state in less than 6 s through the compliant electrodes acting on a square-wave alternating voltage of 3 V, similar to the gold nanomesh electrodes reported previously (**Figure 4.17**b).[38] Such a patterning ability via APD allows for fast and facile fabrication of multiple electrodes

on one substrate with a single exposure, which may benefit complex biological modulation in future. Not only performing electrical stimulation (injecting electrons), the printed Au electrodes can be also used for recording (collecting electrons), owing to their high conductivity and conformability. The action potential during the flytrap's open-to-close actuation of a large deformation and curvature change was successfully recorded without an amplifier (**Figure 4.17**c). This indicates its excellent ability of acquiring electrical signals with a high signal-to-noise ratio.

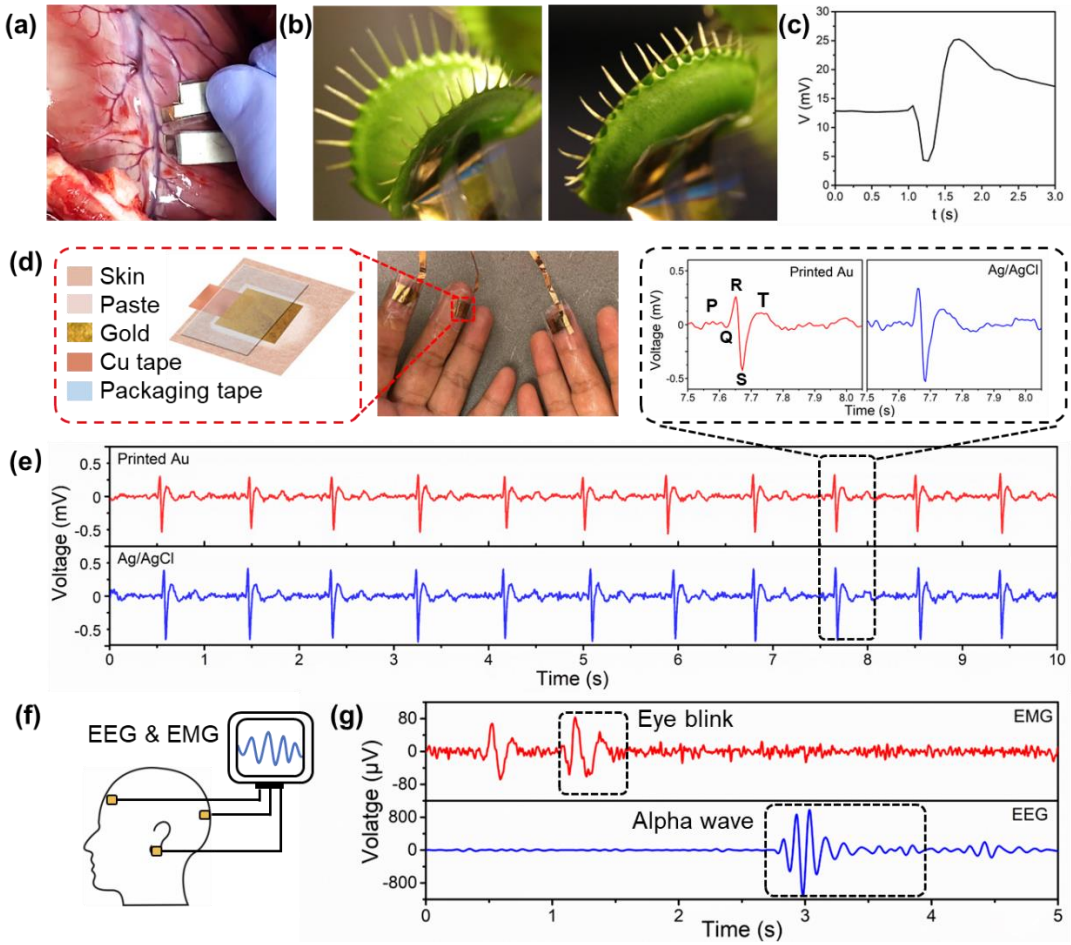

Figure 4.17 Conformable printed Au electrodes in electrophysiological signal delivery and acquisition. (a) A pair of Au electrodes attached to the epicardium of the right ventricles for the porcine heart pacing with an electrical pulse. (b) A pair of Au electrodes attached to the lower epidermis of a Venus flytrap lobe to modulate the lobe

shift from ‘open’ (left) to ‘close’ (right) state with a square wave electrical stimulation. (c) Action potential of the Venus flytrap actuator measured by the printed Au electrodes. (d) The laminate structure diagram and optical image of the printed Au electrodes for ECG test. (e) Pulse signal recording (10 s) and sample of a single beat (top), obtained by printed Au electrodes (red) and Ag/AgCl (blue) electrodes. (f) Schematic of EMG and EEG test. (g) EMG and EEG signal recordings during eye blink.

To further investigate the conformal Au electrodes’ ability to collect complex signals, electrocardiogram (ECG), electromyography (EMG) and electroencephalography (EEG) signals were acquired (**Figure 4.17**e, g). In the ECG tests, the printed Au electrodes and Ag/AgCl electrodes (as control) were attached to the fingers of a volunteer. The ECG signals were recorded for 10 s and the signals from a single beat were extracted from the data (**Figure 4.17**e). The P wave, QRS complex, and T wave were clearly observed in the ECG signals collected using printed Au electrodes. The total QRS wave amplitude of the signals collected by the printed Au electrodes was 0.684 mV, comparable to the one collected by Ag/AgCl electrode (0.868 mV). ECG signals were also recorded right after the volunteer’s engagement in squat exercises, showing the heart rate increased from 66 bpm to 102 bpm (**Figure 4.18**a). The signals were recorded for 5 minutes to highlight the reliability and stability of the printed gold electrodes (**Figure 4.18**b). The application of the printed Au electrodes was also demonstrated in EMG and EEG tests. Four electrodes were attached to the forehead, the back of the head, and both the earlobes of the human subject separately (**Figure**

4.17f). The EMG and EEG signals were recorded for 5 s, featuring the two eye blinks of the test subject. After the eyes of the test subject closed for about 1 s, an alpha wave signal was detected (**Figure 4.17**g). These results suggested that the printed Au electrodes can be safely and reliably used for electrophysiological signal delivery and acquisition.

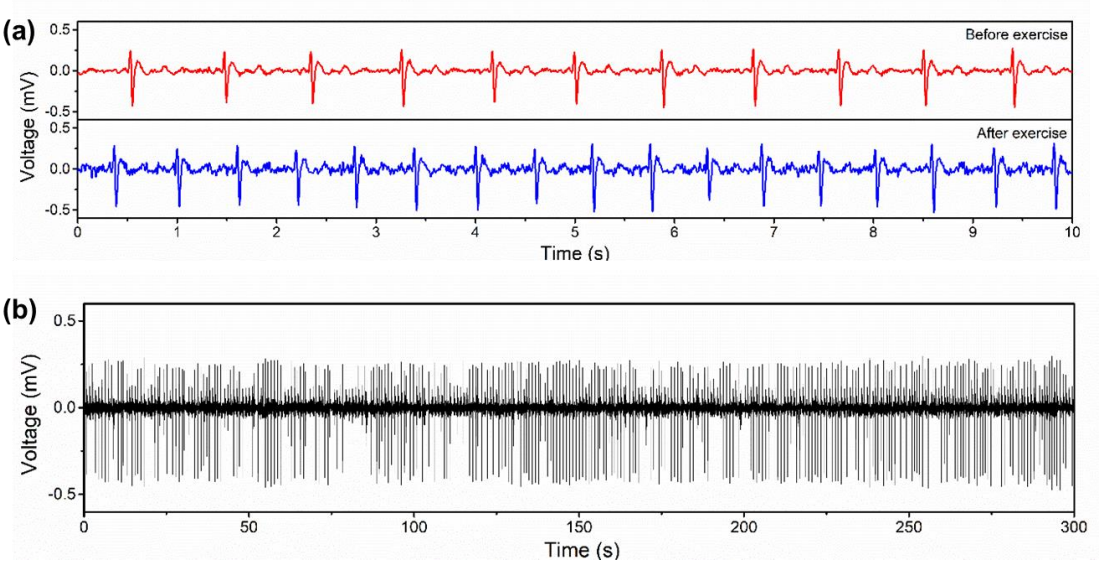

Figure 4.18 (a) ECG signals collected by printed Au electrode before and after exercise of the human test subject. (b) ECG signals collected by printed Au electrode for 5 minutes.

4.5 Conclusion

Herein we have demonstrated a facile direct patterning strategy to produce highly conducive metallic gold on various substrates under ambient conditions via APD. This approach combines projection lithography with specific ion effects to achieve a one-time patterning of gold without post annealing treatment, which simplifies the fabrication process of metal patterning by improving both its time- and cost-efficiency.

The typical printing process was investigated carefully, and a model involving three process was proposed to understand the principle of APD. Our results showed substantial tunability in the structures, electrical properties, and electrochemical performance of the printed gold. We further demonstrated the high conductivity (~10^7 S m^{-1}) and conformability of the Au electrodes fabricated by our method via effective electrophysiological signal delivery and acquisition. With the satisfactory performance of the conformal Au electrodes printed in this work, we expect the APD method to continue to be explored and that it will find far-reaching applications throughout wearable electronics, soft robotics, biochemical sensing and electrochemistry.

4.6 Reference

[1] A. C. Fischer, F. Forsberg, M. Lapisa, S. J. Bleiker, G. Stemme, N. Roxhed, F. Niklaus, *Microsystems Nanoeng.* **2015**, 1, 1.

[2] D. Wang, Y. Zhang, X. Lu, Z. Ma, C. Xie, Z. Zheng, *Chem. Soc. Rev.* **2018**, 47, 4611.

[3] Y. Song, R. M. Panas, J. B. Hopkins, *Precis. Eng.* **2018**, 51, 729.

[4] P. Li, Y. Zhang, Z. Zheng, *Adv. Mater.* **2019**, 31, 1.

[5] A. M. Andrews, W. S. Liao, P. S. Weiss, *Acc. Chem. Res.* **2016**, 49, 1449.

[6] W. J. Sames, F. A. List, S. Pannala, R. R. Dehoff, S. S. Babu, *Int. Mater. Rev.* **2016**, 61, 315.

[7] D. J. Finn, M. Lotya, J. N. Coleman, *ACS Appl. Mater. Interfaces* **2015**, 7, 9254.

[8] Q. Huang, K. N. Al-Milaji, H. Zhao, *ACS Appl. Nano Mater.* **2018**, 1, 4528.

[9] J. Jiang, B. Bao, M. Li, J. Sun, C. Zhang, Y. Li, F. Li, X. Yao, Y. Song, *Adv. Mater.* **2016**, 28, 1420.

[10] M. Tavakoli, M. H. Malakooti, H. Paisana, Y. Ohm, D. Green Marques, P. Alhais Lopes, A. P. Piedade, A. T. de Almeida, C. Majidi, *Adv. Mater.* **2018**, 30, 1.

[11] H. Zhao, K. N. Al-Milaji, Q. Huang, Z. Li, T. N. Ng, *ACS Appl. Electron. Mater.* **2020**, 2, 3289.

[12] K. S. Bhat, U. T. Nakate, J. Y. Yoo, Y. Wang, T. Mahmoudi, Y. B. Hahn, *Chem. Eng. J.* **2019**, 373, 355.

[13] S. B. Walker, J. A. Lewis, *J. Am. Chem. Soc.* **2012**, 134, 1419.

[14] T. Tanaka, A. Ishikawa, S. Kawata, *Appl. Phys. Lett.* **2006**, 88, 1.

[15] A. Ishikawa, T. Tanaka, S. Kawata, *Appl. Phys. Lett.* **2006**, 89, 1.

[16] Y. Liu, Q. Hu, F. Zhang, C. Tuck, D. Irvine, R. Hague, Y. He, M. Simonelli, G. A. Rance, E. F. Smith, R. D. Wildman, *Polymers (Basel).* **2016**, 8, 325.

[17] E. Blasco, J. Müller, P. Müller, V. Trouillet, M. Schön, T. Scherer, C. Barner-Kowollik, M. Wegener, *Adv. Mater.* **2016**, 28, 3592.

[18] B. Bin Xu, Z. C. Ma, L. Wang, R. Zhang, L. G. Niu, Z. Yang, Y. L. Zhang, W. H. Zheng, B. Zhao, Y. Xu, Q. D. Chen, H. Xia, H. B. Sun, *Lab Chip* **2011**, 11, 3347.

[19] Z.-C. Ma, Y.-L. Zhang, B. Han, Q.-D. Chen, H.-B. Sun, *Small Methods* **2018**, 2, 1700413.

[20] Q. Ge, Z. Li, Z. Wang, K. Kowsari, W. Zhang, X. He, J. Zhou, N. X. Fang, *Int. J. Extrem. Manuf.* **2020**, 2, 022004.

[21] D. Wu, J. Song, Z. Zhai, M. Hua, C. Kim, I. Frenkel, H. Jiang, X. He, *ACS Appl.*

Mater. Interfaces **2019**, 11, 47468.

[22] M. Hua, D. Wu, S. Wu, Y. Ma, Y. Alsaid, X. He, *ACS Appl. Mater. Interfaces* **2021**, 13, 12689.

[23] M. Gregorini, R. N. Grass, W. J. Stark, *Ind. Eng. Chem. Res.* **2020**, 59, 12048.

[24] Y. Zhang, Z. Liang, A. P. Zhang, H. Tam, *Adv. Opt. Mater.* **2021**, 2001368, 1.

[25] X. Yang, M. Sun, Y. Bian, X. He, *Adv. Funct. Mater.* **2019**, 29, 1.

[26] X. Wang, K. Cui, Q. Xuan, C. Zhu, N. Zhao, J. Xu, *ACS Appl. Mater. Interfaces* **2019**, 11, 21668.

[27] X. Liu, X. Zhou, Y. Li, Z. Zheng, *Chem. - An Asian J.* **2012**, 7, 862.

[28] Z. Zhao, J. Bai, Y. Yao, C. Wang, *Mater. Today* **2020**, 37, 10.

[29] M. Hua, S. Wu, Y. Ma, Y. Zhao, Z. Chen, I. Frenkel, J. Strzalka, H. Zhou, X. Zhu, X. He, *Nature* **2021**, 590, 594.

[30] S. Wu, M. Hua, Y. Alsaid, Y. Du, Y. Ma, Y. Zhao, C. Y. Lo, C. Wang, D. Wu, B. Yao, J. Strzalka, H. Zhou, X. Zhu, X. He, *Adv. Mater.* **2021**, 33, 1.

[31] Z. He, W. J. Xie, Z. Liu, G. Liu, Z. Wang, Y. Q. Gao, J. Wang, *Sci. Adv.* **2016**, 2, e1600345.

[32] V. Merk, C. Rehbock, F. Becker, U. Hagemann, H. Nienhaus, S. Barcikowski, *Langmuir* **2014**, 30, 4213.

[33] R. Du, Y. Hu, R. Hübner, J. O. Joswig, X. Fan, K. Schneider, A. Eychmüller, *Sci. Adv.* **2019**, 5, 1.

[34] P. Bianchi, G. Petit, J. C. M. Monbaliu, *React. Chem. Eng.* **2020**, 5, 1224.

[35] C. Fan, T. Bian, L. Shang, R. Shi, L. Z. Wu, C. H. Tung, T. Zhang, *Nanoscale* **2016**,

8, 3923.

[36] J. He, Y. Wang, Y. Feng, X. Qi, Z. Zeng, Q. Liu, W. S. Teo, C. L. Gan, H. Zhang, H. Chen, *ACS Nano* **2013**, 7, 2733.

[37] Q. Cheng, L. Song, H. Lin, Y. Yang, Y. Huang, F. Su, T. Chen, *Langmuir* **2020**, 36, 250.

[38] W. Li, N. Matsuhisa, Z. Liu, M. Wang, Y. Luo, P. Cai, G. Chen, F. Zhang, C. Li, Z. Liu, Z. Lv, W. Zhang, X. Chen, *Nat. Electron.* **2021**, 4, 134.

[39] M. Gregorini, R. N. Grass, W. J. Stark, *Ind. Eng. Chem. Res.* **2020**, 59, 26, 12048–12055.

[40] C. Schoner, A. Tuchscherer, T. Blaudeck, S. F. Jahn, R. R. Baumann, H. Lang, *Thin Solid Films* **2013**, 531, 147

[41] W. Cui, W. Lu, Y. Zhang, G. Lin, T. Wei, L. Jiang, *Colloids Surfaces A Physicochem. Eng. Asp.* **2010**, 358, 35

[42] S. Mekhmouken, N. Battaglini, G. Mattana, A. Maurin, S. Zrig, B. Piro, D. Capitao, V. Noel, *Electrochem. commun.* **2021**, 123, 106918.

[43] A. Escudero, L. Gonzalez-Garcia, R. Strahl, D. J. Kang, J. Drzic, T. Kraus, *Inorg. Chem.* **2021**, 60, 17103.

[44] Y. Wu, Y. Li, B. S. Ong, P. Liu, S. Gardner, B. Chiang, *Adv. Mater.* **2005**, 17, 184.

[45] W.-E. Lu, Y.-L. Zhang, M.-L. Zheng, Y.-P. Jia, J. Liu, X.-Z. Dong, Z.-S. Zhao, C.-B. Li, Y. Xia, T.-C. Ye, X.-M. Duan, *Opt. Mater. Express* **2013**, 3, 1660.

Chapter 5. Liquid Metal Printing for wearable electronics and soft robotics

5.1 Introduction

Soft circuits have drawn tremendous interest in a broad range of emerging technologies, such as wearable electronics,[1,2] biomedical devices,[3] human-machine interface,[4] and soft robotics.[5] Besides high conductivity and reliable signal transmission, many new characteristics are demanded over traditional rigid electronics, such as light weight, flexibility, stretchability and conformability. Extensive research has been undertaken to develop new material systems and fabrication techniques, yet challenges remain in various aspects of soft electronic performance and manufacturing.[6]

In recent decades, stretchable circuits have been created by fabricating inextensible conductive materials into unique flexible structures, such as serpentine ribbons and out-of-plane arc-shaped structures, to gain deformability and stretchability.[7–9] Despite of the maturity and compatibility of the fabrication techniques with conventional rigid electronic components, structure-based stretchable circuits could only provide limited stretchability. Conductive composites with conductive fillers, such as carbon materials[10,11] and metallic micro/nanomaterials[12,13] in elastomer matrices, offer an alternative solution. Although the stretchability was improved, most composites sacrifice conductivity due to the limited conductive paths in the polymeric matrix and poor interface between conductive fillers. Therefore, conductors with intrinsic stretchability, including ionic conductors,[14,15] conducting polymers,[16] and room-temperature liquid metals (LMs),[17] have attracted great interest. Gallium-based LMs, especially eutectic gallium indium (EGaIn), provide much higher electrical

conductivity and larger stretchability due to their metallic and fluidic intrinsic at room temperature. Additionally, EGaIn has been studied extensively due to its unique properties, such as water-like viscosity, low toxicity, high thermal conductivity, neglectable volatility, and the formation of oxide skin,[17,18] and been widely utilized in wearable electronics,[19–23] epidermal sensing,[24–26] thermal devices,[27–31] and soft robotics.[32–35]

LM has been fabricated into various 2D/3D soft circuits with diverse fabrication techniques. Conventional manufacturing methods such as stencil printing, laser ablation and photolithography have been used.[36–39] Taking advantages of its fluid nature, LM can be injected or vacuum filled into soft microfluidics and porous template.[40,41] Selectively wetting of LM on rigid metal patterns was also reported.[42,43] In addition, additive manufacturing strategies have been utilized to print LM, including inkjet printing, direct writing and magnetic/voltage/freezing assisted printing.[18] Digital light processing (DLP) as one of the most popular additive manufacturing technology, which generates high-quality light pattern by modulating light via a micromirror array, has been used to fabricate 2D patterns/3D objects of polymer, ceramic and metal materials.[50–53] Despite of the excellent accuracy and resolution, as well as relatively high printing efficiency, DLP has not yet been reportedly used for LM printing.

Even though bulk LM has been used for fabricating soft circuits, its high surface tension largely hinders its applications, due to the issues of limited resolution, discontinuous fluid during jetting, and unreliable connection under strain. Therefore, increasing number of research suggests using liquid metal particles (LMPs) instead, which can be

easily obtained by applying shear or vibration to bulk LM. The oxide skin of LMP not only diminishes the tension, but also endows LMP with unique surface reactivity, which substantially extend its applications.[44] To fabricate soft circuits, LMPs were usually cast or molded into films and forms, then sintered with laser or localized pressure to form conductive paths, which lead to limited materials utilization rate and low resolution.[45,46] Recently, advanced strategies using LMP composites to fabricate stretchable circuits with excellent electromechanical properties have been proposed. Liu *et al.* invented a biphasic EGaIn via oxidation and phase segregation at high temperature.[47] Neumann *et al.* developed a self-encapsulating LMP-PDMS composite for direct write printing.[48] Lee *et al.* reported a ultrasonication strategy enabling the connection between LMPs in various polymer matrix. [49] Despite of satisfactory performance, the high-energy-input and multi-step fabrication process, the possible nozzle clogging issue due to the build-up oxidation and polymer solidification, or reliance of physical mask for patterning, persuade the searching for a novel and energy-saving fabrication solution with high efficiency and moderate processing conditions.

5.2 Proposed Method

Herein, we introduce a facile and scalable strategy to fabricate highly conductive (3.0×10^6 S m^{-1}) LM patterns with extreme stretchability (> 2500%) via DLP-based projection lithography for the first time. In this work, a DLP system was utilized via projecting UV patterns to achieve LM printing. Modified LMPs were crosslinked via photopolymerization for pattern formation, and mechanically sintered to obtain

electrical conductance. The whole fabrication process was conducted in the ambient condition at room temperature with a simple light exposure for a few seconds and a low energy input. We systematically investigated the critical parameters of the pattern formation, including ink formulation and light exposure. The electromechanical performance of the printed EGaIn including twisting, bending and stretching was carefully studied. To explore the potential of this printing method, we demonstrated a broad range of applications for on-body electronics, including an epidermal strain sensor for gesture monitoring, an electrically driven heater for thermal therapy, a humidity sensor for breath and finger contact, conformal electrodes for electrophysiology monitoring. In addition, we utilized the printed LM traces to fabricate thin-film soft actuators including a multi-layer electromagnetic actuator and electroactive liquid crystal elastomer actuators.

5.3 Experimental and Characterization Section

5.3.1 Materials

Gallium (Ga) purchased from Gallant Metals and Indium (In) purchased from Luciteria Science were combined in a ratio of 75% Ga and 25% In by weight to produce Eutectic Gallium Indium (EGaIn). 2-hydroxyethyl acrylate (2-HEA), diphenyl(2,4,6-trimethylbenzoyl)phosphine oxide (TPO), 3-(trimethoxysilyl) propyl methacrylate, allylamine, acrylamide, 1,6-hexanedithiol, acrylic acid, 11-phosphonoundecyl acrylate (11-PUA), poly(ethylene glycol) diacrylate (PEGDA), trimethylolpropane ethoxylate triacrylate (ETPTA, Mn 428 and 912), pentaerythritol tetraacrylate, trimethylolpropane

triacrylate, polyethylene glycol 200 (PEO-200), 2-hydroxy-4′-(2-hydroxyethoxy)-2-methylpropiophenone (Irgacure 2959), pentaerythritol tetrakis(3-mercaptopropionate) (PETMP), 2,2′-(ethylenedioxy)diethanethiol, dipropylamine (DPA), polystyrene-block-polyisoprene-block-polystyrene (SIS), dipolyethylene terephthalate (PET) thin films were purchased from Sigma-Aldrich, Inc. 2-Methyl-1,4-phenylene bis(4-(3-(acryloyloxy)propoxy)benzoate) (RM 257) was purchased from Shijiazhuang Sdyano Fine Chemical, Co., Ltd.. Toluene was purchased from Avantor Performance Materials. Glass slides and ethanol were purchased from Fisher Scientifics, Inc.

5.3.2 Material Fabrication

In all cases, 500 mg of EGaIn liquid metal was transfer via a syringe into a 20 ml vial. 20 mg surface modifying agent was dissolved in 10ml ethanol and then the solution was added into the vial. The vial was immersed approximately half of the solution level into a chilled water bath with ice before immersing a 15 mm tapered tip powered by Q500 Sonicator from Qsonica Inc. into the solution in the open vial. The ultrasonication procedure was set to an amplitude of 20%, 30%, 40% and a sonication time of 5, 10, 15, 20 minutes respectively. After the ultrasonication, the clear colorless solution turned into a dark grey colloidal solution which contains EGaIn particles. The suspension was placed still in dark overnight, allowing the modifying agents to fully react with the gallium oxide shell and. Then, the solution was centrifuged in 2000 rcf for 3 min and the supernatant was removed and replaced. This process was repeated for three times with a final suspension of EGaIn particles and 1 ml ethanol.

5.3.3 Precursors Formulate

Stock solutions with different components were prepared separately including 150-900 mg/mL LMPs solution, 200 mg/ml PEO-200 ethanol solution, 0.1-0.3 mmol/ml ETPTA-912 ethanol solution. The printable inks in this work were formulated by mixing the as-prepared solutions of LMPs, PEO-200 and ETPTA with 2-HEA in the volume ratios of 15:5:5:1. Then 0.4 vol% of TPO as photoinitiator was added and mixed under vortex to form the LMP inks for printing.

5.3.4 Printing Architecture and Procedure

The bottom-up setup consists of a DLP-based projector PRO4500 from Wintech Digital System Technology Corporation, a motorized translation stage mounted to a motor controller and optical accessories from Thorlabs, Inc.

The printing process was conducted under ambient conditions. Transparent substrates were placed on the translation stage and the focus of the projected patterns was adjusted to the top surface of the substrates. The LMP ink was vortexed before usage. Adequate amount of LMP ink was then casted on the substrates. Then a designed pattern was projected for 5-10 seconds and rinsed with ethanol and water to wash away the extra LMPs and solution. A designed LMPs-polymer pattern formed and a mechanical sintering such pressing and peeling was then proceeded to make the printed traces conductive.

5.3.5 Material Characterization

Scanning electron microscopy (SEM) images were taken by a ZEISS Supra 40VP SEM. The as-printed samples were observed under SEM after sputtering a thin gold layer using Pelco SC-7 sputter due to the existence of the oxide shell of LMPs. The sintered samples were directly observed without further treatment. The obtained SEM were analyzed using the software ImageJ. The particle sizes were determined by measuring the diameters of the particles. X-ray photoelectron spectra (XPS) were obtained using an X-ray photoelectron spectrometer (Axis Ultra, Kratos).

5.3.6 Electrical Characterization

A rectangular patten of LMPs with 3:1 aspect ratio was printed on a PET substrate and activated via mechanical sintering. The sheet resistance of the printed samples was measured with a four-point probe from Suzhou Jingge Electronic Co., Ltd. and 2450 digital multimers Keithley Instrument. The thickness of the activated LM patterns was measured with Phase-Shift Interference (PSI) mode by Bruker NT9300 optical profiler from Bruker corporation. The conductivity of activated LM patterns was calculated as the product of sheet resistance and thickness.

$$\rho = 4.53 \frac{VW}{I} D\left(\frac{d}{S}\right)$$

$$R_s = \frac{\rho}{W} \quad \kappa = \frac{1}{\rho}$$

ρ: electrical resistivity; V: voltage; I: current; W: thickness; d: short side length of the rectangular samples; S: probe spacing; $D\left(\frac{d}{S}\right)$: geometrical correction factor ($D\left(\frac{d}{S}\right) = 0.3286$ for the samples); R_s: sheet resistance; κ: electrical conductivity.

5.3.7 Electromechanical Characterization

A rectangular pattern of LMPs was printed and activated via mechanical sintering. The patterns printed on PET were for bending test and those printed on SIS were for stretching test. The printed samples on PET and SIS were subjected to bending and stretching respectively using a Unistretch mechanical tester from Cellscale Inc. The resistance of the printed LM patterns was measured using 2450 digital multimers from Keithley Instrument.

5.3.8 Demonstrations

All LM patterns in this work were printed by using the LMP ink via DLP projection lithography as described in the printing procedure section. For the stretchable “LA” LED array, 11 LEDs were adhered to the SIS substrate. With voltage held constant at 2.7V, the LED array was put under a strain of 70% by hand and then released repeatedly. For the strain sensor, a folded trace was printed on SIS and attached to the index finger of the tested volunteer. The resistance variation was measured and recorded with a 2450 digital multimers from Keithley Instrument. For the electrically driven heater, a curve trace was printed on SIS and different voltage were applied. The temperature and IR images were measured and recorded with a TiX580 thermal imager from Fluke Corporation. For the breath sensor, a cross finger electrodes pair was printed on PET and a PVA aqueous solution was casted on the cross-finger area. The device was then placed at ambient allowing water evaporation to form a PVA humidity sensitive film. By applying a 0.5V voltage, leakage current was measured and recorded using the 2450

digital multimers from Keithley Instrument. Same laminated structure can be utilized as a finger touch/proximity sensor. The capacitance change was measured and recorded using a DAQ6510 multimer system from Keithley Instrument. For the electrodes of EMG monitoring, a three-electrode pattern was printed on SIS. Then the other SIS thin film with punched holes was laminated above to seal the conductive trace. Ten 20 conductive paste was applied on the skin first and then the patch was conformably attached to the human subject's forearm epidermis. The signals were measured and recorded using a Cyton + Daisy biosensing board (16 channels) from OpenBCI Inc. For the bilayer electromagnetic actuator, a spiral and a rectangular pattern were printed on PET substrates separately. A VIA was created on the top layer by Genmitsu PROVerXL 4030 laser cutter from SainSmart. Then the two layers were laminated and a drop of bulk LM was injected to the VIA forming a conductive path through both layers. The LCE thin film was fabricated via a reported method, and then laminated with a LM circuit printed on PET. For both actuators, a silicone adhesive was used for interlayer binding and a E36313A programmable DC power supply from Keysight Instrument was used to control the power input.

5.4 Result and Discussion

5.4.1 Fabrication and Mechanism of LM Printing

To achieve the fast LM patterning via DLP projection lithography, we developed a unique LMP ink and a facile fabrication procedure (**Figure 5.1**). For formulation of the printable LMP ink, we first mixed appropriate amount of bulk EGaIn with modifying

agents in ethanol and shattered them via ultrasonic shearing to obtain modified LM micro- and nanoparticles. The LMP-ethanol dispersion was kept still in ambient condition for several hours before being centrifuged to obtain modified LMPs. Then the modified LMPs were rinsed and centrifuged with fresh ethanol solvent to remove the unreacted agents. Eventually, a concentrated modified LMP solution was obtained serving as a stock solution (**Figure 5.1**b). The prepared LMPs were modified with ligands, which were chemically bonded to the Ga_2O_3 shell of the LMPs with the anchoring groups at one end. Various functional groups can serve such a purpose, such as hydroxyl, thiol, amine, phosphonic acid, carboxylic acid, silane, and amine.[44,46,54–56] Meanwhile, the modifying agents would provide alkene groups at the other end for the subsequent photo-crosslinking process. In this work, we specifically used 2-hydroxyethyl acrylate (2-HEA) to modify LMPs for demonstrations. As the modified LMP stock solution was prepared, we adequately mixed it with additives including crosslinker, dispersant, monomer and photoinitiator at an appropriate ratio to form the printable LMP ink.

The procedure of printing highly conductive liquid metal patterns with the LMP ink consisted of four steps (**Figure 5.1**a). First, the ink was drop-casted on a transparent substrate. After seconds until the LMPs ink became still, a designed UV light pattern was projected from the bottom of the substrate at the interface between the ink and substrate, using a DLP projection system with 385 nm UV light source. Within 5-10 seconds of exposure, a non-conductive crosslinked liquid metal particles (cLMPs) pattern can be printed on the substrate. Then ethanol was used to wash away the extra

non-crosslinked components and a clear cLMP pattern can be observed. At last, we activated the cLMP pattern to be highly conductive with simple mechanical sintering such as pressing and peeling.

It is noticeable that rapid printing speed, high printing resolution and flexible pattern design of the printed LM can be achieved due to the implementation of DLP, which utilizes a digital micromirror device to manipulate projected light patterns (**Figure 5.1**c & d). Maskless parallel printing intrinsic and the rapid photo crosslinking reaction of this method guarantee high throughput manufacturing. This is demonstrated by the rapid printing of a 3×3 array of a circuit pattern with a UV exposure for 10 seconds (**Figure 5.1**e), which significantly reduced the fabrication time, compared to other additive techniques such as direct writing (> 1 minute). In addition, cLMPs can be printed on rigid, flexible and stretchable substrates. A stretchable "LM" circuit was printed on a polystyrene-block-polyisoprene-block-polystyrene (SIS) rubber substrate and connected with LEDs, which remained the stable connection while being repeatedly stretched to 70% strain (**Figure 5.1**f). The as-fabricated LM pattern on SIS achieved a high conductivity of 3.0×10^6 S m^{-1} and well retained the conductance at a maximum strain of 2500%, which stood out of the state-of-the-art stretchable conductors (**Figure 5.1**g & **Table 5.1**).

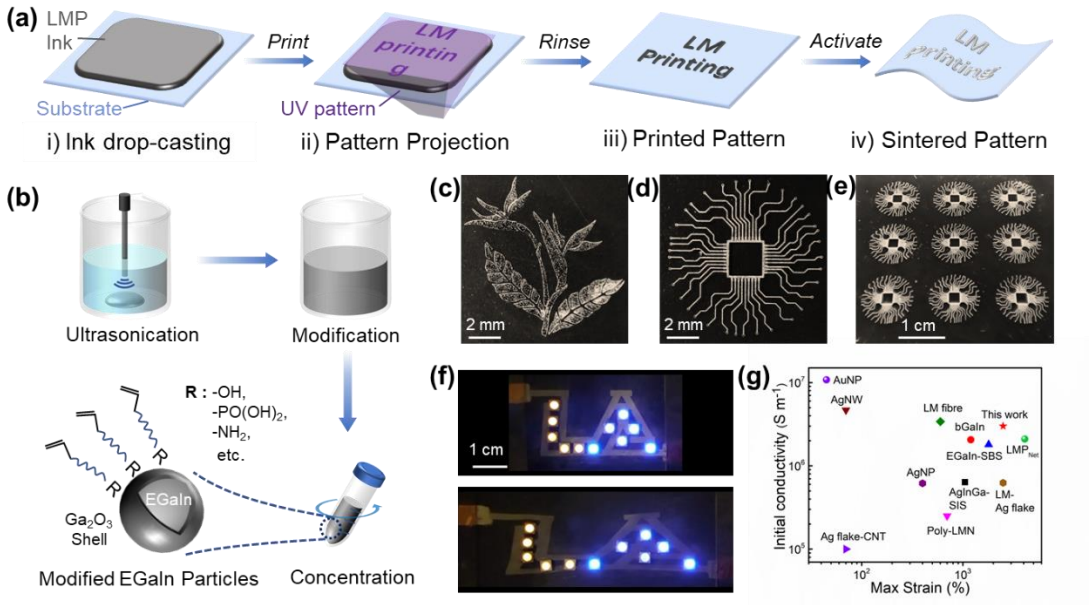

Figure. 5.1 Fabrication of conductive liquid metal patterns via DLP-based projection lithography. (a) Schematic of the printing process: (i) drop-casting of LMP ink; (ii) UV pattern projection on the substrate; (iii) obtaining the printed cLMP pattern after rinsing off non-reacted components; (iv) activation to form a conductive flexible LM pattern, via mechanical sintering such as pressing and peeling. (b) Schematic of modified LMP stock solution preparation: bulk LM was first broken into LMPs in ethanol under ultrasonication; the dispersion was kept still for the anchoring of modifying agent to anchor to the oxide shell of LMPs afterward; the modified LMPs solution was then rinsed and concentrated by centrifuging to obtain the modified LMP stock solution. (c-e) Images of printed LM patterns of a Strelitzia reginae (bird of paradise flower), a circuit, and a circuit array; (f) A stretchable LM circuit printed on a SIS substrate connected with LEDs; (g) Comparison of initial conductivity and stretchability with various stretchable conductors: silver flakes and multiwalled carbon nanotubes in styrene isoprene block copolymer rubber (Ag flake-CNT)[10], silver nanoparticles (AgNP)[12], silver nanowires (AgNW)[13], gold nanoparticles (AuNP)[57], silver microflakes

with EGaIn in styrene isoprene block copolymer rubber (AgInGa-SIS)[58], biphasic Ga-In (bGaIn)[47], EGaIn-coated poly(styrene-block-butadiene-block-styrene) microfiber mat (EGaIn-SBS)[59], polymerized liquid metal networks (Poly-LMN)[46], liquid metal fiber (LM fibre)[60], liquid metal and silver flakes in polyurethane acrylate elastomer (LM-Ag flake)[61], and long range assembled network of LMPs (LMP_{Net})[49].

Table 5.1. Comparison of various stretchable conductors

Materials	Patterning Process	Conductivity (10^6 S/m)	Maximum Strain (%)	Ref.
EGaIn	DLP printing	3.12	2500	This work
LMP Net	Screen printing, Photolithography	2.10	4100	49
bGaIn	Transfer printing	2.06	1200	47
AgInGa-SIS	Direct ink writing	0.638	1050	58
LM-Ag flakes	Direct ink writing	0.625	2500	61
EGaIn-SBS	Screen printing	1.80	1800	59
Poly-LMN	/	0.25	700	46
LM fibre	/	3.40	600	60
EGaIn-PVP	Screen printing	0.69	800	68
Ag flake-CNT	Direct ink writing	0.10	70	10
AgNP	Screen printing	0.617	400	12
AgNW	Screen printing	4.67	70	13
AuNP	DLP printing	1.08	45	57
PEDOT:PSS	Inkjet printing	0.31	800	69

To further understand and optimize this printing technique, we firstly investigated the pattern formation process. Since the LMPs in the ink would precipitate due to their high density, the LMP ink was homogenized with vortex prior to printing. As the ink turned into a dark grey dispersion without obvious lamination, we drop-cast adequate amount

of ink onto the substrate. We observed that the LMPs in the dropped solution would sink to the bottom within seconds. Although oxide skin formed as the shell of LMPs, the particles did not stick to the substrate like bulk EGaIn, which can be attributed to a slip layer of ink formed between the LMPs and the substrate (**Figure 5.2**a). The thin slip layer was suggested to prevent the adhesion of LMPs to the substrate,[62] which was validated with a titling test (**Figure 5.3**). When drops of LMP ink were placed on glass substrates, tilting the substrate caused the LMPs flew off the substrate. However, when the ethanol solvent fully evaporated, the LMPs would adhere to the substrate. The printing process continued once the casted ink laminated. A UV light pattern was projected from bottom onto the ink-substrate interface to crosslink the modified LMPs and polymerized the adhesive monomers 2-HEA. After exposure and subsequent rinsing, the cLMPs pattern was printed on the substrate. By using sodium hydroxide to reduce the Ga_2O_3 shell and etch away the cLMPs, a polymeric poly-2-hydroxyethyl acrylate (PHEA) layer formed beneath the cLMPs layer was observed (**Figure 5.4**). Therefore, we concluded that the presence of the slip layer also led to the formation of adhesive PHEA layer at the bottom of the printed structure holding the cLMPs onside (**Figure 5.2**b). To obtain the conductance, the cLMPs pattern was then subject to shearing stress for activation. The applied stress would cause the rupture of the thin oxide layer and allow the EGaIn liquid inside the LMPs to flow out (**Figure 5.2**c). Due to the remerging intrinsic of EGaIn, conductive paths would form throughout the desired pattern. In addition, PHEA layer consists of abundant hydroxyl group providing a native-oxide-driven surface reconciliation of EGaIn onsite under mechanical

deformation, which contributed to the high stretchability of the printed conductor.[63] As the printed traces were subject to strain, the soft segments of PHEA would also be stretched. New surfaces with -OH were created, guiding the EGaIn to deform with the substrate. Once the strain being released, the EGaIn with Ga_2O_3 shell would reconfigure its surface to adapt to the post-stretched PHEA layer. It is noticeable that such bilayer structure on rubbery substrate can provide better electromechanical performance than directly mixing LMPs with rubber resin.

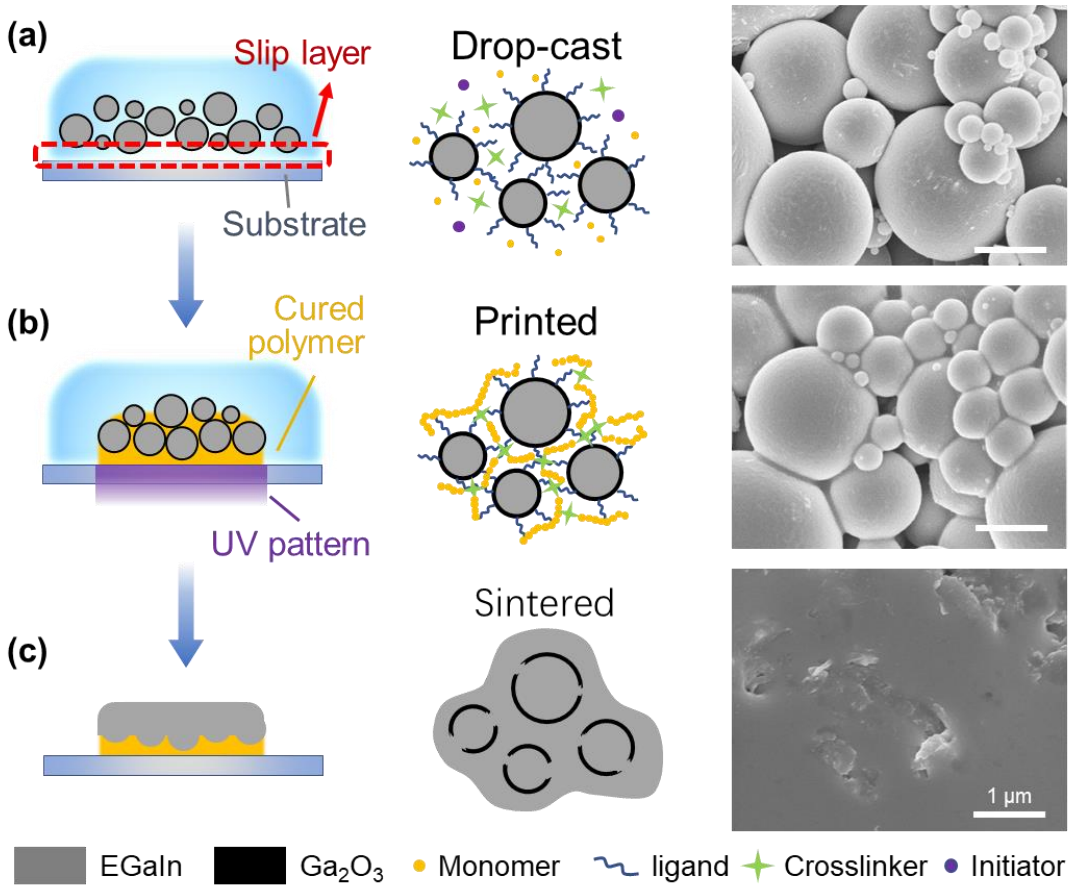

Figure 5.2 Mechanism of LM printing via DLP-based projection lithography. Schematics of (a) the drop-cast LM ink on a substrate, (b) the printed cLMP network, and (c) the activated LM-PHEA bilayer structure after activation and their corresponding SEM images.

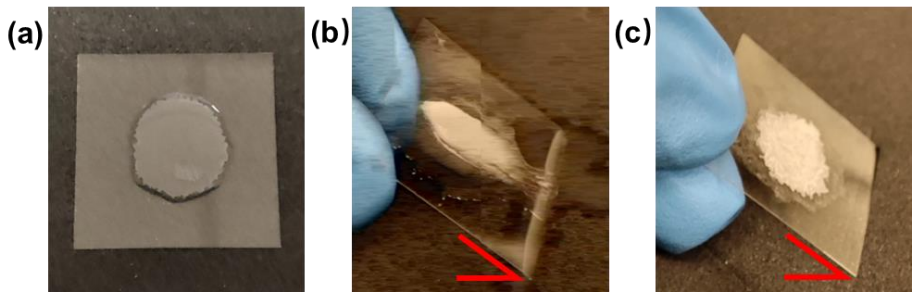

Figure 5.3. Optical images to validate the presence of layer under LMPs. (a) Liquid metal ink drop-casted on a glass slide; (b) Tilting the same glass slide with ink onside and (c) with dry LMPs onside.

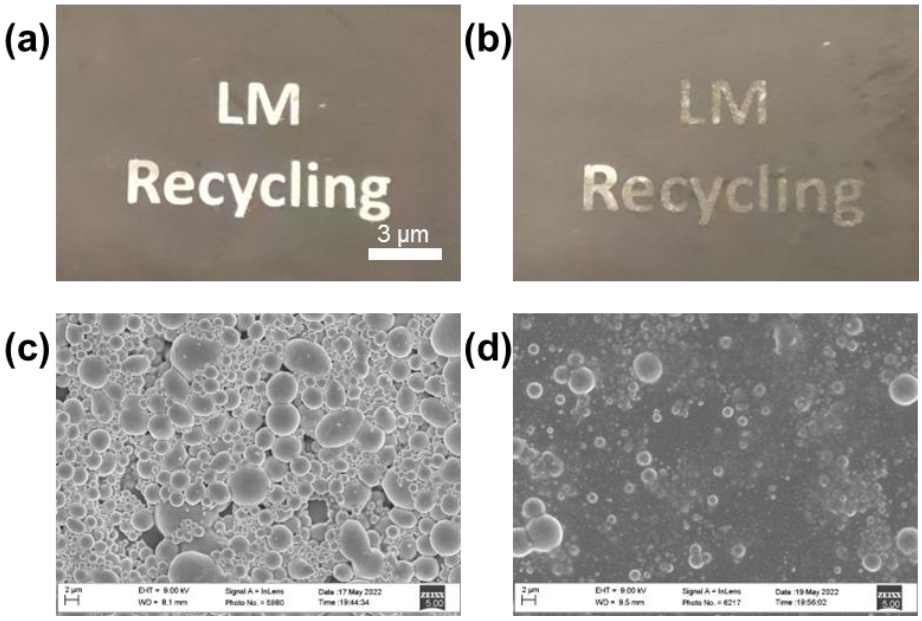

Figure 5.4. Recycling of printed LM pattern. (a) Optical image of the as-printed LM pattern.(b) Optical image of the same sample etched with 150 mmol/L NaOH solution. (c) Corresponding SEM image of as-printed LM pattern. (d) Corresponding SEM image of the remained PHEA pattern after etching.

5.4.2 Critical Parameters in Printing

To understand the critical parameters that determine the quality of the printed patterns, we investigated the particle size of LMPs, the input power density of light, the crosslinker concentration and LMPs concentration. Firstly, the average particles sizes **(Figure 5.5**a) and distribution of LMPs modified with 2-HEA (**Figure 5.6** & **Figure 5.7**) were measured. We observed that the particle sizes largely depended on the ultrasonication amplitude and time. With the increase in the amplitude from 20% to 40% and the ultrasonication time extending from 5 to 15 min, the average size of LMPs modified with 2-HEA decreased from 1.2 μm to ~320 nm. Similar trends were also observed with LMPs modified with 11-phosphonoundecyl acrylate (**Figure 5.8**). However, different modifying agents also have influence on the average particle sizes (**Figure 5.9** & **Figure 5.10**). During the optimizing of the printing process, we discovered that the particle size had significant effect on the patterning accuracy and the required input power density. Therefore, we designed a pattern of 8 strips with different width ranging from 22.5 μm to 1.44 mm and printed it with different LMP inks, which separately consisted of LMPs prepared with 20% amplitude and 5-, 10-, and 15-minutes sonication time. As we exposed the inks to a UV pattern of 2.58 $mW \cdot cm^{-2}$, only 7 strips were printed and the thinnest one was always absent for each print. By increasing the power input to 3.98 $mW \cdot cm^{-2}$, all 8 strips could be printed, which indicated that higher light intensity was required to achieve the printing with higher resolution. However, it is notable that increasing intensity can lead to the inaccurate printing of larger features. Blurred edges and filled gaps between strips were

observed on the samples printed with higher input power (**Figure 5.5**b). In addition, we observed that smaller particle sizes can improve the printing accuracy under the exposure of same light intensity. To obtain an overall picture of the relation between average particle sizes and the input power density, we designed patterns of strips and gaps with a width ranging from 22.5 μm to 5.4 mm using two LMPs inks (20% amplitude, 5 min and 15 min, noted as 20Amp-5min and 20Amp-15min). Then we printed the patterns with UV light of varied input power density, ranging from 0.14 $mW \cdot cm^{-2}$ to 8.03 $mW \cdot cm^{-2}$, and measured the achievable linewidth of strips (**Figure 5.5**c) as well as the resolution (**Figure 5.5**d). With an exposure intensity of 0.14 $mW \cdot cm^{-2}$, no pattern can be printed with the 20Amp-15min ink while the thinnest linewidth can be obtained with the 20Amp-5min ink was 270 μm. By increasing the light intensity, thinner lines became achievable for both inks. As the input power density increased to 3.83 $mW \cdot cm^{-2}$, the smallest linewidth (22.5 μm) this printing setup can provide was achieved. Further rise in input power will lead to the falling part of the printed larger patterns during rinsing, which can be attributed to the uneven photopolymerization and the failure of a continuous PHEA layer formation due to the overly high input power. Therefore, we expected that there would be an optimized range of input power for printing with different LMP inks. Moreover, resolution was another significant characteristic of printing, which was defined as the width of the smallest gap that can be printed. The increase of input power density would boost the feature size that can be resolved. The decrease in particle sizes could help achieve higher resolution with proper input power. The combination of linewidth and resolution studies would

give guidance on the design of pattern and the control of power input Herein we demonstrated an example by printing the same 8 strips pattern at different greyscale. (**Figure 5.5**e) With proper greyscale distribution, we printed the pattern with one exposure, which was clearer and more accurate compared to those printed with simple black and white images (**Figure 5.5**b).

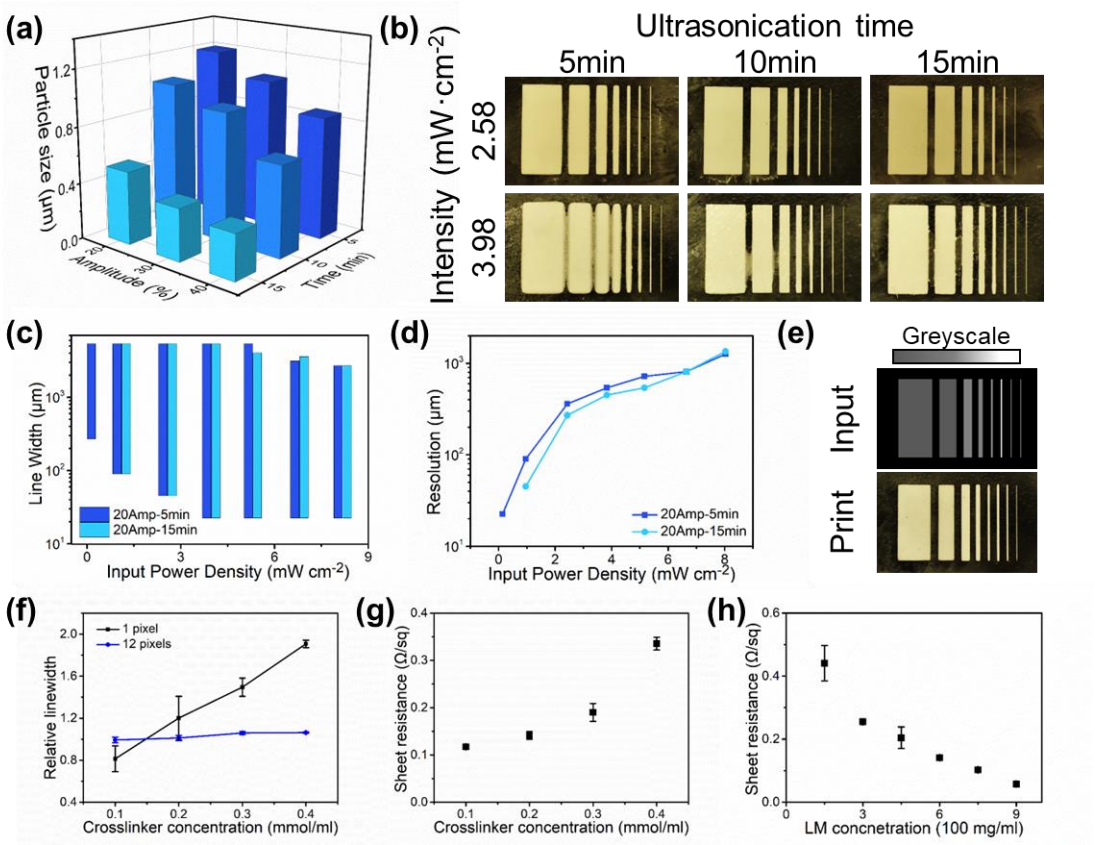

Figure 5.5 Investigation on critical parameters in fabrication process. (a) Average LMP sizes under different ultrasonication amplitude (20% to 40%) and time (5 to 15 min). (b) Images of the strip patterns printed with different light intensity using LMP inks prepared by different ultrasonication conditions. (c) Linewidth range of the printed strips with varied input power density. (d) Resolution of the printed traces with varied input power density. (e) A greyscale digital image (top) and corresponding printed LMPs pattern (bottom). (f) relative linewidths of printed strips using inks with varied

crosslinker concentrations. (g) sheet resistance of printed pattern as a function of crosslinker concentration in LMP inks. (h) sheet resistance of printed pattern as a function of LM concentration in LMP inks.

In addition to particle size and input power density, we also investigated the influence of crosslinker and LMP concentrations on the printing results. Various crosslinkers can serve for this material system while trimethylolpropane ethoxylate triacrylate was typically used in this study. 20AMP-5min LMP inks with same LMPs concentrations of 450 mg/ml and different crosslinker concentrations ranging from 0.1 to 0.4 mmol/ml were prepared to study the printed linewidth and sheet resistance. Relative linewidths of printed strips with 1- and 12-pixels width in digital image using different crosslinker concentrations were measured. For the 1-pixels strip which designed to be 22.5 μm, the actual printed linewidth increased along with the increasing crosslinker concentration, while the relative linewidth had negligible change for the 12-pixels strip (**Figure 5.5**f). However, both strips had a comparable variation at width around 20 μm with the increase of crosslinker concentration. Therefore, we suggested that the crosslinker concentration would have tremendous effect on the polymerization of LMPs at edges of the printed patterns. The higher the concentration was, the more LMPs would be crosslinked at pattern outlines. In addition, the increase of crosslinker concentration would also lead to the formation of a more resilient PHEA-LMP network, making it more difficult to break the oxide shell of the LMPs during the sintering. The tougher crosslinked network limited the formation of conductive paths, which eventually raised

the sheet resistance of the printed patterns (**Figure 5.5**g). To decrease the sheet resistance of the conductive traces, the most simple and effective way is to increase the LM concentration in the LMP ink. By raising the LM concentration from 150 to 900 mg/ml, a rapid decrease in the sheet resistance from 0.441 to 0.057 Ω/square can be observed (**Figure 5.5**h).

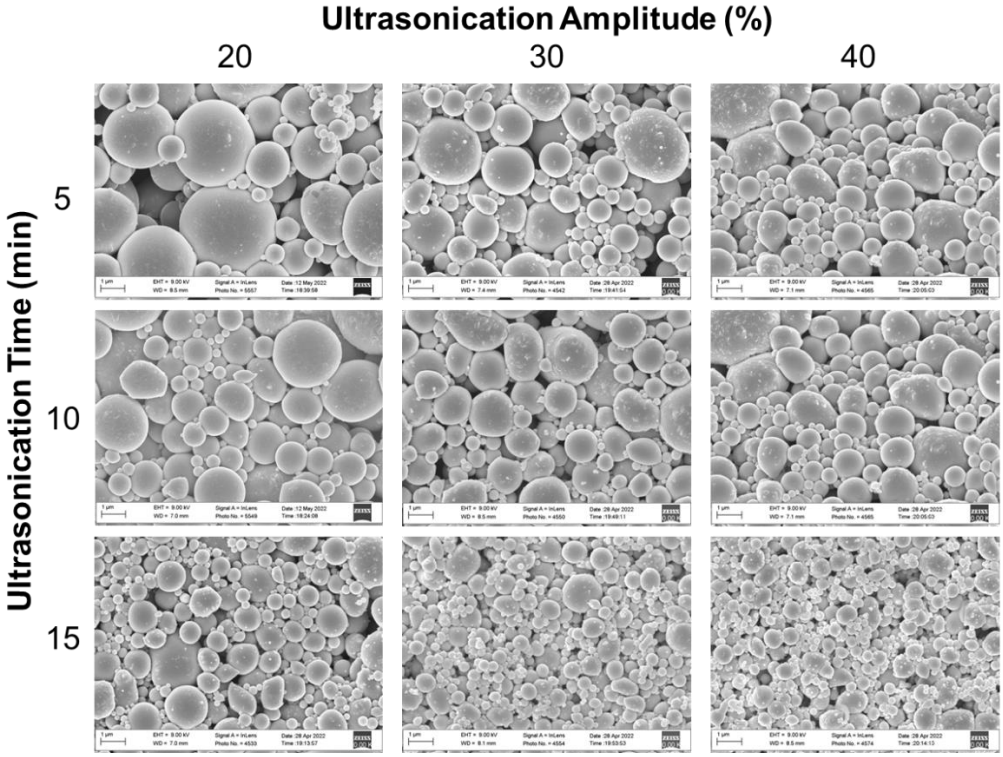

Figure 5.6 SEM images of LMPs modified with 2-hydroxyethyl acrylate (2-HEA) processed with different ultrasonication amplitude and time.

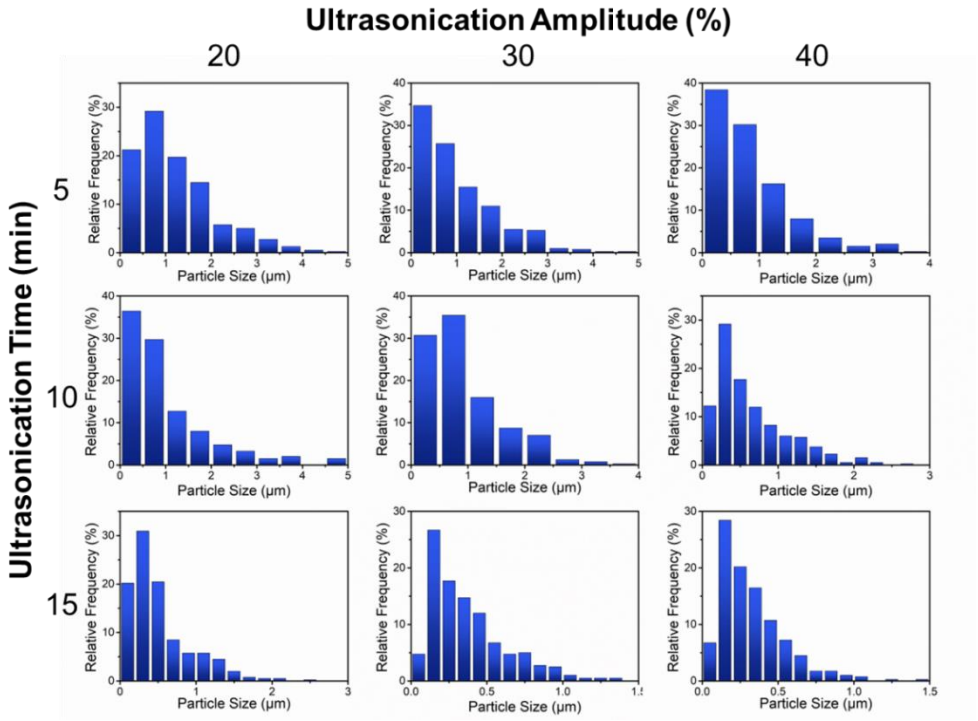

Figure 5.7 Particle size distribution of LMPs modified with 2-hydroxyethyl acrylate (2-HEA) processed with different ultrasonication amplitude and time.

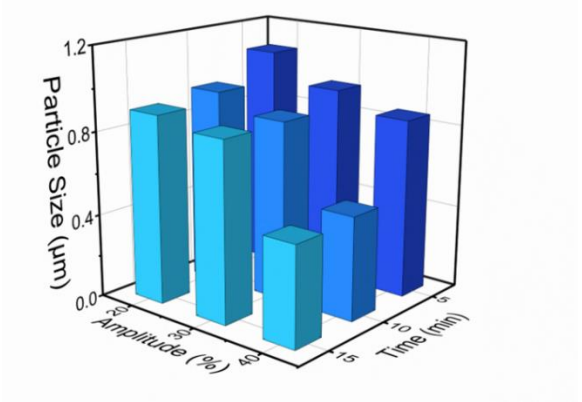

Figure 5.8 Average particle size of LMPs modified with 11-phosphonoundecyl acrylate under different ultrasonication amplitude and time.

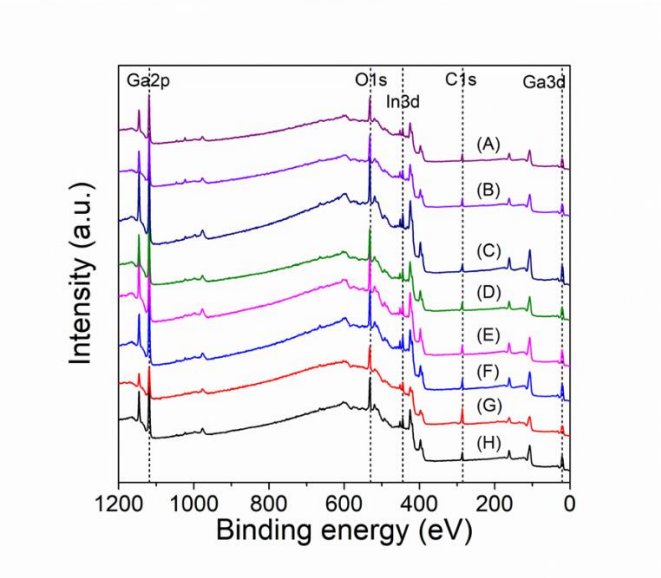

Figure 5.9 X-ray photoelectron spectra (XPS) of (a) unmodified LMPs and LMPs with different ligands including (b) 11-phosphonoundecyl acrylate; (c) 2-hydroxyethyl acrylate; (d) allylamine; (e) acrylamide; (f) acrylic acid; (g) 1,6-hexanedithiol; (h) 3-(trimethoxysilyl) propyl methacrylate.

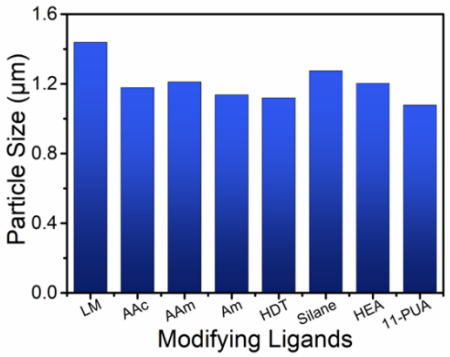

Figure 5.10 Average particle sizes of the LMPs modified with different ligands.

5.4.3 Electromechanical Performance

To evaluate the electromechanical performance of the LM patterns fabricated in this work, we printed and activated EGaIn traces on flexible substrate and stretchable

substrate and measured their relative resistance change (R/R_0) undergoing twisting, bending and uniaxial stretching. (**Figure 5.11**a) The traces printed on SIS had outstanding stable electromechanical performance with inconspicuous resistance change under various twisting angles up to 360°. (**Figure 5.11**b) For traces on flexible but non stretchable substrates like PET, electromechanical performance is commonly evaluated by bending test. By bending the traces printed on PET thin film inward and outward respectively with at a radius ranging from 2 to 24mm, negligible resistance change ($\Delta R/R_0 \approx \pm 0.01$) was observed (**Figure 5.11**c). Furthermore, we conducted 10,000 cycles of outward bending with a radius of 1 mm on the printed trace where limited resistance change ($\Delta R/R_0 < 0.03$, $\Delta R < 0.05\Omega$) was observed (**Figure 5.11**d).

To unveil the stretching limitation of the LM traces, we printed the pattern on highly stretchable SIS thin film and measured the change in resistance as a strain was put on the samples (**Figure 5.11**e). The printed trace showed satisfactorily low resistance change at low strain and notably high stretchability. The resistance changes measured at low strain ($R/R_0 \approx 1.22$ at 100% strain and $R/R_0 \approx 3.74$ at 500% strain) are much smaller than the theoretical prediction for an incompressible, constant-conductivity bulk liquid metal conductor using Pouillet's law ($R/R_0 = (1+\varepsilon)^2$, where ε is the applied strain; $R/R_0 = 4$ at strain of 100%, $R/R_0 = 36$ at strain of 500%). As the strain further increased from 500% to 2200%, the resistance increased linearly with the strain. Once the strain exceeded the critical point at 2200%, the resistance ascended rapidly until the substrate failed. We observed that at such high strain, the PHEA layer on the substrate was not fully covered by the LM layer due to the enlargement of the surface area during

stretching and the insufficient amount of LM to maintain the coverage. Despite of this, the tested sample can remain conductive at such high strain (>2500%). In addition, we studied cyclic stretching performance of the printed trace by subjecting it to a cyclic strain of 100% (**Figure 5.11**f). At the initial cycles, the resistance went through an adapting process with some increase and then settled to a stable electromechanical platform over 1500 cycles. We suggested to attribute the increase to mismatch at the interface between the solid copper tape electrodes and liquid EGaIn. In accordance with the study of the electrotechnical performance of the printed samples, the conductive traces possessed excellent stretchability and stability under strain. However, challenges in optimizing the interface between printed circuits and external connection, especially mounted electronics components, are expected to be addressed in the future.

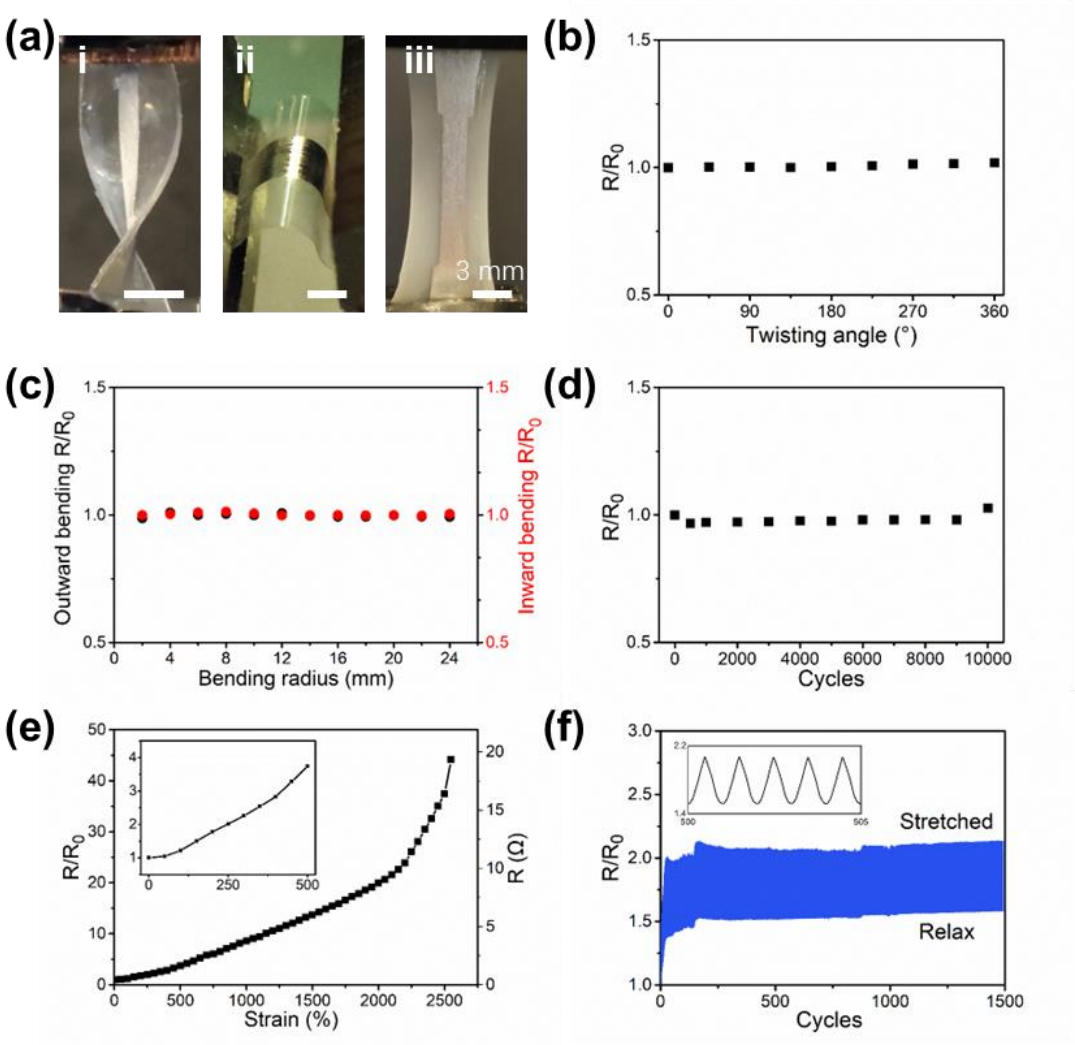

Figure 5.11 Electromechanical characteristics of printed LM patterns. (a) printed LM traces subjected to (i) twisting, (ii) bending and (iii) stretching. (b) Relative resistance changes as a function of twisting angle. c, Relative variation in resistance under outward (black) and inward (red) bending with a bending radius from 2 to 24 mm; (d) Relative resistance change of printed LM trace subjected to cyclic bending with a radius of 1 mm up to 10,000 cycles. (e) Relative resistance / resistance (Ω) variation as a function of strain. (f) Relative variation in resistance during cyclic stretching at a strain of 100% up to 1500 cycles.

5.4.4 Printed LM for Wearable Devices

To demonstrate the patterning capability of our printing method and the excellent electrical and electromechanical performance of the printed EGaIn, we fabricated several flexible/stretchable wearable devices including an electrically driven heater for thermal therapy, a humidity sensor for breath monitoring, conformal electrodes for electrophysiology monitoring, a strain sensor for soft haptics, and a capacitive sensor for detecting finger contact (**Figure 5.12**). Firstly, we printed a wave-shaped LM pattern serving as a resistive heater. The IR image (**Figure 5.12**a) showed the temperature distribution of the heater at ambient environment and after being powered with 5V for one minute. The average temperature of substrate can rise to around 80 °C within a minute. We also investigated the relation between the applied voltage and the temperature of the heater. By applying different voltages from 1V to 5V, we were able to control the heating temperature from 28°C to 83°C. Besides, we printed LM on SIS to fabricate an epidermal ohmic strain sensor to detect finger motions. The sensor was attached conformably to the index finger of the tested human subject. As the finger switched among relax state and bending states with angles of 45° and 90°, the resistance of the conductive pattern varied accordingly based on the bending angle (**Figure 5.12**e). The stable cycling performance and instant response to deformation allowed the strain senser to serve as an effective interface for tracking human body motions (**Figure 5.12**f). In addition of ohmic devices, we were able to fabricate a capacitive senser via integrating a printed interdigitated LM pattern and a casted thin polyvinyl alcohol (PVA) film onside (**Figure 5.12**c). PVA as a hygroscopic polymer can be utilized in fast and

stable humidity sensing due to its abundant hydroxyl groups64. With the excellent compatibility between the LM circuit and PVA coating, this thin-film sensor can be easily fabricated to detect humidity change and provide electrical output, which can serve as a breath sensor. By placing the sensor in front of the volunteer's nose in 2 cm and allowed the tested subject to conduct unevenly rapid breathing, normal breathing, and deep breathing. Each exhalation led to an increase in humidity of PVA sensing layer. By measuring the leakage current of the capacitive sensor under 0.5V voltage, different breathing modes can be obviously identified (**Figure 5.12**c). Such breath sensor has the potential to achieve complex breath monitoring by anchoring other electrochemical sensing materials to the printed circuit. Additionally, the same configuration can be utilized to detect the finger proximity/contact. We recorded the capacitance variation of the sensor under the tapping of a dry finger of the volunteer at varied frequencies (**Figure 5.12**g). The dry finger can retrain some moisture which can lead to the sudden change in capacitance. With different finger flapping frequencies from 1.25 Hz to 5.38 Hz, the sensor was capable to identify each contact between the finger and PVA layer.

Besides, we fabricated a conformal stretchable electrode patch for electromyography (EMG) signal monitoring (**Figure 5.12**d). A three-electrode LM pattern was printed on a SIS substrate and activated to achieve the conductivity. A SIS thin film with a hole pattern was laminated above to seal the conductive trace, leaving the contact electrodes exposed. The patch was then conformably attached to the human subject's forearm epidermis. The EMG signals were recorded by the LM patch clearly and continuously, comparable to those collected by the commercial Ag/AgCl electrodes. The safe and

reliable acquisition of EMG signals suggested broader potential applications with our LM printing technique in electrophysiological studies and diagnosis.

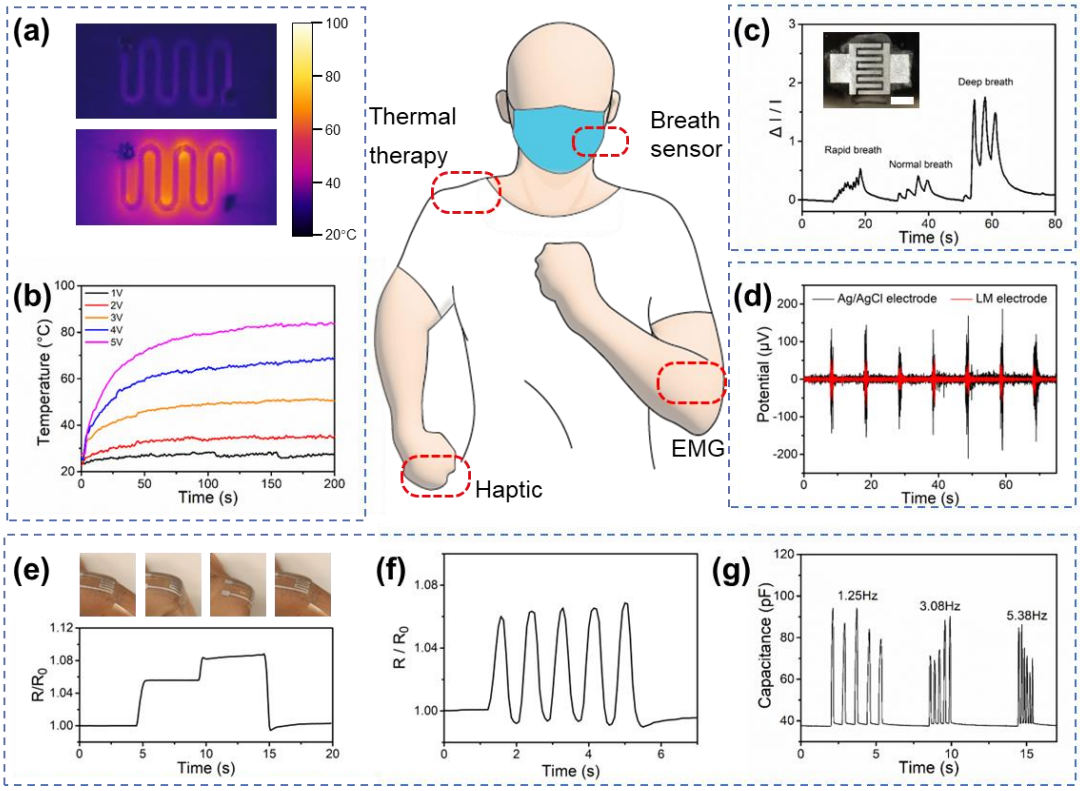

Figure 5.12 Applications of printed LM circuits for wearable electronics. (a) IR thermal images of the LM heater with wave structure for thermal therapy before and after applying a 5V voltage input. (b) Temperature evolution of the flexible LM heater with constant applied voltages from 1 to 5 V. (c) Leakage current curve of the proposed breath sensor for the sensing different breath patterns. (d) Electromyography (EMG) signals collected by LM electrodes (red) and commercial Ag/AgCl electrodes (black). (e) Resistance variation of the LM strain sensor on a finger bending with different angles. (f) Resistance variation of the LM strain sensor under multiple finger-bending cycles. (g) Capacitance curve of the proposed sensor for the finger contact at different frequencies of 1.25 Hz, 3.08 Hz and 5.38 Hz.

5.4.5 Printed LM for Soft Robotics

The outstanding electromechanical properties and the simple fabrication process of the printed LM drove us to exploit its applications in the field of soft robotics. Therefore, we fabricated two types of flexible thin-film actuators based on different mechanisms. A multilayer thin-film electromagnetic actuator was demonstrated at first (**Figure 5.13**a-c). A spiral and a rectangular conductive pattern were first printed on PET substrates separately (**Figure 5.13**a). A vertical interconnect access (VIA) was created on the top layer by laser cutting. Then the two layers were laminated and a small drop of LM was injected to the VIA for connecting LM traces on both layers. The bilayer actuator was then adhered at one side on a flat platform above a magnet. An input current was applied through the bilayer circuit to generate an instant magnetic field with an opposite direction to the permanent magnet. According to Ampere's Law ($\int B \cdot dI = \mu_0 I$, where B is the magnetic field, dI is an infinite element of the conductive pattern, μ_0 is the permeability of free space and I is the current flowing through the pattern), the generated magnetic field is proportional to the applied current. Therefore, we tuned the voltage from 1V to 10V to study the bending angle of the actuator (**Figure 5.13**b & **Figure 5.13**c). The actuation was instantly controlled, and a large bending angle around 120 degrees was achieved at a current of 100 mA.

In addition, we combined printed LM circuits with liquid crystal elastomer (LCE) to fabricate an electro-driven flexible thin-film actuator. LCE as a popular smart material with reversible shape transformation, suitable modulus, large actuation strain and good reliability.[65,66] It consists of mesogens which can transit from nematic state to isotropic

state with environmental stimuli, such as temperature, humidity and electric. Here we used a LCE composite which was synthesized and fabricated into thin films using a previously reported method.[67] The LCE thin film was then laminated with a PET thin film with LM traces onside to assemble the thin-film actuator (**Figure 5.13**d). By applying a current of 100 mA to the LM trace, we were able to achieve a reversible rolling-up motion of the actuator (**Figure 5.13**e). The deformation of the soft actuator can also be easily tuned by changing the input current. For illustration of its practical application, we further integrated and demonstrated a LM-LCE gripper (**Figure 5.14**). A current of 80 mA was applied to actuate the gripper, picking up soft objects including a soft sponge cube (**Figure 5.13**f) and a 3D printed hydrogel lattice. The release of the object was also achieved by simply turning off the power input, allowing the LCE to relax. These implementation results highlight the exceptional light weight and flexibility of the soft robotics based on flexible LM circuits printed with the technique presented in this study. Besides, the compatibility of handling soft materials and the ease of integration make our LM printing a promising solution for soft robotics and biomedical applications.

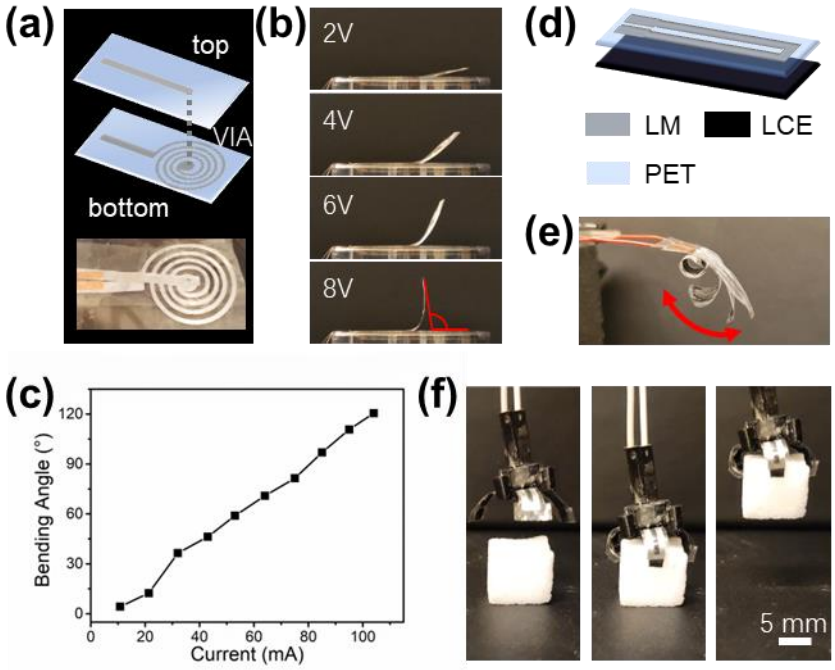

Figure 5.13 Applications of printed LM circuits for soft robotics. (a) Schematic and image of the bilayer thin film electromagnetic actuator. (b) Images of the actuator bending with varied input voltages. (c) Bending angle variation as a function of applied current. (d) Schematic of the bilayer LM-LCE actuator. (e) Images of the bilayer LM-LCE actuator rolling up with an input current of 100 mA. (f) LM-LCE gripper picking up a soft sponge cube via electrothermal actuation.

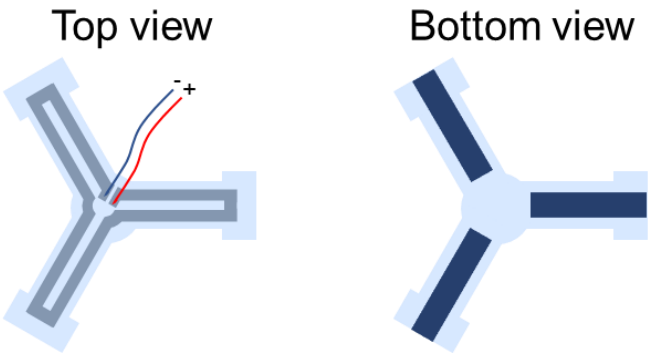

Figure 5.14 The structure of Liquid metal-Liquid crystal elastomer (LM-LCE) Gripper.

5.5 Conclusion

In this work, we introduced a facile and scalable fabrication method to pattern highly stretchable EGaIn with excellent electrical and electromechanical performance via DLP-based projection lithography at ambient conditions. The printed EGaIn incorporates high initial conductivity (3.0×10^6 S m^{-1}), extreme stretchability over 2500%, and great cyclic stability under different deformation types. The mechanism and process of fabrication has been carefully investigated for both understanding of this technique and guidance to optimize the materials system in the future. To exploit this printing technique, we fabricated and demonstrated a variety of wearable devices based on this approach, including epidermal sensors and electrodes, electrically driven heater and humidity sensors. Additionally, we showcased two types of thin-film soft actuators with light weight and outstanding flexibility, including an electromagnetic actuator which can achieve large bending angles, and LM-LCE actuators which can achieve rolling-up motion. We also demonstrated a LM-LCE gripper for picking up soft objects. With the scalable fabrication process and satisfactory performance of the printed LM, we expect the LM printing strategy presented in this work to enable low-cost mass production of flexible electronics for a wide range of applications in wearable electronics, medical devices and soft robotics.

5.6 Reference

[1] P. Won, S. Jeong, C. Majidi, S. H. Ko, *iScience* **2021**, *24*, 102698.

[2] M. D. Dickey, *Advanced Materials* **2017**, *29*, 1606425.

[3] B. Llerena Zambrano, A. F. Renz, T. Ruff, S. Lienemann, K. Tybrandt, J. Vörös, J. Lee, *Adv Healthc Mater* **2021**, *10*, 2001397.

[4] Z. Rao, F. Ershad, A. Almasri, L. Gonzalez, X. Wu, C. Yu, *Adv Mater Technol* **2020**, *5*, 2000233.

[5] S. I. Rich, R. J. Wood, C. Majidi, *Nat Electron* **2018**, *1*, 102.

[6] D. F. Fernandes, C. Majidi, M. Tavakoli, *J Mater Chem C Mater* **2019**, *7*, 14035.

[7] Z. Huang, Y. Hao, Y. Li, H. Hu, C. Wang, A. Nomoto, T. Pan, Y. Gu, Y. Chen, T. Zhang, W. Li, Y. Lei, N. H. Kim, C. Wang, L. Zhang, J. W. Ward, A. Maralani, X. Li, M. F. Durstock, A. Pisano, Y. Lin, S. Xu, *Nat Electron* **2018**, *1*, 473.

[8] J. A. Rogers, T. Someya, Y. Huang, *Science* **2010**, *327*, 1603.

[9] D.-H. Kim, N. Lu, R. Ma, Y.-S. Kim, R.-H. Kim, S. Wang, J. Wu, S. M. Won, H. Tao, A. Islam, K. J. Yu, T.-I. Kim, R. Chowdhury, M. Ying, L. Xu, M. Li, H.-J. Chung, H. Keum, M. Mccormick, P. Liu, Y.-W. Zhang, F. G. Omenetto, Y. Huang, T. Coleman, J. A. Rogers, *Science* **2011**, *333*, 833.

[10] H. S. Lee, Y. Jo, J. H. Joo, K. Woo, Z. Zhong, S. Jung, S. Y. Lee, Y. Choi, S. Jeong, *ACS Appl Mater Interfaces* **2019**, *11*, 12622.

[11] K. Fu, Y. Yao, J. Dai, L. Hu, *Advanced Materials* **2017**, *29*, 1603486.

[12] N. Matsuhisa, D. Inoue, P. Zalar, H. Jin, Y. Matsuba, A. Itoh, T. Yokota, D. Hashizume, T. Someya, *Nat Mater* **2017**, *16*, 834.

[13] J. Liang, K. Tong, Q. Pei, *Advanced Materials* **2016**, *28*, 5986.

[14] B. Yao, Y. Yan, Q. Cui, S. Duan, C. Wang, Y. Du, Y. Zhao, D. Wu, S. Wu, X. Zhu, T. Hsiai, X. He, *Matter* **2022**, *5*, 1.

[15] Y. Cao, T. G. Morrissey, E. Acome, S. I. Allec, B. M. Wong, C. Keplinger, C. Wang, *Advanced Materials* **2017**, *29*, 1605099.

[16] Y. Wang, C. Zhu, R. Pfattner, H. Yan, L. Jin, S. Chen, F. Molina-Lopez, F. Lissel, J. Liu, N. I. Rabiah, Z. Chen, J. W. Chung, C. Linder, M. F. Toney, B. Murmann, Z. Bao, *Sci Adv* **2017**, e1602076.

[17] S.-Y. Tang, C. Tabor, K. Kalantar-Zadeh, M. D. Dickey, *Annu Rev Mater Res* **2021**, *51*:1, 381-408.

[18] T. v. Neumann, M. D. Dickey, *Adv Mater Technol* **2020**, *5*, 1.

[19] Y. Jo, J. H. Hwang, S. S. Lee, S. Y. Lee, Y. S. Kim, D.-G. Kim, Y. Choi, S. Jeong, *ACS Appl Mater Interfaces* **2022**, *14*, 10747.

[20] Y. G. Park, G. Y. Lee, J. Jang, S. M. Yun, E. Kim, J. U. Park, *Adv Healthc Mater* **2021**, 2002280, 1.

[21] M. Zadan, C. Chiew, C. Majidi, M. H. Malakooti, *Multifunctional Materials* **2021**, *4*, 012001.

[22] L. Tang, J. Shang, X. Jiang, *Sci Adv* **2021**, *7*, eabe3778.

[23] L. Tang, L. Mou, J. Shang, J. Dou, W. Zhang, X. Jiang, *Mater Horiz* **2020**, *7*, 1186.

[24] L. Ding, C. Hang, S. Yang, J. Qi, R. Dong, Y. Zhang, H. Sun, X. Jiang, *Nano Lett* **2022**, *22*, 4482.

[25] Y. Li, S. Wang, J. Zhang, X. Ma, S. Cao, Y. Sun, S. Feng, T. Fang, D. Kong, *ACS Appl Mater Interfaces* **2021**, *14*, 13713.

[26] M. Liao, H. Liao, J. Ye, P. Wan, L. Zhang, *ACS Appl Mater Interfaces* **2019**, *11*, 47358.

[27] L. C. Jia, Y. F. Jin, J. W. Ren, L. H. Zhao, D. X. Yan, Z. M. Li, *J Mater Chem C Mater* **2021**, *9*, 2904.

[28] A. Uppal, M. Ralphs, W. Kong, M. Hart, K. Rykaczewski, R. Y. Wang, **2019**, *12*, 2625.

[29] N. Lazarus, B. Hanrahan, *Adv Mater Technol* **2016**, *1*, 1600130.

[30] Y. Wang, Z. Yu, G. Mao, Y. Liu, G. Liu, J. Shang, S. Qu, Q. Chen, R. W. Li, *Adv Mater Technol* **2019**, *4*, 1800435.

[31] S. Xiang, D. Liu, C. Jiang, W. Zhou, D. Ling, W. Zheng, X. Sun, X. Li, Y. Mao, C. Shan, *Adv Funct Mater* **2021**, *31*, 2100940.

[32] J. Zhang, R. H. Soon, Z. Wei, W. Hu, M. Sitti, *Advanced Science* **2022**, *9*, 2203730.

[33] J. Ye, Y.-C. Yao, J.-Y. Gao, S. Chen, P. Zhang, L. Sheng, J. Liu, *Soft Robot* **2022**, 9:6, 1098-1107.

[34] M. Zadan, D. K. Patel, A. P. Sabelhaus, J. Liao, A. Wertz, L. Yao, C. Majidi, *Advanced Materials* **2022**, *34*, 2200857.

[35] G. Mao, D. Schiller, D. Danninger, B. Hailegnaw, F. Hartmann, T. Stockinger, M. Drack, N. Arnold, M. Kaltenbrunner, *Nat Commun* **2022**, *13*, 4456.

[36] X. P. Hao, C. Y. Li, C. W. Zhang, M. Du, Z. Ying, Q. Zheng, Z. L. Wu, *Adv Funct Mater* **2021**, *31*, 1.

[37] C. W. Park, Y. G. Moon, H. Seong, S. W. Jung, J. Y. Oh, B. S. Na, N. M. Park, S. S. Lee, S. G. Im, J. B. Koo, *ACS Appl Mater Interfaces* **2016**, *8*, 15459.

[38] T. Lu, L. Finkenauer, J. Wissman, C. Majidi, *Adv Funct Mater* **2014**, *24*, 3351.

[39] Y. G. Park, H. Kim, S. Y. Park, J. Y. Kim, J. U. Park, *ACS Appl Mater Interfaces*

2019, *11*, 41497.

[40] Y. Lin, O. Gordon, M. R. Khan, N. Vasquez, J. Genzer, M. D. Dickey, *Lab Chip* **2017**, *17*, 3043.

[41] S. Liang, Y. Li, Y. Chen, J. Yang, T. Zhu, D. Zhu, C. He, Y. Liu, S. Handschuh-Wang, X. Zhou, *J Mater Chem C Mater* **2017**, *5*, 1586.

[42] C. Xiao, J. Feng, H. Xu, R. Xu, T. Zhou, *ACS Appl Mater Interfaces* **2022**, *14*, 20000.

[43] M. Tavakoli, M. H. Malakooti, H. Paisana, Y. Ohm, D. Green Marques, P. Alhais Lopes, A. P. Piedade, A. T. de Almeida, C. Majidi, *Advanced Materials* **2018**, *30*, 1.

[44] B. E. Kelly, I. Bhattacharya, H. Heidari, M. Shusteff, C. M. Spadaccini, H. K. Taylor, *Science* **2019**, *363*, 1075.

[45] X. Wen, B. Zhang, W. Wang, F. Ye, S. Yue, H. Guo, G. Gao, Y. Zhao, Q. Fang, C. Nguyen, X. Zhang, J. Bao, J. T. Robinson, P. M. Ajayan, J. Lou, *Nat Mater* **2021**, *20*, 1506.

[46] S. K. Saha, D. Wang, V. H. Nguyen, Y. Chang, J. S. Oakdale, S. C. Chen, *Science* **2019**, *366*, 105.

[47] J. R. Tumbleston, D. Shirvanyants, N. Ermoshkin, R. Janusziewicz, A. R. Johnson, D. Kelly, K. Chen, R. Pinschmidt, J. P. Rolland, A. Ermoshkin, E. T. Samulski, J. M. DeSimone, *Science* **2015**, *347*, 1349.

[48] S.-Y. Tang, R. Qiao, *Acc Mater Res* **2021**, *2*, 966.

[49] E. J. Markvicka, M. D. Bartlett, X. Huang, C. Majidi, *Nat Mater* **2018**, *17*, 618.

[50] C. J. Thrasher, Z. J. Farrell, N. J. Morris, C. L. Willey, C. E. Tabor, *Advanced Materials* **2019**, *31*, 1.

[51] S. Liu, D. S. Shah, R. Kramer-Bottiglio, *Nat Mater* **2021**, *20*, 851.

[52] T. v. Neumann, E. G. Facchine, B. Leonardo, S. Khan, M. D. Dickey, *Soft Matter* **2020**, *16*, 6608.

[53] W. Lee, H. Kim, I. Kang, H. Park, J. Jung, H. Lee, H. Park, J. Su Park, J. Min Yuk, S. Ryu, J.-W. Jeong, J. Kang, *Science* **2022**, *378*, 637.

[54] H. Li, R. Qiao, T. P. Davis, S.-Y. Tang, *Biosensors (Basel)* **2020**, *10*, 196.

[55] Z. J. Farrell, C. J. Thrasher, A. E. Flynn, C. E. Tabor, *ACS Appl Nano Mater* **2020**, *3*, 6297.

[56] X. Li, M. Li, J. Xu, J. You, Z. Yang, C. Li, *Nat Commun* **2019**, *10*, 3514.

[57] D. Wu, B. Yao, S. Wu, H. Hingorani, Q. Cui, M. Hua, I. Frenkel, Y. Du, T. K. Hsiai, X. He, *Advanced Materials* **2022**, *34*, 2201772.

[58] W. Zu, Y. Ohm, M. R. Carneiro, M. Vinciguerra, M. Tavakoli, C. Majidi, *Adv Mater Technol* **2022**, 2200534.

[59] Z. Ma, Q. Huang, Q. Xu, Q. Zhuang, X. Zhao, Y. Yang, H. Qiu, Z. Yang, C. Wang, Y. Chai, Z. Zheng, *Nat Mater* **2021**, *20*, 859.

[60] S. Zhu, J. H. So, R. Mays, S. Desai, W. R. Barnes, B. Pourdeyhimi, M. D. Dickey, *Adv Funct Mater* **2013**, *23*, 2308.

[61] K. Parida, G. Thangavel, G. Cai, X. Zhou, S. Park, J. Xiong, P. S. Lee, *Nat Commun* **2019**, *10*, 2158.

[62] M. R. Khan, C. Trlica, J. H. So, M. Valeri, M. D. Dickey, *ACS Appl Mater*

Interfaces **2014**, *6*, 22467.

[63] J. E. Park, H. S. Kang, M. Koo, C. Park, *Advanced Materials* **2020**, *2002178*, 1.

[64] S. A. Rahman, S. A. Khan, M. M. Rehman, W. Y. Kim, *Nanomaterials* **2022**, *12*(6), 1026.

[65] D. Sun, J. Zhang, H. Li, Z. Shi, Q. Meng, S. Liu, J. Chen, X. Liu, *Polymers (Basel)* **2021**, *13*(11), 1889.

[66] Y. Yan, Y. Zhao, Y. Alsaid, B. Yao, Y. Zhang, S. Wu, X. He, *Advanced Intelligent Systems* **2021**, *3*, 2000234.

[67] P. Shi, Y. Zhao, Z. Liu, X. He, *J Compos Mater* **2022**, DOI 10.1177/00219983221146618.

[68] L. Tang, L. Mou, J, Shang, J. Dou, W. Zhang, X. Jiang. *Mater Horiz* **2020**, 7, 1186–1194.

[69] Wang, Y., Zhu, C., Pfattner, R., Yan, H., Jin, L., Chen, S., Molina-Lopez, F., Lissel, F., Liu, J., Rabiah, N. I., Chen, Z., Chung, J. W., Linder, C., Toney, M. F., Murmann, B., & Bao, Z. *Science Advances*, 3, e1602076.

Chapter 6. Conclusion and outlook

6.1 Conclusion

DLP printing techniques are revolutionizing prototyping and production across diverse fields, including automotive, consumer goods, healthcare and industrial, due to their exceptional design flexibility, high printing resolution and precision, excellent scalability, mild fabricating conditions and rapid fabrication process. Despite of the numerous achievements of DLP printing, the technology is expected to deliver more benefits in various application scenarios. Therefore, we aimed to leverage DLP printing to fabricate diverse functional materials and exploit their potential applications in biomimetic study, soft robotics, and flexible electronics.

In Chapter 2, we developed a 4D printing strategy of hydrogel to mimic the morphogenesis of pumpkin through instability. Core-shell heterogeneous hydrogel structures were printed to replicate the distinct circumferential buckling formation process of pumpkins. The investigation of governing parameters allowed us to develop a mechanical model to understand the mechanism of the buckling formation. The 4D printing platform of fabricating heterogeneous structures was also demonstrated for mimicking the morphologic transformation of various plants.

In Chapter 3, we successfully adapted a hydrogel toughening mechanism to 3D printing platform, enabling the 4D printing of a thermoresponsive tough hydrogel. A freezing assisted salting-out method was applied as a post-treatment to endow a printable thermoresponsive PVA-based hydrogel with high toughness and large contraction force. Thermal and photothermal printed actuators with improved performance were achieved,

showcasing the potential of this material design for soft robotics applications.

In Chapter 4, we explored the application of DLP printing for direct patterning of conductive metal. An one-step room-temperature annealing-free gold printing method was developed. Specific ion effect was involved in the printing process, enabling the in-situ sintering of the deposited gold nanoparticles. This printing approach offered substantial tunability in structures, electrical properties and electrochemical performance of the printed gold. With high conductivity and excellent conformability, gold electrodes printed by this method was demonstrated to serve as reliable bioelectrodes for electrophysiological signal delivery and acquisition.

In Chapter 5, we developed a fast and facile liquid metal printing method based on DLP projection lithography. A liquid metal particles dispersion ink was formulated to realize photopatterning of liquid metal traces on various substrates. With the bilayer structural design, the printed liquid metal traces showed high electrical conductivity, extreme stretchability and outstanding electromechanical performance. Diverse wearable electronics and soft robotics based on printed liquid metal were demonstrated.

6.2 Outlook

The presented methods in this dissertation provide some insights on the development of DLP-based printing technologies. However, to launch printed devices for real-world applications, improvements in fabrication and performance are expected.

For 4D printing, there are some major challenges in the fabrication of complex objects and actuation performance. To achieve complicated shape transformation, highly

heterogeneous structures must be printed, which can be accomplished by using multiple materials or printing with anisotropic materials. However, both the development of multi-material printer and the control of a deposited anisotropic materials are still in their infant stage. The slow and inaccurate actuation also significantly limit the usefulness of 4D printing in the practical applications. Materials innovation is demanded to achieve faster response of 4D printed structures. Despite of these challenges, 4D printing holds tremendous potentials in various applications, including smart sensors, artificial tissues, automotives and even fashion, which are expected to be explored in the future.

While direct metal patterning via DLP is an inspiring achievement, it is just a first step towards its practical applications. Several obstacles can be foreseen including limited selection of materials and unoptimized properties. Expanding the range of printable metals and substrates will significantly broaden the scope of direct metal printing. Optimizing the microstructures, thickness and electrical properties will enhance the functional capabilities. Furthermore, engineering challenges in speeding up the fabrication process, controlling thin film thickness and improving interfaces with electronic components must be addressed to ensure reliable manufacturing.

In summary, the methods presented in this dissertation show great potential value of DLP-based printing for a wide range of applications. Many challenges remain in further improvement of these techniques and more possibilities are still unexploited. Therefore, we believe that DLP-based printing will continue to bring impacts to research and manufacturing.